DEVELOPMENT OF MICROWAVE AND MILLIMETER-WAVE INTEGRATED-CIRCUIT STEPPED-FREQUENCY RADAR SENSORS FOR SURFACE AND SUBSURFACE PROFILING

A Dissertation

by

JOONGSUK PARK

Submitted to the Office of Graduate Studies of
Texas A&M University
in partial fulfillment of the requirements for the degree of

DOCTOR OF PHILOSOPHY

December 2003

Major Subject: Electrical Engineering

DEVELOPMENT OF MICROWAVE AND MILLIMETER-WAVE INTEGRATED-

CIRCUIT STEPPED-FREQUENCY RADAR SENSORS

FOR SURFACE AND SUBSURFACE PROFILING

A Dissertation

by

JOONGSUK PARK

Submitted to Texas A&M University
in partial fulfillment of the requirements
for the degree of

DOCTOR OF PHILOSOPHY

Approved as to style and content by:

Cam Nguyen	Norris Stubbs
(Chair of Committee)	(Member)
Andrew K. Chan	Chanan Singh
(Member)	(Head of Department)
Ugur Cilingiroglu	
(Member)	

December 2003

Major Subject: Electrical Engineering

ABSTRACT

Development of Microwave and Millimeter-Wave Integrated-Circuit Stepped-

Frequency Radar Sensors for Surface and Subsurface Profiling. (December 2003)

Joongsuk Park, B.S., Yonsei University, Korea

Chair of Advisory Committee: Dr. Cam Nguyen

Two new stepped-frequency continuous wave (SFCW) radar sensor prototypes, based on a coherent super-heterodyne scheme, have been developed using Microwave Integrated Circuits (MICs) and Monolithic Millimeter-Wave Integrated Circuits (MMICs) for various surface and subsurface applications, such as profiling the surface and subsurface of pavements, detecting and localizing small buried Anti-Personnel (AP) mines and measuring the liquid level in a tank. These sensors meet the critical requirements for subsurface and surface measurements including small size, light weight, good accuracy, fine resolution and deep penetration. In addition, two novel wideband microstrip quasi-TEM horn antennae that are capable of integration with a seamless connection have also been designed. Finally, a simple signal processing algorithm, aimed to acquire the in-phase (I) and quadrature (Q) components and to compensate for the I/Q errors, was developed using LabView.

The first of the two prototype sensors, named as the microwave SFCW radar sensor operating from 0.6-5.6-GHz, is primarily utilized for assessing the subsurface of pavements. The measured thicknesses of the asphalt and base layers of a pavement sample were very much in agreement with the actual data with less than ±0.1-inch error. The measured results

on the actual roads showed that the sensor accurately detects the 5-inch asphalt layer of the pavement with a minimal error of ±0.25 inches. This sensor represents the first SFCW radar sensor operating from 0.6-5.6-GHz.

The other sensor, named as the millimeter-wave SFCW radar sensor, operates in the 29.72-35.7-GHz range. Measurements were performed to verify its feasibility as a surface and sub-surface sensor. The measurement results showed that the sensor has a lateral resolution of 1 inch and a good accuracy in the vertical direction with less than ± 0.04-inch error. The sensor successfully detected and located AP mines of small sizes buried under the surface of sand with less than 0.75 and 0.08 inches of error in the lateral and vertical directions, respectively. In addition, it also verified that the vertical resolution is not greater than 0.75 inches. This sensor is claimed as the first Ka-band millimeter-wave SFCW radar sensor ever developed for surface and subsurface sensing applications.

ACKNOWLEDGMENTS

I would like to express my sincere gratitude to my advisor, Dr. Cam Nguyen, for his guidance, dedication and support throughout this work. I would also like to thank my committee members, Dr. Andrew Chan, Dr. Norris Stubbs, and Dr. Ugur Cilingiroglu, for their valuable time and advice.

I wish to thank Mr. Tom Scullion, Mr. Lee Gustavus, and Mr. Tony Barbosa of the Texas Transportation Institute for their help, as well as Mr. John Guido and Mr. Thomas Gersbeck of the Texas Engineering Extension Service for providing mines. Finally, I would like to express my love and gratitude to my wife, Joowon Kim, son, Eugene Park, and my parents for their endless support and encouragement.

This work was supported in part by the National Science Foundation and in part by the National Academy of Sciences.

DEDICATION

To my wife, son, and parents

TABLE OF CONTENTS

CHAPTER

LIST OF FIGURES

LIST OF TABLES

CHAPTER I

INTRODUCTION

1.1 Fundamentals of Radar Sensors

Radar sensors have been used as an accurate and cost effective technique for nondestructive characterization of surface and subsurface in various applications, such as detecting and localizing buried mines or archeological sites, measuring distances, displacements, thicknesses or moisture contents, and profiling the surface or subsurface of pavement [1]-[8]. This section gives an overview of the fundamentals of these radar sensors.

An electromagnetic wave incident on a medium is scattered in all directions when it encounters a change in electric or magnetic properties of the medium. A careful analysis of the scattered electromagnetic waves leads to a better understanding of the characteristics of the medium, and also helps in appreciating the dynamics of a radar sensor in a holistic way, as will be covered in more detail in Chapter II.

A radar transmits electromagnetic waves towards a target (or object), and then receives the scattered electromagnetic waves back from it. The two-way travel time (t) of the electromagnetic wave is associated with the range (R) of the target, as defined by

$$t = \frac{2R}{c} \qquad\qquad 1.1$$

where c is the speed of light in free space.

Journal Model is *IEEE Transaction on Microwave Theory and Techniques*.

The important parameters of radar sensors are "penetration depth" and "resolution". The maximum penetration depth (R_{max}), which is achieved when the receiving power P_r is equal to the receiver sensitivity S_i, depends on the propagating medium's property, the antenna gain, the transmitting power P_t, the receiver bandwidth B and so on, as expressed by [9]

$$R_{\max} \propto \left[\frac{P_t G_t G_r \exp(-4aR_{\max})}{S_i} \right]^{\frac{1}{4}} \qquad 1.2$$

where $S_i = kTBF(SNR)$, and G_t and G_r are the transmitting and receiving antenna gains, respectively, and a is the attenuation constant of the medium. Modified radar equations for subsurface radar sensors are derived in Chapter II.

It is useful to consider the average transmitting power P_{tav}, which is the product of the transmitting power P_t and the inverse of the bandwidth B, hence Eq. 1.2 is modified as

$$R_{\max} \propto \left[\frac{P_{tav} G_t G_r \exp(-4aR_{\max})}{kTF(SNR)} \right]^{\frac{1}{4}} \qquad 1.3$$

The average transmitting power is one of controllable factors extensively used in designing a sensor and relates to the type of the waveform used. From the above facts, it can easily be deduced that more average transmitting power (Eq. 1.3) or more peak transmitting power combined with less bandwidth (Eq. 1.2) results in deeper maximum penetration.

The absolute bandwidth (B) of the transmitted EM waves determines the range (or vertical) resolution ΔR, which is the ability to distinguish closely spaced targets within a specific range R. It is given by

$$\Delta R = \frac{c}{2B} \qquad\qquad 1.4$$

The range resolution is inversely proportional to the bandwidth that can be associated with the shape of the waveform, as discussed in Section 1.2. Thus, one of the important design constraints of a radar sensor is the choice of an appropriate waveform. According to the waveform used for transmission, the radar sensor can be categorized as a pulsed radar sensor or Continuous-Wave (CW) radar sensor. They are briefly introduced in the following section.

1.2 Review of Pulsed Radar Sensors and Continuous Wave Radar Sensors

1.2.1. Pulsed Radar Sensors

The pulsed radar sensor, also known as the time-domain radar sensor, typically employs a train of impulses, mono-pulses or modulated pulses, as the transmitting waveform (Figure 1.1). The first subsurface radar sensor was the impulse radar that measured the properties of coal [10]. The impulse radar transmits a short pulse train with a pulse repetition interval (*PRI*). Such an impulse can be generated by using avalanche transistors, step recovery diodes (SRD), or tunnel diodes to produce a high peak power or a pulse of short

duration [11],[12]. The pulsed radar sensors typically use the two-way travel time of the transmitted pulse to measure the range of a target.
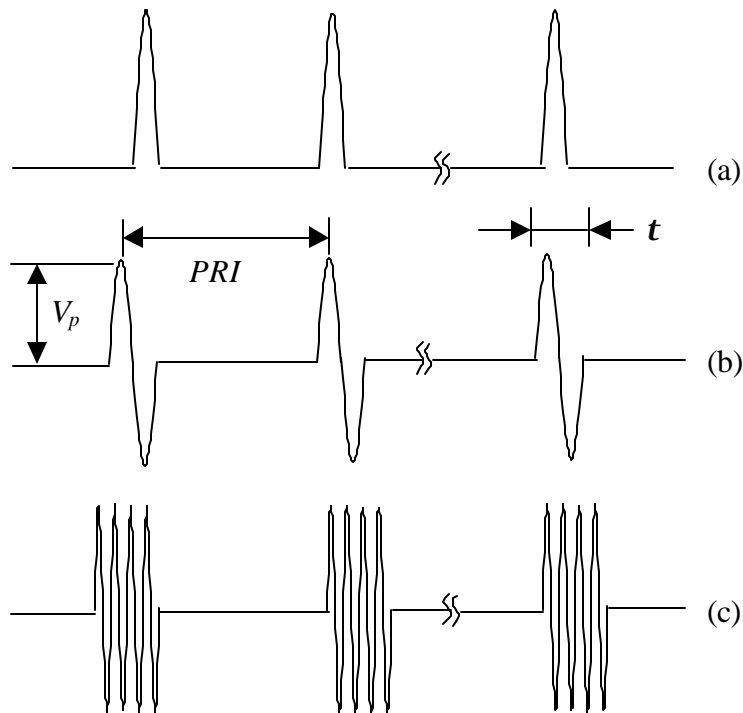
Figure 1.1 Waveforms of pulsed radar sensors; (a) impulse (b) mono-pulse, where t is the pulse width and V_p is the peak amplitude (c) modulated pulse.

The pulsed radar sensor has been widely used in many applications owing to its effective cost and simple structure. However, it has been found that this sensor is inappropriate and has severe constraints while operating as a High-Resolution Radar (HRR) sensor. To be a HRR sensor, the bandwidth (B) of the pulse needs to be increased as seen by equation (1.4). As the bandwidth of the pulse is increased by shortening the pulse width

(t), which in turn is restricted by available technologies, this type of sensor finds its usage effectively constricted by technological limitations and hence finds itself limited in high resolution based radar applications. It is worthwhile to note that the increased bandwidth degrades the receiver sensitivity, which results in decreasing the penetration depth.

Pulsed radars with a few hundred pico-seconds of pulse width can be designed, but only at very low power levels, up to a fraction of a watt of the average power [13]-[14]. This means that the pulsed radars cannot achieve both high range resolution and deep penetration simultaneously, unless pulse compression technique is used.

Alternatively, CW radar sensors can be implemented either as frequency-modulated continuous wave (FMCW) radar sensors or stepped-frequency continuous wave (SFCW) radar sensors. These sensors can achieve an average power much higher than that of a pulsed radar sensor. Both of these sensors are briefly discussed below.

1.2.2 Frequency-Modulated Continuous Wave Radar Sensors

FMCW radar sensors, also known as frequency domain radar sensors, have also been widely used as subsurface radar sensors, for instance, in measuring the thickness of a coal layer and detecting buried objects under the ground [15]-[17].

Figure 1.2 shows the FMCW radar sensor using a beat frequency (f_d) to seek the range (R) information of a target, as defined by

$$R = \frac{c\mathbf{t}}{2} = \frac{cf_d}{2m} \qquad\qquad 1.5$$

where m is the rate of sweeping frequency and the beat frequency accounts for the relative time delay ($\mathbf{t}$) of the transmitted signal to the returned signal.
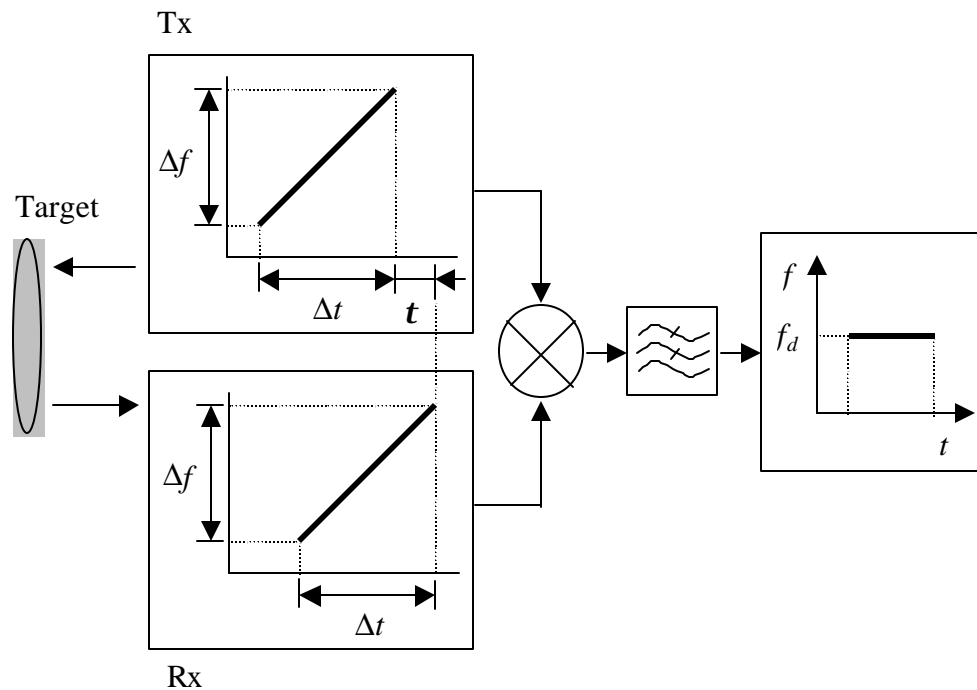
Figure 1.2 FMCW radar sensor.

An important characteristic of FWCW radar sensors is that the rate of sweeping frequency (m) should be carefully observed to obtain a satisfactorily accurate range of the target. However, it is quite difficult to achieve this specification over a wide band, due to the non-linearity of the voltage-controlled oscillator (VCO). Moreover, its wide bandwidth degrades the receiver's sensitivity, which results in reducing penetration depth. Hence, these drawbacks limit the FMCW radar sensor in some applications that need a greater degree of accuracy.

1.2.3 Stepped-Frequency Continuous Wave Radar Sensors

The SFCW radars, also known as frequency-domain radar sensors, transmit and receive consecutive trains of N frequencies changed by the frequency step (Δf). More details are given in Chapter III. Basically, the SFCW radar transforms the amplitudes (A_i) and phases ($\boldsymbol{f}_i$) of the base-band I and Q signals in frequency domain to a synthetic pulse in time domain to find the range (R) of a target [18], as defined by

$$I_i = A_i \cos \boldsymbol{f} = A_i \cos\left(-\frac{\boldsymbol{w}_i 2R}{c} \right) \qquad 1.6a$$

and

$$Q_i = A_i \sin \boldsymbol{f} = A_i \sin\left(-\frac{\boldsymbol{w}_i 2R}{c} \right) \qquad 1.6b$$

The advantages of SFCW radar sensors are as follows [19],[20]: Firstly, it has a narrow instantaneous bandwidth that significantly improves the receiver's sensitivity while

maintaining the average power. Secondly, it can transmit a high average power, resulting in a deeper penetration, due to the use of CW signals. Thirdly, the non-linear effects caused by the inherent imperfections of the transmitter and receiver can be corrected through appropriate signal processing. Furthermore, the received signals propagated through dispersive media can be accurately compensated through signal processing if the properties of the media are known, as the system transmits only one frequency at a particular instant of time. Lastly, the Analog-to-Digital (A/D) converter uses a very low sampling frequency, due to low frequency of the base-band I/Q signals. This enables greater precision and ease in designing the circuits.

On the flip side, a few disadvantages of the SFCW radar sensors include their high complexity and cost. However, owing to the impending ramifications due to the above advantages, there is a significant impetus for exhaustive research in this field.

1.3 Status of Stepped-Frequency Continuous Wave Radar Sensors

The concept of the stepped-frequency technique was first presented to detect buried objects by Robinson at Stanford research Institute in 1972 [21], but active research began only in the early nineties. An SFCW sensor operated at 0.6-1.112-GHz was developed for detecting moisture content in the pavement subgrade by Pippert et al. in 1993 [22]. Another SFCW radar sensor was developed at 490-780-MHz for detection of buried objects by Langman in 1996 [23] while a 10-620-MHz system was reported by Stickely in 1997 [24]. Langman et al. also developed a microwave SFCW radar sensor operating in the 1-2-GHz

was presented for detecting landmines in 1998 [3]. Recently, a Network Analyzer was used as a SFCW radar sensor at 0.5-6 GHz to detect concrete cracks by Huston in 1998 [25].

Most of the reported microwave SFCW radar sensors as subsurface radar sensors operate at low frequencies with insufficient bandwidths, which cause poor lateral and vertical resolution. A SFCW radar sensor is required to be of smaller size, lighter weight, finer resolution and better accuracy for usage in various applications. In practice, an accurate sensor assessing pavement layers is essential for pavement management during or after constructing the pavement. Portability is also quite an important issue, as radar sensors are also required to detect and localize mines of very small sizes during or after a war, so they need a fine resolution and should be lightweight. In addition, a small and accurate radar sensor is needed to monitor displacement of liquid levels in a stringent environment.

In order to reduce size and weight, the circuits of the sensor should be integrated using MICs and MMICs, and the antennae should be small with the possibility for a seamless connection. A wide bandwidth can promise a fine range resolution (Eq. 1.4) and a good lateral resolution can be achieved with a short wavelength as discussed later in Chapter III. To satisfy these requirements, ultra-wideband (UWB) and high frequency radar sensors need to be developed.

1.4 Proposed Stepped-Frequency Continuous Wave Radar Sensors

A microwave SFCW radar sensor operating at low frequencies can satisfy both deep penetration and fine range resolution simultaneously for subsurface sensing, and is thus attractive for subsurface evaluation such as measuring the thickness of the pavement layers. But, there is no such SFCW radar sensor, completely realized using MICs, and operated over a decade of frequency bandwidth that has been reported for subsurface sensing.

Similarly, a millimeter-wave SFCW radar sensor can achieve both vertical and lateral resolution very finely for surface and subsurface sensing. Yet, no millimeter-wave SFCW radar sensor, completely realized using MICs and MMICs, operating in Ka-band as a surface and subsurface radar sensor, has been developed.

For SFCW radar sensors, both homodyne and super-heterodyne schemes need a quadrature demodulator producing I and Q components to preserve the amplitude and phase information of the targets. However, the homodyne scheme would yield large phase errors in the wideband SFCW radar sensor, due to difficulties in designing the quadrature demodulator for such a wide bandwidth. Alternately, the super-heterodyne scheme has an advantage of using a much lower frequency, as well as a single Intermediate Frequency (IF) at which it is relatively easy to compensate for the quadrature demodulator errors. Therefore, the super-heterodyne scheme is more preferable for SFCW radar sensors operated in wideband width than the homodyne.

In this dissertation, two new SFCW radar sensor systems are presented for the first time. Each system includes transceiver, antenna, and signal processing parts. The transceivers

of both radar sensors are based on the coherent super-heterodyne architecture and are integrated with MICs and MMICs. The antennae are suitable for an integrated system due to their seamless connection and have been fabricated locally. The one intended for the microwave SFCW radar sensor system was tested and applied to the system while the other for the millimeter-wave SFCW radar sensor system was tested for potential usage in the system. Signal processing was developed using LabView to sample the base-band I and Q signals, synchronize the digitized I and Q signals, reform them, and transform the reformed data from the frequency domain into the time domain. In addition, a new simple yet effective and accurate procedure was introduced to compensate the common amplitude deviations and non-linear phase errors of the complex I/Q vectors due to the inherent imperfections of the system. Consequently, it can be stated that the performance of the two SFCW radar sensor systems was accurately appraised with intended usage for subsurface and surface radar sensors applications and is described in much detail in the forthcoming chapters.

CHAPTER II

SUBSURFACE RADAR SENSOR ANAYSIS

2.1 Introduction

Understanding the behavior of electromagnetic (EM) waves is important to the design of surface or subsurface radar sensors employing EM waves. This chapter presents a theoretical analysis from an electromagnetic perspective. The above mentioned sensors transmit EM energy through the transmitting antenna to targets (or objects) such as sand, soil, pavement, wood, liquid, mines, etc., and receive EM energy reflected back from targets through the receiving antenna.

The most important terms in radar sensors are "resolution" and "penetration depth". The range resolution determined by pulse shape is discussed in more detail in Chapter III. On the other hand, the penetration depth is determined by various parameters. Therefore, the penetration depth of a radar sensor is intensively focused in this chapter. Some are controllable by the designer, but others are dependent upon the propagation media and individual targets. The attenuation constant, wave velocity, reflection and transmission coefficients, spreading loss, and Radar Cross Sections (RCSs) of targets are those parameters of the radar sensor that cannot be adjusted by the designer. On the other hand, the transmitting power, antenna gain, frequency of the EM wave, and the receiver's sensitivity are controllable by the designer.

The EM waves of subsurface radar sensors propagate into materials with a wave velocity that associates them with the electrical properties of the materials. However, they also suffer from attenuation losses that are related to the material properties. The attenuation and velocity of EM waves in a given material are important parameters for radar sensors that aid our understanding of how EM waves propagate, what they look like at a specific time and location in the material, how much power loss arises, and how thick the material is.

If EM waves encounter a dielectric discontinuity that results from a sudden variation of material properties, part of the energy of the incident wave will be reflected, and the other part of it will be transmitted. When a plane EM wave is incident obliquely on the interface with a polarization, its reflection and transmission coefficients are governed by Fresnel's equation, while the transmitted and reflected angles are determined by Snell's Law [26].

The attenuation constant and wave velocity will affect the reflected power in the dielectric medium. The reflection and transmission coefficients, as well as the incident angle and the Radar Cross Section (RCS) will affect the reflected power at the dielectric discontinuity.

The penetration depth is related to the transmitting power and the receiver's sensitivity, which estimates the minimum signal level that can be detected. This sensitivity is affected by the input noise bandwidth, receiver noise figure, and the required signal-to-noise ratio (SNR). In addition, the higher the frequency, the greater the attenuation that will be incurred in the propagation medium.

Consequently, a radar equation including the maximum penetration depth of the multi-layered half-spaces similar to the pavement layers will be derived with the aid of image theory, assuming that a plane wave is incident on homogeneous layers. The maximum penetration depth is also expressed in terms of the radar sensor's parameters.

2.2 Electromagnetic Wave Propagation

When EM waves propagate into a source free and lossy homogeneous medium, assuming harmonic time dependence fields, Maxwell's equations in phasor form are given by [27]

$$\nabla \times \overline{E} = -jw\overline{B} \qquad\qquad 2.1a$$

$$\nabla \times \overline{H} = jw\overline{D} + \overline{J} \qquad\qquad 2.1b$$

$$\nabla \cdot \overline{D} = 0 \qquad\qquad 2.1c$$

$$\nabla \cdot \overline{B} = 0 \qquad\qquad 2.1d$$

where $\overline{E}$ is the electric field, $\overline{H}$ is the magnetic field, $\overline{B}$ is the magnetic induction, $\overline{D}$ is the electric displacement and $\overline{J}$ is the electric current.

When EM fields are in a material, the electric field, the magnetic field, the magnetic induction, the electric displacement and the electric current are all related to each other by constitutive relations such as [27]

$$\overline{D} = e\,\overline{E} \qquad\qquad\qquad 2.2a$$

$$\overline{B} = m\overline{H} \qquad\qquad\qquad 2.2b$$

$$\overline{J} = s\,\overline{E} \qquad\qquad\qquad 2.2c$$

where $e = e_0 e_r$,which is the product of the dielectric permittivity of the free space e_0 (≈ 8.85

$\times 10^{-12}$ F/m) and the relative dielectric permittivity of the material e_r , the complex permittivity

of the material, $m = m_0 m_r$, which is the product of the magnetic permeability of the free space

m_0 ($\approx 4\pi \times 10^{-7}$ H/m) and the relative magnetic permeability of the material m_r, the complex

permeability of the material and the conductivity of the material s .

Substituting (2.2a) - (2.2c) into (2.1a) and (2.1b) leads to Maxwell's curl equations

[27]

$$\nabla \times \overline{E} = -jwm\overline{H} \qquad\qquad\qquad 2.3a$$

$$\nabla \times \overline{H} = jw\left(e' - j\frac{s}{w}\right)\overline{E} = jwe_c\overline{E} = jw(e' - je'')\overline{E} \qquad\qquad 2.3b$$

where $e_c(\omega) = e'(\omega) - je''(\omega) = e(\omega) - js(\omega)/w$ is the complex dielectric permittivity.

In order to explain in detail how the waves propagate in a dielectric material (i.e., a lossy medium), modified Helmholtz equations, which are derived from Maxwell's equations and constitutive equations, are needed as depicted in [28]

$$\nabla^2 \overline{E} + w^2 \boldsymbol{me}_c \overline{E} = \nabla^2 \overline{E} - \boldsymbol{g}^2 \overline{E} = 0 \qquad \qquad 2.4a$$

$$\nabla^2 \overline{H} + w^2 \boldsymbol{me}_c \overline{H} = \nabla^2 \overline{H} - \boldsymbol{g}^2 \overline{H} = 0 \qquad \qquad 2.4b$$

where γ is the complex propagation constant of the waves in the medium and defined by [28]

$$\boldsymbol{g} = \boldsymbol{a} + j\boldsymbol{b} = jw\sqrt{\boldsymbol{me}_c} = jw\sqrt{\boldsymbol{me}}\sqrt{1 - j\frac{\boldsymbol{s}}{\boldsymbol{we}}} \qquad \qquad 2.5$$

or

$$\boldsymbol{g} = jw\sqrt{\boldsymbol{me}'}\sqrt{1 - j\left(\frac{\boldsymbol{e}''}{\boldsymbol{e}'}\right)} = jw\sqrt{\boldsymbol{me}'}\sqrt{1 - j\tan\boldsymbol{d}} \qquad \qquad 2.6$$

where $\boldsymbol{a}$ is the attenuation constant (Np/m), $\boldsymbol{b}$ is the phase constant (rad/m), and the loss tangent tan$\boldsymbol{d}$ is defined as the ratio of the real to the imaginary part of the complex permittivity $\boldsymbol{e}_c$ as in [28]

$$\tan\boldsymbol{d} = \frac{\boldsymbol{e}''}{\boldsymbol{e}'} = \frac{\boldsymbol{s}}{\boldsymbol{we}} \qquad \qquad 2.7$$

2.2.1 Plane Wave Solution

Assuming a plane wave, the electric and magnetic fields propagating into a lossy medium in the $+z$ direction in the sinusoidal steady state are obtained by solving Helmholtz equations (2.4a) and (2.4b) as

$$E_x(z,t) = E_{x0} e^{-az} \cos(wt - bz) \qquad \text{2.8a}$$

and

$$H_y(z,t) = \frac{E_{x0}}{|h_c|} e^{-az} \cos(wt - bz - f_{h_c}) \qquad \text{2.8b}$$

where $h_c = |h_c| \angle f_{hc}$ is the complex intrinsic impedance of the lossy medium and E_{x0} and H_{x0} are the electric and magnetic field intensities at $z = 0$.

The equations (2.8a) and (2.8b) account for both the attenuation and the phase constants (a and b). This means that if we know the attenuation and phase constants of the medium at a specific frequency w, it is possible to predict the fields at a specific time t and distance z.

From equations (2.8a) and (2.8b), if the transmitting signal is captured in the receiver at a distance z, the amplitude of the electric or magnetic field is attenuated by

$$A = -az \, 20 \log e = -8.686 az \qquad \text{2.9}$$

where A is the attenuation in dB.

Therefore, knowing the value of the attenuation constant of the propagation medium is important in predicting the power of the received field. When the transmitting antenna emits

a plane wave, as can be seen from equations (2.8a) and (2.8b), the time-averaged power density $S(z)$ at a distance z is

$$\left|S(z)\right| = \left|\frac{1}{2}\text{Re}\left\{E \times H^*\right\}\right| = \frac{\left|E_{x0}\right|^2}{2\left|h_c\right|}\cos f_{h_c} e^{-2az}$$

2.10

where H^* denotes the complex magnetic field intensity conjugate.

This demonstrates that the power density of the plane wave in a lossy medium decreases exponentially at a rate of e^{-2az} as the plane wave travels in the direction of z.

2.2.2 Attenuation and Phase Constants in Different Media

For surface penetrating radars, the parameters of interest are the attenuation constant and wave velocity of EM waves in their propagation media. The attenuation constant decreases the power of the received EM waves that determines the maximum range or penetration depth. The phase constant affects the wave velocity that is related to the target's range. The practical propagation media are lossy and usually categorized into two types; high loss and low loss materials. They are described elaborately as below.

From equation (2.6), the attenuation and phase constants (which are the real and imaginary parts of the propagation constant, respectively) of a medium that is defined as lossy, are given by [28]

$$a = w\sqrt{me'}\sqrt{\frac{1}{2}\left(\sqrt{1+\tan^2 d} - 1\right)}$$

2.11a

and

$$b = w\sqrt{me'}\sqrt{\frac{1}{2}\left(\sqrt{1+\tan^2 d}+1\right)} \qquad 2.11b$$

From equation (2.11a), it is evident that the attenuation constant is a function of the frequency.

A. High loss material

As a benchmark, if $tan d \gg 1$ (i.e., $s \gg we$), the medium is termed as one with high loss. From equation (2.5) the attenuation and phase constants are given by [28]

$$a \approx \sqrt{\frac{wms}{2}} \qquad 2.12a$$

and

$$b \approx \sqrt{\frac{wms}{2}} \qquad 2.12b$$

where the attenuation and phase constants are dependent upon the frequency and conductivity of the material.

B. Low loss material

Low loss material is usually a good insulator due to its low conductivity. If $tan d \ll$ 1 (i.e., $s \ll we$), the material is said to be of low loss. Equation (2.6) is approximated by the binomial as

$$g \approx jw\sqrt{me'}\left[1-\frac{1}{2}(j\tan d)+\frac{1}{8}\tan^2 d\right]$$ 2.13

From equation (2.13), the attenuation constant (the real part of the propagation constant) is

reduced to

$$a \approx w\sqrt{me'}\,\frac{\tan d}{2}$$ 2.14a

The phase constant (the imaginary part of the propagation constant) is approximated as

$$b \approx w\sqrt{me'}\left(1+\frac{1}{8}\tan^2 d\right)\approx w\sqrt{me'}$$ 2.14b

The common pavement materials of interest in subsurface radar can be considered to

be low loss and non-magnetic materials (i.e., $m = m_0$) [29],[30]. Table 2.1 shows an example

of the measured properties of the pavement, typically layered asphalt above the base material

and subgrade [8]. A measurement using the Network Analyzer at 3GHz was conducted by

the Texas Transportation Institute (TTI) that is shown in Table 2.1.

Table 2.1 Electrical properties of pavement.

	Asphalt	Base	Subgrade
ε_r'	5-7	8-12	>20
ε_r''	0.035	0.2-0.8	N/A

Figure 2.1 illustrates that while the loss tangent is varied, the attenuation constants of a medium calculated by equation (2.14a), approximated from equation (2.11a), are not much different than those obtained by equation (2.11a). Therefore, the practical pavements, as shown in Table 2.1, can be assumed to be as low loss for calculating the attenuation constants. However, dielectric permittivity and electrical conductivity are both frequency dependent. With increasing frequency, conductivity loss reduces and dipolar losses associated with the water relaxation of the material increases. Consequently, the total loss is increased [31].
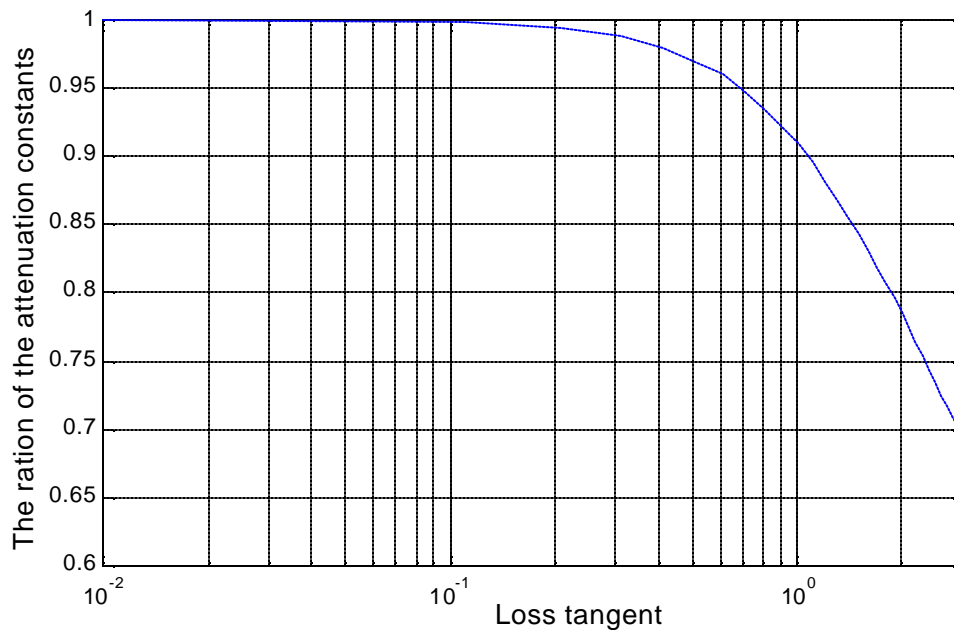
Figure 2.1 The loss tangent vs. the ratio of the attenuation constants calculated by equation (2.11a) to those calculated by equation (2.14a).

2.2.3 Wave Velocity

In a non-dispersive medium, the wave velocity is independent of frequency. On the other hand, in a dispersive medium, different frequency components propagate with different velocities causing a distortion of the signal due to variations in the phase constant at different frequencies. The phase velocity v_p (called the wave velocity), which keeps a constant phase point on the wave, can be written as

$$v_p = \frac{\partial z}{\partial t} = \frac{w}{b} \qquad\qquad 2.15$$

The phase velocity of an EM wave is expressed in terms of the speed of light in a material in equation (2.16). From equations (2.14b) and (2.15), the wave velocity in a low loss material and non-magnetic material is found to be

$$n = \frac{c}{\sqrt{e'_r}}\left[1 - \frac{1}{8}\left(\tan^2 d\right)\right] \approx \frac{c}{\sqrt{e'_r}} \qquad\qquad 2.16$$

The wave velocity is relatively consistent over the common subsurface radar frequency range of 10-1000MHz at conductivities of less than 0.1 S/m. However, it is increasingly independent of conductivities in the 1-10-GHz region where the water relaxation effect is dominant [31]. Therefore, dispersive characteristics of materials at high frequencies need be considered for the accuracy of the measurement.

2.3 Scattering of a Plane Wave Incident on Targets

EM waves incident on a target will be scattered, with a portion of the scattered energy captured by the receiving antenna. Since the electromagnetic properties of the target affect the reflected power, the received power can be estimated if the properties of the target and the propagating medium are known.

2.3.1 Scattering of a Plane Wave Incident on a Half-Space

If an EM wave is incident on an interface, part of its energy is reflected and the other part is transmitted through it. In the case of a smooth and flat surface, the reflection coefficients depend upon the polarization of the incident wave, the angle of incidence, and the wave impedances of the materials [32]. The polarization is determined by the angle formed between the electric field vector and the incident plane [28]. If the electric field is in the incident plane, the incident plane wave has a parallel polarization, as shown in Figure 2.2, where the incident plane is on the xy plane. Alternately, if the electric field is incident normally on the plane, the incident plane wave is in perpendicular polarization.

A. Reflection at a single interface

If a boundary exists between two media, by applying the boundary conditions (which requires continuity of the tangential components of the E- and H-field at the boundary), the reflection coefficients G_{par} and G_{per} of the incident wave in the parallel and perpendicular polarizations are given by [28]

$$\Gamma_{par} = \frac{\boldsymbol{h}_2 \cos \boldsymbol{f}_t - \boldsymbol{h}_1 \cos \boldsymbol{f}_i}{\boldsymbol{h}_2 \cos \boldsymbol{f}_t + \boldsymbol{h}_1 \cos \boldsymbol{f}_i} \qquad\qquad 2.17a$$

$$\Gamma_{per} = \frac{\boldsymbol{h}_2 \cos \boldsymbol{f}_i - \boldsymbol{h}_1 \cos \boldsymbol{f}_t}{\boldsymbol{h}_2 \cos \boldsymbol{f}_i + \boldsymbol{h}_1 \cos \boldsymbol{f}_t} \qquad\qquad 2.17b$$

where $\boldsymbol{f}_i$ and $\boldsymbol{f}_t$ are the incidents and transmitted angles; $\boldsymbol{h}_1$ and $\boldsymbol{h}_2$ are the intrinsic impedances of mediums 1 and 2, respectively.
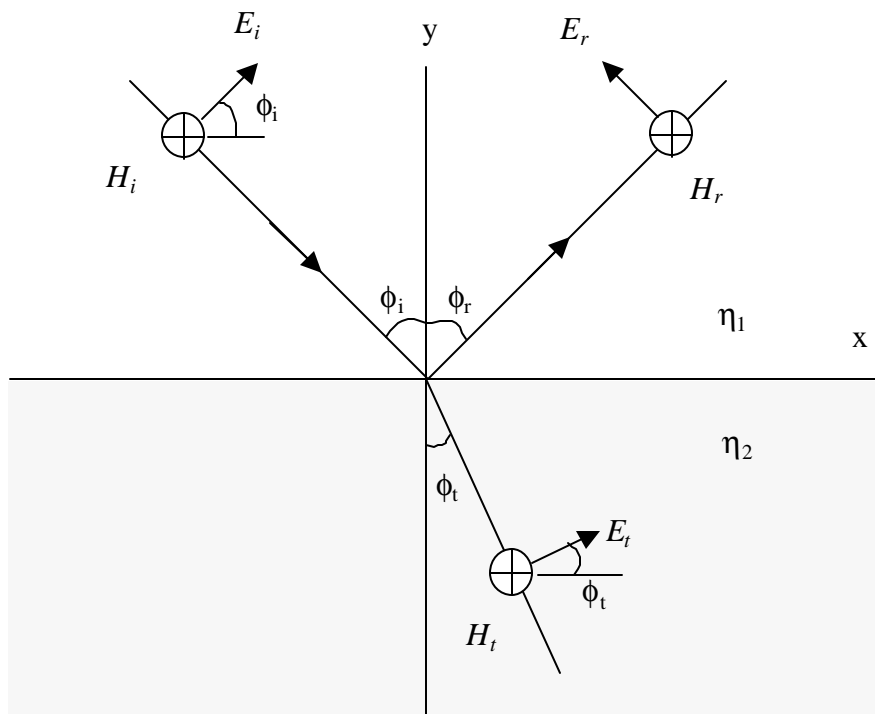
Figure 2.2 A plane wave with a parallel polarization incident on a dielectric interface.

If a parallel-polarized wave is incident on the interface through a lossy medium 1, as shown in Figure2.3, the time-averaged power density $S_r(R)$ reflected from the interface at R, which is the distance from the interface, is found by using equation (2.10) as

$$S_r(R) = \left|\Gamma_{par}\right|^2 \exp(-4\boldsymbol{a}_1 R) S_i(R) \qquad\qquad 2.18$$

where $S_i(R)$ is the incident time-averaged power density at R, $\boldsymbol{a}_1$ is the attenuation constant of the lossy medium 1.
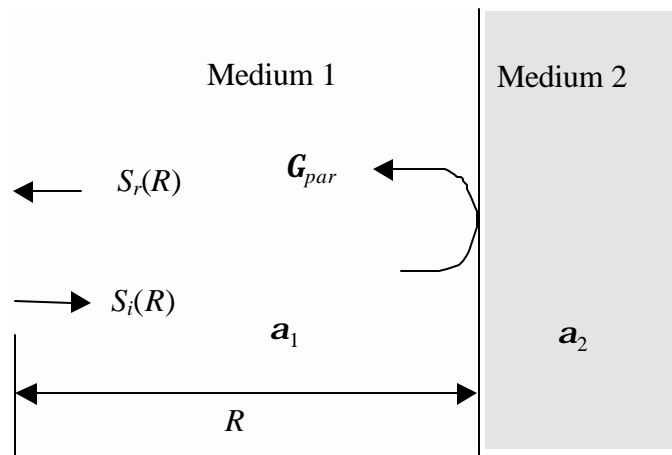
Figure   2.3 Received power density attenuated by the reflection at the interface and the attenuation in the propagating medium.

Figure 2.4 shows the magnitudes of the reflection coefficients for both the parallel and the perpendicular polarizations of a plane wave that is incident on a smooth flat surface, placed at distance z from the transmitting antenna, with varied angles when the wave

incidents from free space to those lossless media with relative dielectric constants values ϵ_r = 2, 4, 6, 8 and 10.
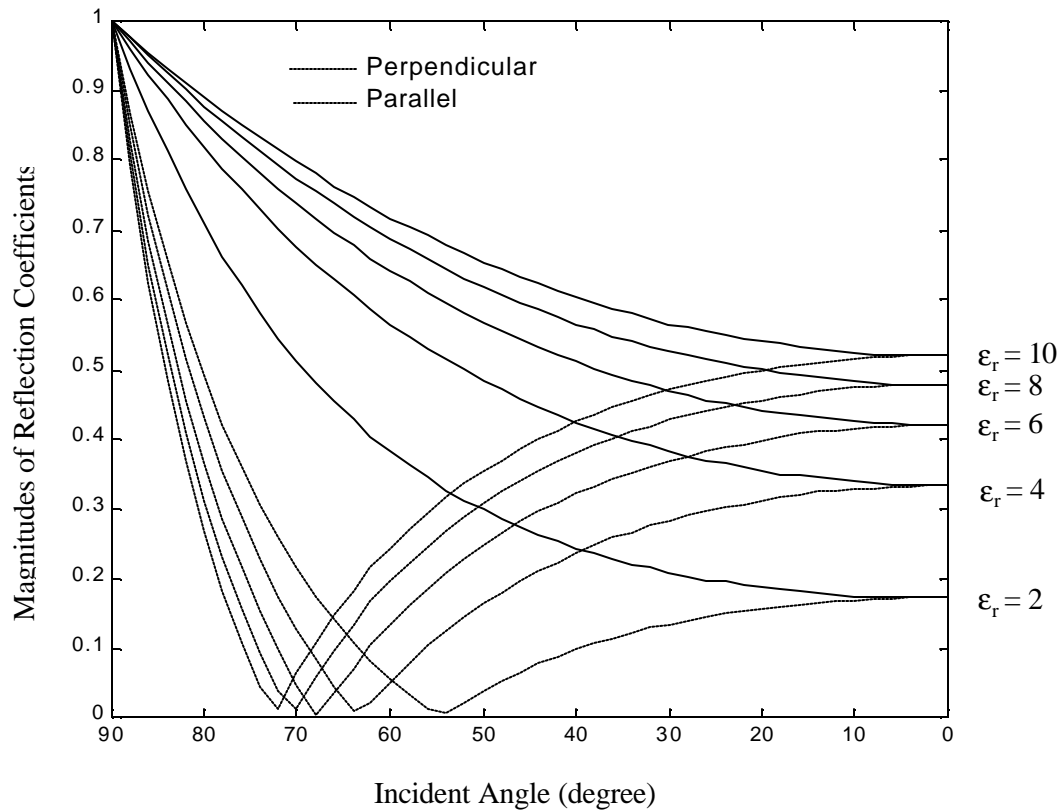
Figure 2.4 Magnitudes of reflection coefficients of a plane wave incident on different dielectric materials from free space with varied angle.

The phase of the reflected signal from a dielectric interface is determined by the phase of the reflection coefficient [33]. Assuming a normal incidence of a plane wave on a dielectric interface with a parallel polarization, equation (2.17a) can then be reduced to

$$\Gamma_{par} = \frac{h_2 - h_1}{h_2 + h_1}$$ 2.19

In case of a low loss and non-magnetic material, such as pavement as seen in Section 2.2, the intrinsic impedance is almost a real value $h \approx \sqrt{m_0 / e_0 e_r'}$. Therefore, from equation (2.19), we have

$$\Gamma_{par} \approx \frac{\sqrt{e_{r1}'} - \sqrt{e_{r2}'}}{\sqrt{e_{r1}'} + \sqrt{e_{r2}'}}$$ 2.20

where e'_{r1} and e'_{r2} are the real parts of the relative dielectric permittivity of those materials in regions 1 and 2, respectively.

To verify equation (2.20) in practical the pavement, as shown in Table 2.1, the reflection coefficients at the interface in between the asphalt and base layers were calculated using equations (2.19) and (2.20), while the imaginary part of the dielectric permittivity of the base layer was varying in the range of 0.2-0.8, as shown in Table 2.1. As expected, the reflection coefficients obtained from equation (2.20) show at most a 1% error, as shown in Figure 2.5. Therefore, an assumption of lossless material is quite valid in calculating the reflection coefficients of the pavement materials. Similarly, it can be deduced that the transmission coefficients can also be calculated under the assumption of lossless materials.
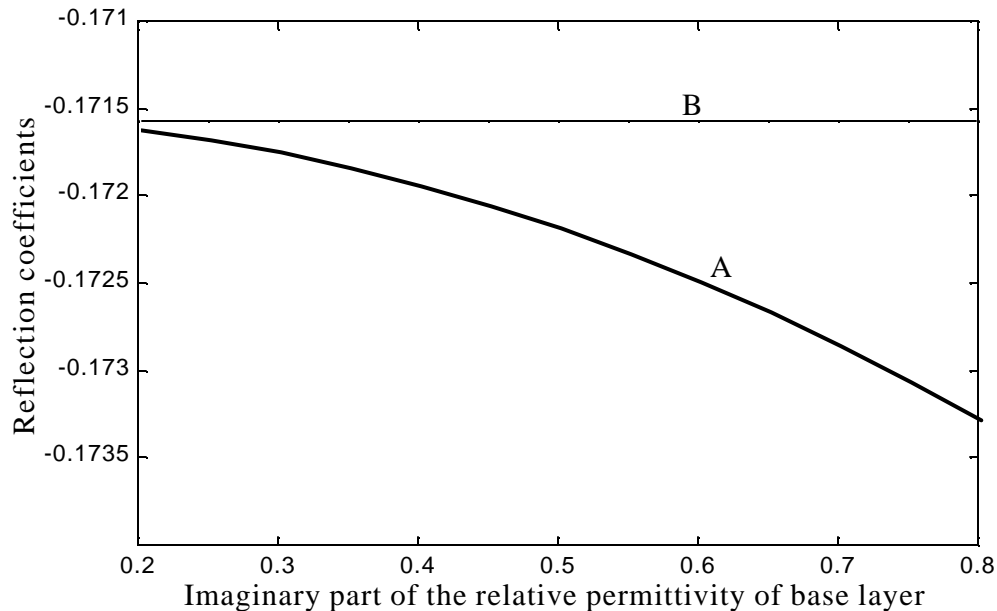
Figure 2.5 Reflection coefficients in normal incident where A is calculated using equation (2.19) and B is calculated using equation (2.20) with an assumption of low loss.

From equation (2.19), the phase of the reflection coefficient is either 0 or π radians. For instance, if the signal is incident from a material with lower dielectric constant to one with a higher dielectric, the polarity of the reflected signal is opposite to that of the incident signal. This happens with most practical realizations of the subsurface radar sensors, such as with the assessment of pavements or the detection of mines. On the contrary, when the incident signal propagates from a material with higher dielectric constant to one with a lower dielectric, the reflected signal is returned with the same polarity as the incident signal. The opposite polarity of the reflected signal as compared to the incident signal and the result can

be used to detect an air void, which might indicate a defect in the pavement, bridge, laminated wood, wall and so on.

However, in case of a lossy material, the reflection coefficient would be a complex value due to the complex intrinsic impedance of the lossy material. The phase of the reflected signal would then be in between 0 and 2π radians, depending on the losses of various materials. In addition, the phase of the reflection coefficient will also be changed by the frequency of the incident signal, since the dielectric permittivity is a function of the frequency of the incident signal. Therefore, the phases of the reflection coefficients in lossy media are found if the dielectric permittivities over the band of interest are known.

B. Reflection and transmission of a plane wave at the interfaces of multi-layered mediums

Subsurface radar sensors investigating the pavement will encounter multiple layers under the pavement. In order to recognize the reflected power from the interfaces of the pavement, the reflection coefficients, as well as the transmission coefficients at the interfaces, should be known. The transmission coefficients $\boldsymbol{T}_{par}$ and $\boldsymbol{T}_{per}$ of the incident wave in both parallel and perpendicular polarizations, respectively, are given by [28]

$$\mathrm{T}_{par} = \frac{2\boldsymbol{h}_2 \cos\boldsymbol{f}_i}{\boldsymbol{h}_2 \cos\boldsymbol{f}_t + \boldsymbol{h}_1 \cos\boldsymbol{f}_i} \qquad\qquad 2.21\mathrm{a}$$

$$\mathrm{T}_{per} = \frac{2\boldsymbol{h}_2 \cos\boldsymbol{f}_i}{\boldsymbol{h}_2 \cos\boldsymbol{f}_i + \boldsymbol{h}_1 \cos\boldsymbol{f}_t} \qquad\qquad 2.21\mathrm{b}$$

where f_i and f_t are the incidents and the transmitted angles; h_1 and h_2 are the wave impedances of mediums 1 and 2, respectively.

The wave passing through an interface will be refracted by Snell's Law, which is defined as [28]

$$\frac{\sin f_i}{\sin f_t} = \frac{\sqrt{e'_{r2}}}{\sqrt{e'_{r1}}} \qquad 2.22$$

where $e\varphi_1$ and $e\varphi_2$ are the relative dielectric constants of mediums 1 and 2, respectively.

When an incident wave traverses through multiple layers, as shown in Figure 2.6, the total reflected field E_{r_total} can be expressed approximately by the superposition of all reflected waves,

$$E_{r\_total} \approx E_{r1} + E_{r2} + E_{r3} + E'_{r2} \qquad 2.23$$

where E_{r1}, E_{r2}, and E_{r3} are the single-reflected fields at the 1st, 2nd and 3rd interfaces, respectively, and $E\varphi_2$ is the double- reflected field within region 1. Then, these reflected waves can be expressed by
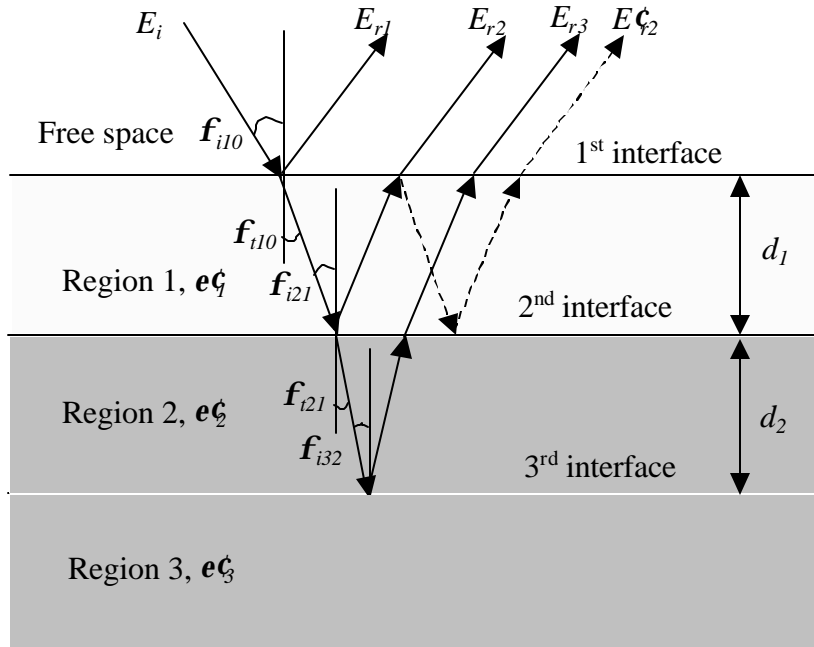
Figure 2.6 Reflected waves at the interfaces of multi-layered half-spaces.

$$E_{r1} = \Gamma_{10} E_i \qquad\qquad 2.24a$$

$$E_{r2} = T_{10}\Gamma_{21}T_{01}E_i \exp\left(-\frac{2\boldsymbol{a}_1 d_1}{\cos \boldsymbol{f}_{t10}}\right) \qquad\qquad 2.24b$$

$$E_{r3} = T_{10}T_{21}\Gamma_{32}T_{12}T_{01}E_i \exp\left(-\frac{2\boldsymbol{a}_1 d_1}{\cos \boldsymbol{f}_{t10}}\right)\exp\left(-\frac{2\boldsymbol{a}_2 d_2}{\cos \boldsymbol{f}_{t21}}\right) \qquad\qquad 2.24c$$

$$E'_{r2} = T_{10}\Gamma_{21}\Gamma_{01}\Gamma_{21}T_{01}E_i \exp\left(-\frac{\boldsymbol{a}_1 d_1}{\cos \boldsymbol{f}_{t10}}\right) \qquad\qquad 2.24d$$

where Γ_{10} and T_{10} indicate the reflection and transmission coefficients of the wave incidents

from region 0 to region 1, respectively, $\boldsymbol{f}_{t10}$ indicates the transmitted angle of the wave

incident from region 0 to region 1, $\boldsymbol{a}_1$ and $\boldsymbol{a}_2$ are the attenuation constants of media 1 and 2,

respectively, and finally, d_1 and d_2 are the thicknesses of mediums 1 and 2, respectively. Therefore, the single-reflected field at each interface is generalized as

$$E_{rn} = \Gamma_{nn-1}\left[\prod_{m=1}^{n-1}\left(T_{mm-1}T_{m-1m}\right)\exp\left(-\frac{2\boldsymbol{a}_m d_m}{\cos \boldsymbol{f}_{tmm-1}}\right)\right]E_i \qquad 2.25a$$

and the double-reflected field in the region n is given by

$$E'_{rn} = \left(\Gamma_{nn-1}\right)^2 \Gamma_{n-2n-1}\exp\left(-\frac{2\boldsymbol{a}_n d_n}{\cos \boldsymbol{f}_{tnn-1}}\right)\left[\prod_{m=1}^{n-1}\left(T_{mm-1}\right)\left(T_{m-1m}\right)\right]E_i \qquad 2.25b$$

In practice, the reflection coefficients are smaller than their transmission coefficient counterpart, which results in ignoring the double-reflected field in the total reflected field. For simplicity, if the incident field is normal, the time-averaged power density $S_{rn}(R)$ reflected from the nth interface is given by

$$S_{rn}(R) = \left(\Gamma_{nn-1}\right)^2\left[\prod_{m=1}^{n-1}\left(T_{mm-1}\right)^2\left(T_{m-1m}\right)^2\right]\left[\prod_{k=1}^{n-1}\exp(-4\boldsymbol{a}_k d_k)\right]S_i(R) \qquad 2.26$$

where $S_i(R)$ is the incident time-averaged power density at R, $\boldsymbol{a}_k$ is the attenuation constant of the kth medium and R is the distance from the interface. Note that the returned power will be significantly decreased if the transmission coefficients are small.

The phase of the transmitted signal propagated through a dielectric interface between the two different dielectric materials is determined by the phase of the transmission coefficient. As expressed in equation (2.21a), the magnitude of the transmission coefficient will be a positive real value and the phase of the transmission coefficient can be between 0 and 2π radians. For lossless materials, the transmission coefficient will be a real value, which

leads to it having the same polarity as the incident signal. However, in case of lossy materials, the phase of the transmission coefficient can be any value between 0 and 2π radians. Note that the phase of the transmission coefficient depends upon the frequency of the incident signal, as well as the losses of the various materials.

Similarly, reflection and transmission coefficients in lossy media can be derived by the definitions provided by Fresnel and Snell [26]. However, the lossy medium has a complex permittivity, which leads to complex reflection and transmission coefficients. It can therefore be inferred that the reflected and transmitted waves would be attenuated in amplitude and modified in angle in a lossy medium, while the angle alone changes in a lossless medium.

2.3.2. Radar Cross Sections

For subsurface radar sensors that specifically detect and localize objects buried underground, the Radar Cross Sections (RCS) values of the objects to be identified should be known. The RCS constitutes an important parameter in the radar equation that is defined as the effective area that captures the transmitted signal and isotropically radiates all the incident power [34]. RCS provides to the radar equation some crucial characteristics of the desired target observed by a receiver. The definition of RCS , σ, is therefore given by [34]

$$\sigma = \frac{\text{power scattered toward source per unit solid angle}}{\text{incident power density at the target} / (4\pi)} \qquad 2.27$$

In other words,

$$s = \lim_{R \to \infty} 4pR^2 \frac{|E_s|^2}{|E_i|^2} \qquad\qquad 2.28$$

where E_s is the scattered field at the receiving antenna, E_i is the incident field at the target,

and R is the distance to the target. An infinity range means that the incident wave is a plane

wave.

Table 2.2 shows the theoretical RCS values of typical geometric shapes in optical

regions (i.e., $2\pi r/\lambda > 10$) [18] where the ratio of the calculated RCS to the real cross

sectional area of a sphere is 1. These values are very accurate as the RCS of a sphere is

independent of the frequency in the optical region. The most typical geometry is a half-space

for radar sensors that investigate the surface or subsurface of pavement consisting of an

asphalt layer, a base layer, and various subgrade layers. The half-space is considered to be

an infinite plate that can be either a smooth or a rough plate, according to roughness of that

plate [30].

Table 2.2 Radar cross sections of typical geometric shapes where λ is the wavelength.

Geometric Shapes	Dimension	RCS(σ)
Sphere	Radius r	πr^2
Flat plate	$r \times r$	$4\pi r^2/\lambda^2$
Cylinder	$H \times$ radius r	$2\pi r H^2/\lambda$

2.4 Radar Equation

The radar equation illustrates the significant characteristics of a radar system [34]. However, it is necessary to be modified for subsurface radar sensor accounting for the attenuation constants of the propagation media and wave velocity in the media. The modified radar equation includes the transmitted power P_t, the antenna gain G, the receiver sensitivity P_t, and wavelength of the transmitted wave λ, all of which are controllable by a radar designer. In addition, it takes into account for the RCS value of the target, the maximum penetration depth d_{max}, and the attenuation constant α of the propagation medium. Conversely, these parameters are not controllable by the radar designer. However, it is difficult to use in practical applications such as multi-layered pavement. Therefore, the radar equation needs to be derived for any subsurface radar sensor investigating pavement layers or buried objects under the ground to estimate its maximum penetration depth. For simplicity, the pavement layers and the ground are assumed to be half-spaces and a plane wave with a parallel polarization was used.

2.4.1 General Radar Equation

Power density S for a plane wave is proportional to $|E|^2$ as seen in equation (2.10). As seen in Figure 2.7, if the transmitted power P_t (which is the power at the input terminal of the transmitting antenna) is radiated into a lossless medium, it will be affected by the attenuation constant of that medium. The power density S at the target in range R is

$$S = \frac{P_t G_t}{4\boldsymbol{p} R^2} \qquad 2.29$$

where G_t is the transmitting antenna gain. By using equation (2.10), $|E_i|^2$ at the target can be expressed as

$$|E_i|^2 = \frac{|2\boldsymbol{h}_c|}{\cos \boldsymbol{f}_{h_c}} \frac{P_t G_t}{4\boldsymbol{p} R^2} \qquad 2.30$$

where E_i is the incident field at the target. If the received power P_r is captured by an antenna with an effective aperture A_{er}, the scattered power will be attenuated until it reaches the receiver antenna. Then, similarly, $|E_s|^2$ at the antenna of the receiver is

$$|E_s|^2 = \frac{|2\boldsymbol{h}_c|}{\cos \boldsymbol{f}_{h_c}} \frac{P_r}{A_{er}} \qquad 2.31$$

where E_s is the scattered field at the receiver antenna.

As a result, the received power in terms of RCS is obtained by substituting equations (2.30) and (2.31) into equation (2.28), which is the definition of RCS.

$$P_r = \frac{P_t G_t A_{er} \boldsymbol{s}}{(4\boldsymbol{p})^2 R^4} \qquad 2.32$$
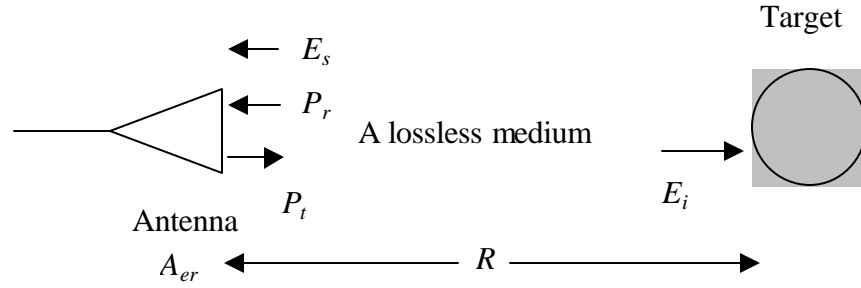
Figure 2.7 Configuration for radar equations in a lossy medium.

If the propagation medium is lossy, the attenuation of the medium needs to be involved. Also, a system loss L is added to account for the loss factor existent in the practical radar system itself [35]; for example the antenna polarization, mismatch, and efficiency and so on; then the equation can be modified as

$$P_r = \frac{P_t G_t A_{er} \boldsymbol{s} \exp(-4\boldsymbol{a}d)}{(4\boldsymbol{p})^2 R^4 L}$$ 2.33

where α and d are the attenuation constant and distance of the propagation medium, respectively, and the exponential term accounts for the loss of the medium as shown in equation (2.18) or (2.26).

In case of a monostatic system in which the transmitting antenna and the receiving antenna are the same or located in a proximate position [34], their corresponding gains are equal to G (i.e. $G_t = G_r = G$). However, the effective aperture of the receiving antenna expressed in terms of the antenna gain and the wavelength is [36]

$$A_{er} = \frac{G_r \boldsymbol{l}^2}{4\boldsymbol{p}}$$ 2.34

The radar sensor can detect signals returned from a target if the received power is higher than the receiver sensitivity S_i that is determined by the noise temperature (T), the noise bandwidth (B), the total noise figure (F) of the receiver and the signal to noise ratio (SNR). Figure 2.8 depicts the required minimum input signal level for the detection of a target.
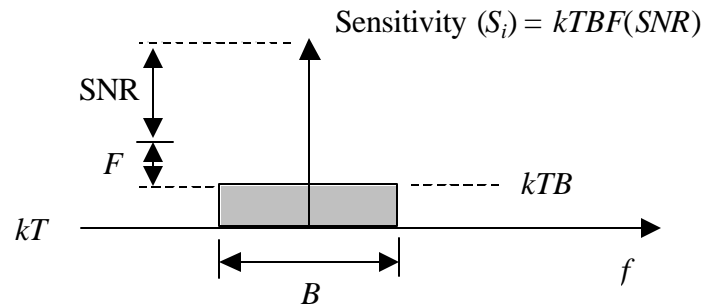
Figure 2.8 The required minimum input signal level or the sensitivity of a receiver where $N_i = kTB$ is the input noise power, $k = 1.38 \times 10^{-23}$ (J/K) is the Boltzmann constant, T is the standard noise temperature ($T = 290$ K), B (Hz) is the noise bandwidth, and F is the total noise figure of the receiver.

As shown in Figure 2.8, the minimum required input signal power is defined by [37]

$$S_i = kTBF(SNR) \hspace{3cm} 2.35$$

As a measure of the radar, the system performance factor *SF* of the radar sensor was defined in [9]:

$$SF = \frac{P_t}{S_i}$$
2.36

Note that this system performance factor is useful for radar equation. Consequently, the radar equation incorporating a maximum range R_{max}, obtained when the received power is equal to the receiver sensitivity, and the system performance factor is found from equations (2.33-36):

$$SF = \frac{(4\boldsymbol{p})^3 R_{max}^4 L}{G^2 \boldsymbol{l}^2 \boldsymbol{s} \exp(-4\boldsymbol{a}R_{max})}$$
2.37

Note that the maximum range R_{max} is also involved in the exponential term.

2.4.2 Radar Equation for Half-Spaces

For surface and subsurface radar sensors, the radar equation needs a modification, applying the definition of the reflection and the transmission on a half-space similar to the surface of the pavement or the ground. If a radar sensor transmits a plane wave and receives back a plane wave reflected from a half-space at the distance of R (Fig. 2.9a), then the received power at the receiver antenna derived by using image theory [30], as shown in Fig 2.9 b, is given by

$$P_r = \frac{P_t G_t A_{er}}{4p(2R)^2 L} \Gamma^2$$ 2.38

where Γ is the reflection coefficient of the half-plane.

From equations (2.32) and (2.38), the radar cross section of a half-space plate is found as

$$s = pR^2\Gamma^2$$ 2.39

This result is equal to the RCS of a half-space presented in [30]. Therefore, equation (2.38) is verified.

Target

G

P_r

Antenna P_t

A_{er} R

(a)

Target

G

Antenna P_t

P_r

Antenna

R R A_{er}

(b)
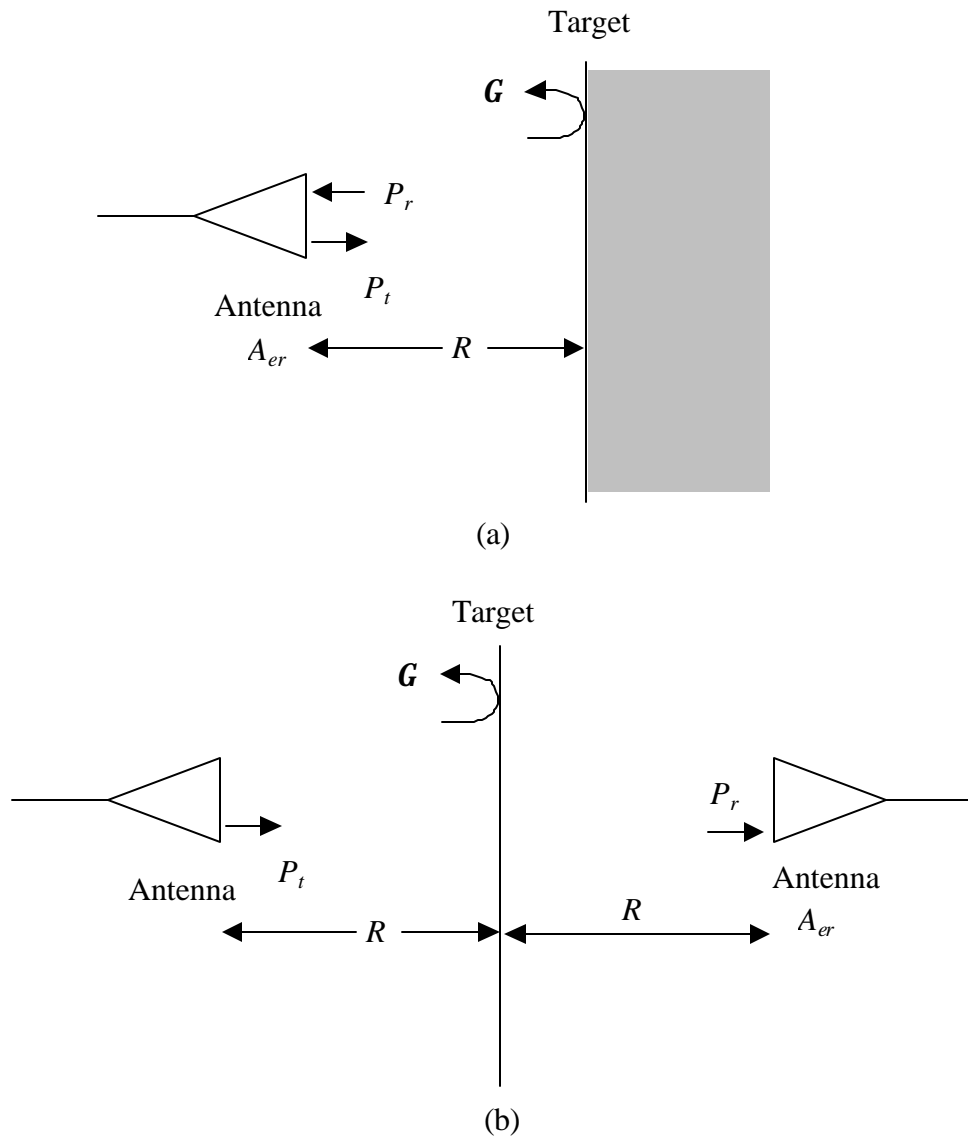
Figure 2.9 (a) A radar sensor receiving from a single half-space (b) equivalent to (a) when the image theory is used.
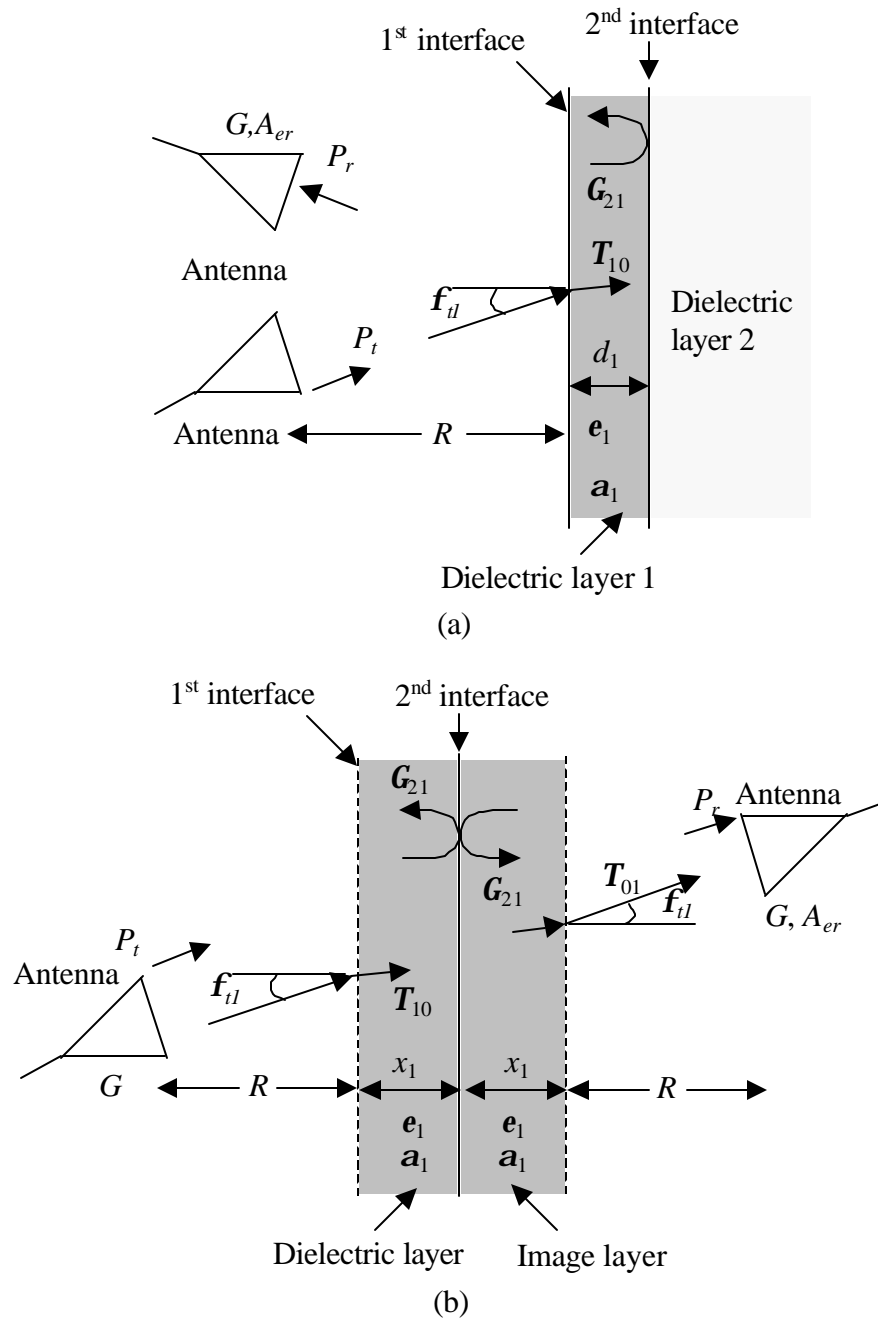
Figure 2.10 Subsurface radar sensors receiving from the 2nd interface: (a) geometry of the pavement (b) geometry of the pavement when the image theory is applied.

With extending the image theory into subsurface radar sensors investigating multi-layered structures, as shown in Fig. 2.10, when a plane wave is incident up on those interfaces obliquely with a parallel polarization, the received power from the second interface, denoted by P_{r2}, can be derived as the following procedures. The reflection coefficient term of equation (2.38) needs to be replaced with the aid of equation (2.26):

$$\Gamma^2 = \left(\Gamma_{21}\right)^2 \left(T_{10}\right)^2 \left(T_{01}\right)^2 \exp\left(-\frac{4\boldsymbol{a}_1 d_1}{\cos \boldsymbol{f}_{t10}}\right) \qquad 2.40$$

Then the distance term of equation (2.38) needs to be modified using the trigonometric as

$$(2R)^2 = \left(\frac{2R}{\cos \boldsymbol{f}_{i1}} + \frac{2x_1}{\cos \boldsymbol{f}_{t10}}\right)^2 \qquad 2.41$$

where ϕ_{i1} and ϕ_{t10} are the incident and transmitted angles at the first interface, respectively. Note that the thickness of the dielectric layer, d_1, should be replaced with $x_1 = d_1\sqrt{\boldsymbol{e}_{r1}}$ as the wave velocity is reduced in the dielectric layer. Therefore, from equation (2.38), the received power from the second interface is expressed by

$$P_{r2} = \frac{P_t G^2 \boldsymbol{l}^2}{(4\boldsymbol{p})^2 \left(\dfrac{2R}{\cos \boldsymbol{f}_{i1}} + \dfrac{2x_1}{\cos \boldsymbol{f}_{t10}}\right)^2 L} \left(\Gamma_{21}\right)^2 \left(T_{10}\right)^2 \left(T_{01}\right)^2 \exp\left(-\frac{4\boldsymbol{a}_1 d_1}{\cos \boldsymbol{f}_{t10}}\right) \qquad 2.42$$

where $G_t = G_r = G$ for a monostatic system.

Then, the generalized radar equation from equation (2.42) can be defined as

$$P_{rn} = \frac{P_t G^2 \boldsymbol{l}^2 (\Gamma_{nn-1})^2 \left[\prod_{m=1}^{n-1} (\mathrm{T}_{mm-1})^2 (\mathrm{T}_{m-1m})^2 \exp\left(\frac{-4\boldsymbol{a}_m d_m}{\cos \boldsymbol{f}_{tmm-1}}\right) \right]}{(4\boldsymbol{p})^2 L \left(\frac{2R}{\cos \boldsymbol{f}_{i1}} + \sum_{l=1}^{n-1} \frac{2x_l}{\cos \boldsymbol{f}_{tll-1}} \right)^2}$$ 2.43

where P_{rn} is the returned power at the receiver antenna from the nth infinite plate.

The nth interface is detectable if $P_{rn} \geq S_i$. Consequently, the radar range equation taking into account the radar's system performance factor SF is found by using equations (2.36), (2.37) and (2.43):

$$SF = \frac{64\boldsymbol{p}^2 \left(\frac{R}{\cos \boldsymbol{f}_{i1}} + \sum_{l=1}^{n-1} \frac{x_l}{\cos \boldsymbol{f}_{tll-1}} \right)^2 L}{G^2 \boldsymbol{l}^2 (\Gamma_{nn-1})^2 \left[\prod_{m=1}^{n-1} (\mathrm{T}_{mm-1})^2 (\mathrm{T}_{m-1m})^2 \exp\left(-\frac{4\boldsymbol{a}_m d_m}{\cos \boldsymbol{f}_{tmm-1}}\right) \right]}$$ 2.44

This equation can be used to estimate the maximum penetration depth of radar sensors investigating multi-layered half-spaces, such as pavement layers.

2.4.3 Radar Equation for Buried Objects

To estimate the maximum detectable range for a buried object under the ground, as shown in Figure 2.11, equation (2.44) needs a modification that replaces the 2nd interface into the RCS of the buried object. The time-averaged power density S at the object is

$$S = \frac{P_t G_t}{4\boldsymbol{p}\left(\dfrac{R}{\cos \boldsymbol{f}_{i1}} + \dfrac{x_1}{\cos \boldsymbol{f}_{t10}}\right)^2} (\mathrm{T}_{10})^2 \exp\left(-\frac{2\boldsymbol{a}_1 d_1}{\cos \boldsymbol{f}_{t10}}\right) \qquad 2.45$$

Thus, the reflected power from the object is

$$P_r = \frac{P_t G_t A_{er}\boldsymbol{s}}{(4\boldsymbol{p})^2\left(\dfrac{R}{\cos \boldsymbol{f}_{i1}} + \dfrac{x_1}{\cos \boldsymbol{f}_{t10}}\right)^4 L} (\mathrm{T}_{10})^2 (\mathrm{T}_{01})^2 \exp\left(-\frac{4\boldsymbol{a}_1 d_1}{\cos \boldsymbol{f}_{t10}}\right) \qquad 2.46$$

where the system loss L is added later as discussed earlier.

Consequently, the maximum detectable range, d_{1max}, under the surface can be derived using the system performance factor SF:

$$SF = \frac{64\boldsymbol{p}^3\left(\dfrac{R}{\cos \boldsymbol{f}_{i1}} + \dfrac{x_{1max}}{\cos \boldsymbol{f}_{t10}}\right)^4 L}{G^2 \boldsymbol{l}^2 \boldsymbol{s}\, (\mathrm{T}_{10})^2 (\mathrm{T}_{01})^2 \exp\left(-\dfrac{4\boldsymbol{a}_1 d_{1max}}{\cos \boldsymbol{f}_{t10}}\right)} \qquad 2.47$$

where $d_{1max} = z_{1max}\big/\sqrt{\boldsymbol{e}_{r1}}$.

This equation is verified by equation (2.46) when the RCS of a buried target, $\boldsymbol{s}$, is

replaced with the RCS of a half-space, which is $\boldsymbol{p}\left(\dfrac{R}{\cos \boldsymbol{f}_{i1}}+\dfrac{x_{1\max}}{\cos \boldsymbol{f}_{t10}}\right)^{2}\Gamma^{2}$, with the aid of

equation (2.39).
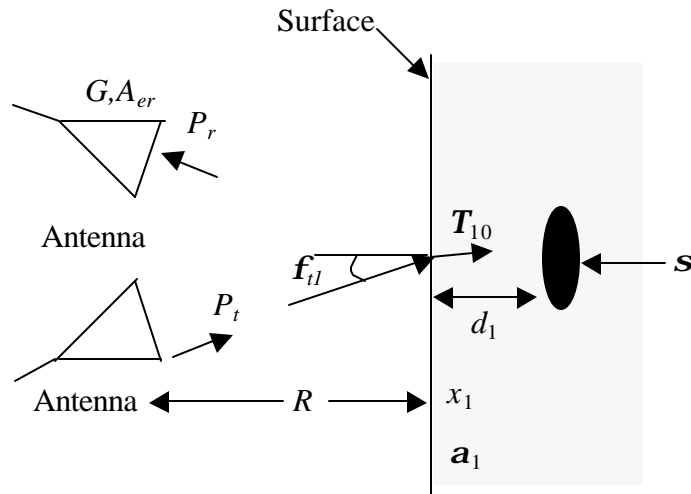
Figure 2.11 Buried object under the surface.

CHAPTER III

SFCW RADAR SENSOR ANALYSIS

3.1 Introduction

As discussed in Chapter I, SFCW radar sensor as a HRR sensor is attractive due to their distinct advantages. Understanding this sensor's principles is necessary not only to design, but also to analysis of its properties.

The resolution of a radar sensor can be either vertical or lateral, depending on the direction of observation. The vertical (or range) resolution depends upon the total absolute bandwidth of the transmitted signals and wave velocity. On the other hand, the lateral resolution is directly proportional to the 3dB beamwidth of the antenna and the distance between the antenna and the target. Therefore, the wider the bandwidth, the greater the observed vertical resolution, whereas the higher the frequency of operation, the narrower the lateral resolution.

Increasing the frequency of the transmitted signal makes it much easier to achieve accurate lateral and vertical resolution; however, it also has the added disadvantage of degrading the penetration depth. Usually, lower frequencies can penetrate deeper, but they provide very small lateral and vertical resolution, due in part to the restrictions on the absolute bandwidth. Therefore, there is an inherent tradeoff involved in satisfying both the penetration depth and resolution requirements.

This evidently implies that the design parameters of a SFCW radar sensor should be considered carefully and understood thoroughly in order to achieve an optimum design. These parameters include the frequency step Δf, the total bandwidth B, and the pulse repetition interval PRI. The frequency step is related to an ambiguous range R_u which is an unfolded range that can be defined by the sampling theory, while the absolute bandwidth of the transmitted signal determines the vertical resolution and the pulse repetition interval affects the receiver's sensitivity.

Further, the actual system performance factors are used by the radar equation derived in Chapter II. Consequently, simulations will be conducted to estimate the penetration depth in terms of the actual system performance factor for the two SFCW radar sensor systems. The simulation results for the UWB SFCW radar sensor system will show the maximum penetration depth of the asphalt and the base layers of the pavement, and also depict the effect of an incident angle. On the other hand, the simulation results for the millimeter-wave SFCW radar sensor system represent the maximum detectable depth of a buried object under the ground.

3.2 Principles of SFCW Radar Sensors

The SFCW radar sensor employs a consecutive train of N frequencies (i.e., f_0, f_1,...,

f_{N-1}) generated with a uniform frequency step Δf, as shown in Figure 3.1(a-c), that depicts its

waveform in time and frequency domains, and time vs. frequency domains.
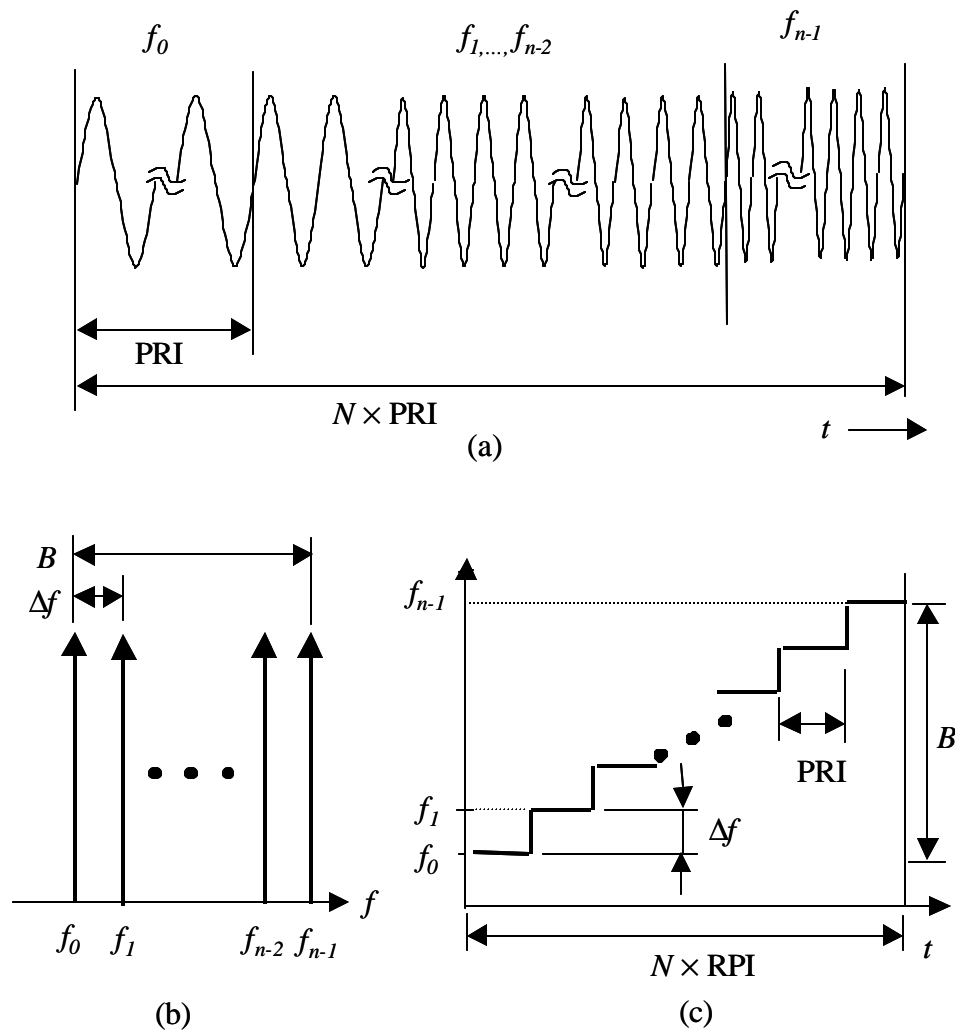
Figure 3.1 The waveform of a SFCW radar sensor in (a) time domain (b) frequency domain

(c) time vs. frequency domain.

The total bandwidth *B* is, thus *N* times Δf. An important parameter that needs to be considered is the pulse repetition interval *PRI* that is defined as the time required for transmitting a single frequency [18].

The step-frequency radar sensor operates as a frequency-modulation system - transmitting sequences of sinusoidal signals toward a target and processing the return signals in order to find the properties of that target. The mathematical expressions of the transmitted waveform of the SFCW radar sensor can be expressed as [18]

$$x_i(\boldsymbol{w}_i, t) = A_i \cos[\boldsymbol{w}_i t + \boldsymbol{q}_i]$$
<div align="right">3.1</div>

where $\boldsymbol{w}_i = 2\boldsymbol{p}(f_0 + i\Delta f)$, $i = 0,\ldots,N\text{-}1$; A_i and $\boldsymbol{q}_i$ are the amplitude and the relative phase of the ith transmitted signal. If the transmitted signals are returned back to the receiver from a fixed point target, the returned signals, including a two-way travel time τ, can be represented as

$$r_i(\boldsymbol{w}_i, t, \boldsymbol{t}) = B_i \cos[\boldsymbol{w}_i(t - \boldsymbol{t}) + \boldsymbol{q}_i]$$
<div align="right">3.2</div>

where B_i is the amplitude of the ith returned signal and $\boldsymbol{t}$ is the two-way travel time to the target. However, the two-way travel time $\boldsymbol{t}$, that is directly related to the range *R* of the target is

$$R = \frac{c\boldsymbol{t}}{2}$$
<div align="right">3.3</div>

where *c* is the speed of light in free space.

The returned signals are then coherently down-converted into base-band signals by a portion of the transmitted signals at the quadrature detector. After down-conversion, the normalized base-band in-phase (I) and quadrature (Q) signals are obtained as

$$I_i = \cos(-\boldsymbol{w}_i \boldsymbol{t}) = \cos \boldsymbol{f}_i \qquad\qquad 3.4a$$

$$Q_i(\boldsymbol{w}_i, \boldsymbol{t}) = \sin(-\boldsymbol{w}_i \boldsymbol{t}) = \sin \boldsymbol{f}_i \qquad\qquad 3.4b$$

The analog I/Q signals are sampled into digital I/Q signals through an Analog to Digital (A/D) converter. It is worthwhile to note that the range information of the target can be found from the phase $\boldsymbol{f}_i = \boldsymbol{w}_i \boldsymbol{t}$ of the I/Q signal. In order to retrieve the two-way travel time $\boldsymbol{t}$, the Fourier Transform is used. By combining the digitized I/Q signals in complex vector form, an analytic signal is obtained as

$$C_i = I_i + jQ_i = \exp(-j\boldsymbol{f}_i) \qquad\qquad 3.5$$

The IDFT that transforms the complex vector C_i in a frequency domain into a range profile of the target in time domain is [18],[38]

$$y_n = \frac{1}{M} \sum_{i=0}^{M-1} C_i \exp\left[\frac{j2\boldsymbol{p}ni}{M}\right] \qquad\qquad 3.6$$

where $0 \leq n \leq M\text{-}1$.

However, adding *M-N* zeros on the *N* complex vectors corresponding to the *N* stepped-frequencies to make the size of an array, *V*, including the *M* vectors into the power of two increases the speed of the Inverse Discrete Fourier Transform (IDFT), as well as a range accuracy as discussed later. Therefore, the IDFT applied to the array *V* becomes

$$y_n = \frac{1}{M} \sum_{k=0}^{M-1} V \exp\left[\frac{j2\boldsymbol{p}nk}{M}\right] \qquad\qquad 3.7$$

where $0 \leq n \leq M\text{-}1$ and k is the index of the vector *V*. Substituting equation (3.5) into (3.7) gives

$$y_n = \frac{1}{M} \sum_{k=0}^{M-1} \exp\left[j\left(\frac{2\boldsymbol{p}nk}{M} - \boldsymbol{j}_k\right)\right] \qquad\qquad 3.8$$

where

$$\boldsymbol{j}_k = \boldsymbol{f}_{\left(k-\frac{M-N}{2}\right)} \qquad\qquad 3.9$$

Equation (3.9) states that $\boldsymbol{j}_k$ is valid only if $(M\text{-}N)/2 \leq k \leq (M+N)/2 - 1$, otherwise $\boldsymbol{j}_k = 0$.

Letting $k = m + (M\text{-}N)/2$ leads equation (3.8) to

$$y_n = \frac{1}{M} \sum_{m=0}^{N-1} \exp\left[j\left(\frac{2\boldsymbol{p}n}{M}\left(m + \frac{M-N}{2}\right) - \boldsymbol{f}_m\right)\right] \qquad\qquad 3.10$$

Rewriting and normalizing equation (3.10) in terms of the range *R*, we have

$$y_n = \sum_{m=0}^{N-1} \exp\left[j\left(\frac{2\boldsymbol{p}n}{M}\left(m + \frac{M-N}{2} \right) - \frac{2\boldsymbol{p}f_m 2R}{c} \right) \right]$$

3.11

In addition, rearranging it gives

$$y_n = \exp\left(j\frac{4\boldsymbol{p}f_0 R}{c} \right)\exp\left(j\frac{\boldsymbol{p}n(M-N)}{M} \right)\sum_{m=0}^{N-1} \exp\left[j\left(\frac{2\boldsymbol{p}n}{M} - \frac{2\boldsymbol{p}\Delta f\,2R}{c} \right)m \right]$$

3.12

where $f_m = f_0 + m\Delta f$, f_0 is the start frequency. Then, solving equation (3.12) gives

$$y_n = \exp\left(j\frac{4\boldsymbol{p}f_0 R}{c} \right)\exp\left(j\frac{\boldsymbol{p}n(M-N)}{M} \right)\exp\left[j\frac{a(N-1)}{2} \right]\frac{\sin\left(\dfrac{aN}{2} \right)}{\sin\left(\dfrac{a}{2} \right)}$$

3.13

where $a = \left(n - \dfrac{2M\Delta fR}{c} \right)\dfrac{2\boldsymbol{p}}{M}$. Therefore, the magnitude response of the IDFT becomes

$$\left| y_n \right| = \left| \frac{\sin\left(\dfrac{aN}{2} \right)}{\sin\left(\dfrac{a}{2} \right)} \right|$$

3.14

where N is the number of frequency steps.

Figure 3.2 indicates the magnitude response of the IDFT (called the synthetic pulse) where that pulse, consisting of N lobes, is repeated every M cells due to M points of IDFT [38]. The peaks of the main lobes of equation (3.14) occur when $n = n_p + lM$ corresponds to $a = \pm 2l\boldsymbol{p}$, $l = 0, 1, 2…$ Hence, the range of the target in terms of n_p, which is the cell number corresponding to the main lobe's peak at $a = 0$, becomes

$$R = \frac{n_p c}{2M\Delta f} \qquad\qquad 3.15$$

where M is the number of IDFT.
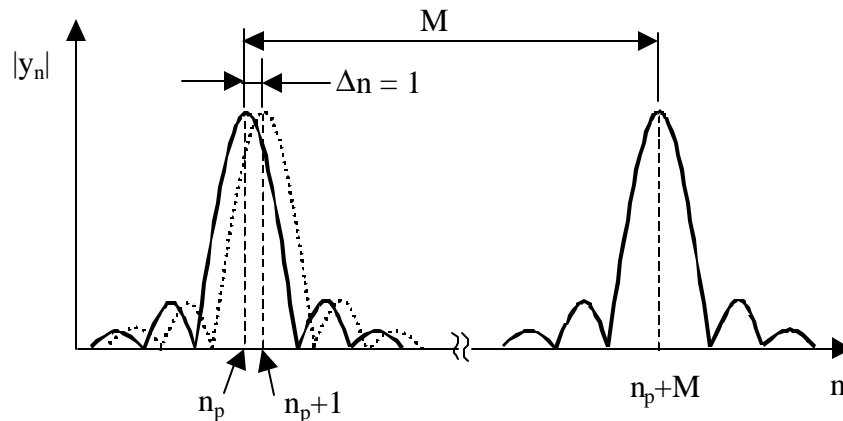
Figure 3.2 Synthetic pulse obtained by the IDFT.

Let the "range accuracy" dR be the minimum displacement of the peak of the main lobe, as shown in Figure 3.1. Then, the range accuracy obtained by letting $n_p = 1$ is

$$dR = \frac{c}{2M\Delta f} \qquad\qquad 3.16$$

It is important to note that equations (3.15) and (3.16) are valid with no error if the frequency source is ideal and the frequency step size Df is uniform. In practice, the frequencies are, however, contaminated by phase noise and the frequency step is not uniform. Therefore, the range accuracy wouldn't be improved beyond limitation. An analysis

of these effects on range accuracy was not covered here, as it will be beyond the scope of this dissertation.

In the case of multiple targets, the synthetic pulses obtained from each target will be superimposed. When two synthetic pulses caused by two targets at $R1$ and $R2$ have the same magnitudes, the range resolution ΔR can be defined by the range difference $R2$ - $R1$, where the cell number n_{p2} corresponding to the main-lobe's peak of the target at $R2$ coincides with the main lobe's null of the target at $R1$, as illustrated in Figure 3.3.

The main lobe's null occurs when $n = n_{p1} + M/N$, resulting in $n_{p2} = n_{p1} + M/N$. Consequently, the range resolution ΔR is given by

$$\Delta R = R2 - R1 = \frac{\left(n_{p1} + \dfrac{M}{N}\right)c}{2M\Delta f} - \frac{n_{p1}c}{2M\Delta f} = \frac{c}{2N\Delta f} \qquad 3.17$$

where the result is identical to the range resolution, defined for the impulse radar as $N\Delta f = B$.
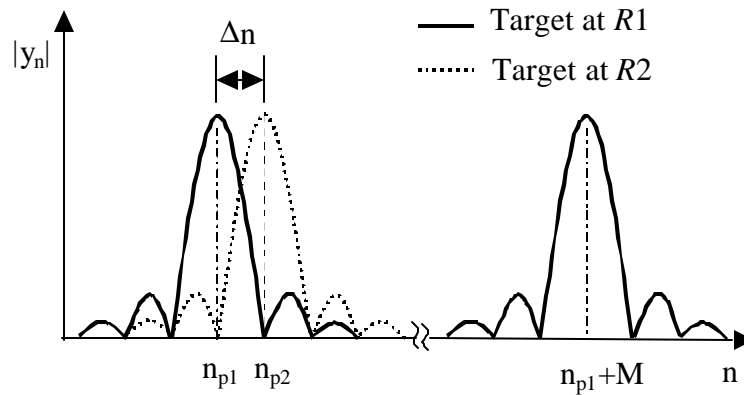
Figure 3.3 Range resolution as defined by the main lobe's null.

3.3 Design Parameters of SFCW Radar Sensor

Repeating equation (3.5) here as equation (3.18), the complex vector of the *I/Q* components is expressed as

$$C_i(\boldsymbol{w}_i, \boldsymbol{t}) = I_i(\boldsymbol{w}_i, \boldsymbol{t}) + jQ_i(\boldsymbol{w}_i, \boldsymbol{t}) = A_i \exp(-j\boldsymbol{f}_i) \qquad 3.18$$

where C_i is denoted by the complex *I*/Q vectors. When the SFCW radar sensor receives a train of stepped-frequency is from a stationary point target at range R, the phase ($\boldsymbol{f}_i$) of the complex *I*/Q vectors is given by equation (3.19):

$$\boldsymbol{f}_i = -2\boldsymbol{p}f_i t_1 = -\frac{4\boldsymbol{p}f_i R}{c} \qquad 3.19$$

where f_i is the ith frequency and $t_1=2R/c$ is the two-way travel time. The change of the phase $\boldsymbol{f}_i$ of the complex *I*/Q vectors, with respect to time, produces a constant radial frequency ω (rad/sec), as given by

$$\boldsymbol{w} = -\frac{\partial \boldsymbol{f}_i}{\partial t} = -\frac{4\boldsymbol{p}R}{c}\frac{df_i}{dt} = -\frac{4\boldsymbol{p}R\Delta f}{c(PRI)} \qquad 3.20$$

If a target range *R* is fixed, the the complex *I*/Q vectors in a magnitude of A_i rotate at a constant rate along the locus, as sown in Figure 3.4, where the phase $\boldsymbol{f}_i$ is a function of the stepped-frequency f_i, as seen in equation (3.20), and A_i is assumed as a constant value.

The above analysis can be generalized to a situation involving two targets at R_1 and R_2, wherein the magnitude and phase of the complex vectors are A_i and $\boldsymbol{f}_i$ for the target at R_1 and B_i, and $\boldsymbol{f}_i$ for the target at R_2, while the radial frequency $\boldsymbol{w}$ of the complex *I*/Q vectors is

the sum of the different radial frequencies ($\boldsymbol{w}_{R1}$ and $\boldsymbol{w}_{R2}$) of the complex I/Q vectors produced by the two targets, and is expressed by
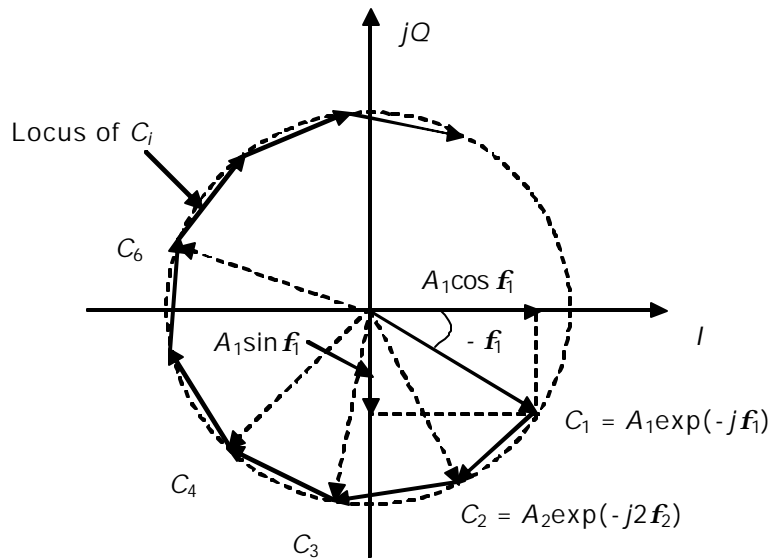
Figure 3.4 Complex I/Q vectors rotating at a constant rate for a fixed point target when the amplitudes A_i of returned signals are constant.

$$\boldsymbol{w} = \boldsymbol{w}_{R1} + \boldsymbol{w}_{R2} = -K(R_1 + R_2)$$ 3.21

where $K = -4\pi\Delta f\,/\,[c(PRI)]$ is constant if the targets are in the same propagating medium. The vector diagram resulting from the two targets is depicted in Figure 3.5.
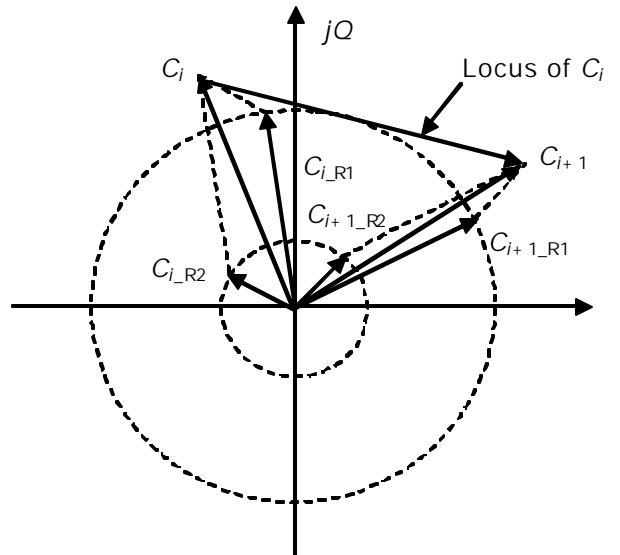
Figure 3.5 Complex vectors $C_i = C_{i\_R1} + C_{i\_R2}$ moving along the locus due to two point targets.

3.3.1 Lateral and Vertical Resolution

Lateral/Vertical resolution denotes the ability of the sensor to distinguish two targets (or objects) that are closely spaced in lateral and vertical directions, respectively. A resolution could either vertical or lateral, depending upon the direction of observation, as shown in Figure 3.6.
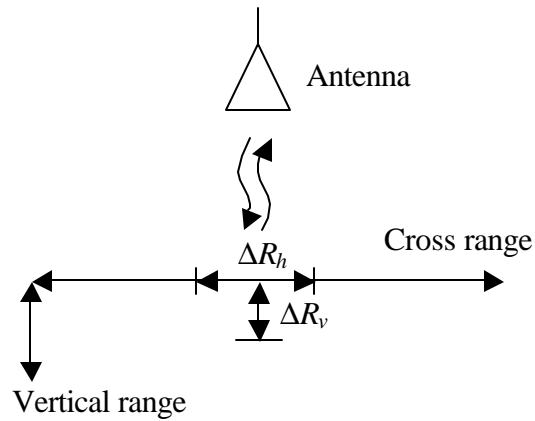
Figure 3.6 Resolution of a radar sensor, where ΔR_h and ΔR_v denote the lateral and vertical resolution, respectively.

In figure 3.7(a), the lateral resolution is defined by [35]

$$\Delta R_h = R\boldsymbol{q} \qquad\qquad 3.22$$

where $\boldsymbol{q}$ is the antenna beamwidth (in radians) and R is the range of a target satisfying a far field condition, as given by [36]

$$R \geq \frac{2D^2}{\boldsymbol{l}} \qquad\qquad 3.23$$

where $\boldsymbol{l}$ is the wavelength and D is the dimension of the antenna.

The lateral resolution ΔR_h is thus dependent of the antenna beamwidth and the range of a target in far field distance, which means that the high frequencies yield a high (or narrow) lateral resolution if no advanced signal processing (such as the Synthetic Aperture image processing technique) is applied.

Figure 3.8(a) represents the lateral resolution vs. the far field distance with varied beamwidths. According to the simulation results, it is needed to employ the frequency range of the Ka-band to achieve the lateral resolution in inches for the surface profiling sensor. The 3dB beamwidth of the Ka-band waveguide horn antenna that is to be incorporated into the system is about 0.26 radians. If the range of a target is 0.12m, the lateral resolution will be 0.031m (= 1.2 inches).

On the other hand, the vertical resolution ΔR_v is determined by the total operating bandwidth B given by equation (1.2). However, the total bandwidth B is equal to $N \times \Delta f$ that gives the vertical resolution of the SFCW radar sensor as [18]

$$\Delta R_n = \frac{c}{2N\Delta f} \qquad\qquad 3.24$$

Figure 3.8(b) represents the vertical resolution vs. the bandwidth with varied relative dielectric constants when a hamming window factor (= 1.33) is applied. According to the simulation results, the required bandwidth should be at least 4GHz to achieve the vertical resolution in inches for the subsurface radar sensor. However, with the theoretical range resolution, it is quite hard to distinguish two synthetic pulses clearly, especially if those pulses are superimposed. Hence, it was decided that the operating absolute bandwidths should be 5GHz and 8GHz for the microwave and millimeter-wave SFCW radar sensors, respectively.
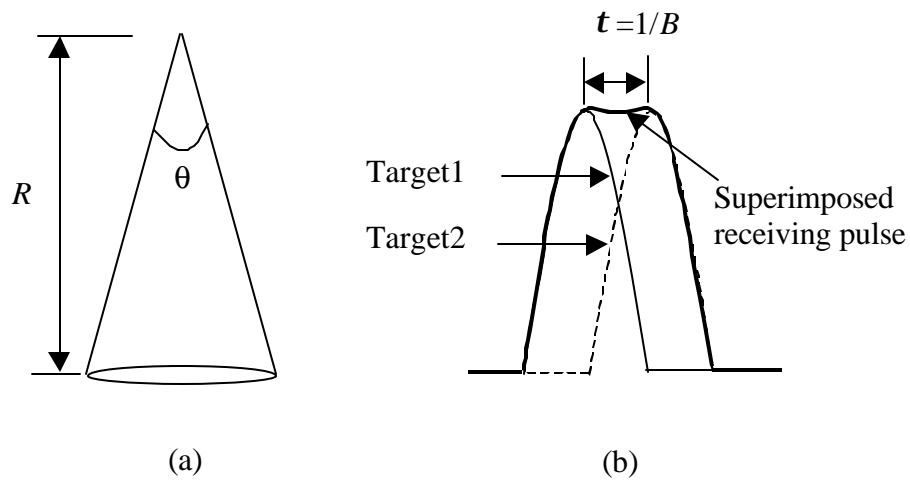
Figure 3.7 (a) Lateral resolution (b) vertical resolution.
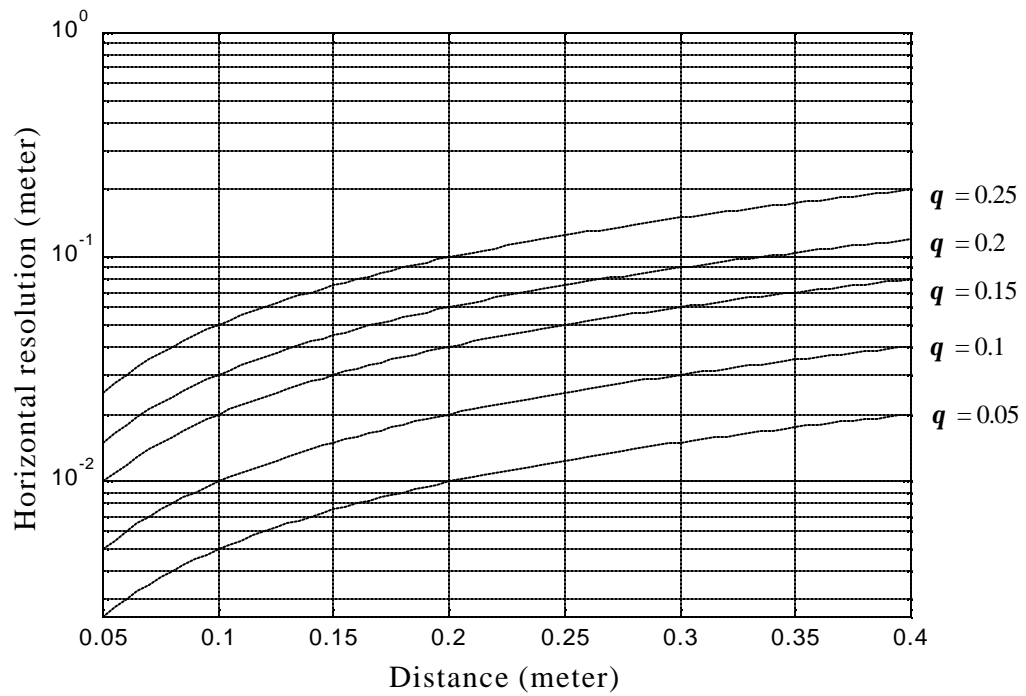
Figure 3.8 (a) Lateral resolution vs. distance R where θ is in radians.
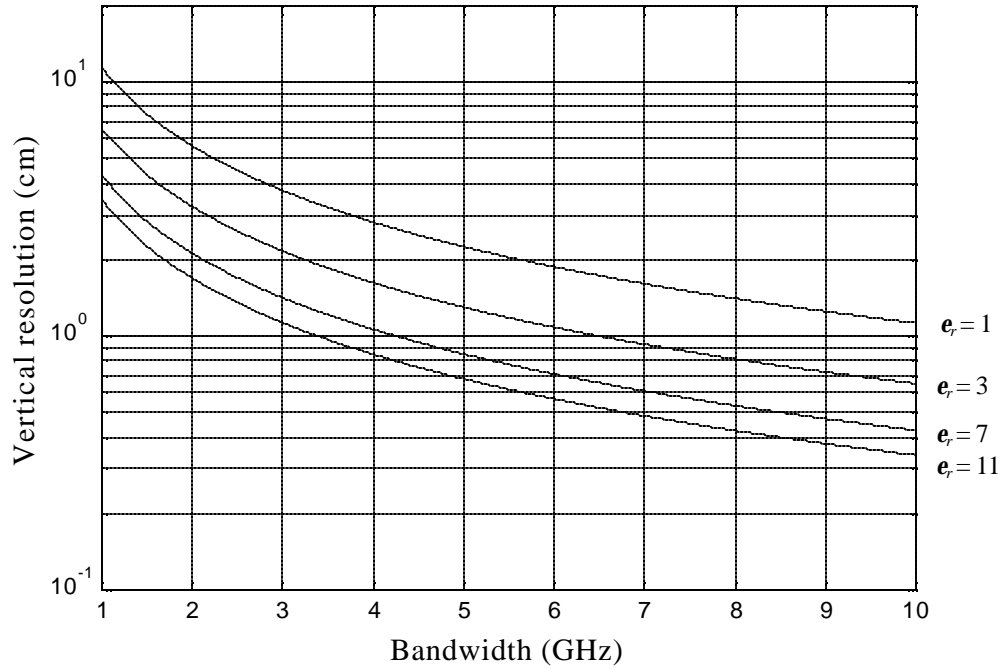
Figure 3.8 (b) Vertical resolution vs. bandwidth $N\boldsymbol{D}f$.

3.3.2 Ambiguous Range

As seen from equation (3.20), the phase $\boldsymbol{f}_i$ of the complex I/Q vectors is determined by the frequency f_i. The resulting phases $\boldsymbol{f}_i$ of the complex I/Q vectors are in the range of 2π. When two targets located at R_1 and R_2 produce phases $\boldsymbol{f}_{i\_R1}$ and $\boldsymbol{f}_{i\_R2}$, respectively, at a frequency of f_i and if the phase difference ($\boldsymbol{Df}_{R1}$ and $\boldsymbol{Df}_{R2}$) obtained from the two consecutive frequencies $\boldsymbol{Df}_{R1} = \boldsymbol{f}_{i\_R1} - \boldsymbol{f}_{i+1\_R1}$ and $\boldsymbol{Df}_{R2} = \boldsymbol{f}_{i\_R2} - \boldsymbol{f}_{i+1\_R2}$ are equal, then the two targets tend to appear at the same location.

From another perspective, as in equation (3.20), the phase differences $\boldsymbol{Df}_{R1}$ and $\boldsymbol{Df}_{R2}$ associated with R_1 and R_2 respectively, is given by

$$\Delta f_{R1} = -\frac{4pR_1\Delta f}{c} \qquad\qquad 3.25a$$

$$\Delta f_{R2} = -\frac{4pR_2\Delta f}{c} \qquad\qquad 3.25b$$

If $Df_{R1} = Df_{R2} \pm 2pn$, then the two targets are ambiguous. From equations (3.25a-b), the ambiguous range R_u is found as [18]

$$R_u = |R_1 - R_2| = \frac{c}{2\Delta f} \qquad\qquad 3.26$$

As seen by equation (3.26), the ambiguous range is determined by the frequency step Δf.

The ambiguous range can also be found by using the sampling theory [38]. If a signal with bandwidth B is sampled by a sampling time Δt, the signal is replicated every $n(1/\Delta t)$Hz in a frequency domain where n is the integer, as shown in Figures 3.9(a-b). In order to avoid aliasing, the bandwidth B must be less than one-half the inverse of the sampling time (i.e., B £ $1/2Dt$). Similarly, using a duality of the sampling theory enables us to infer that the range R must be less than one-half of an inverse of the frequency step times the speed of light (i.e., R £ $c/2Df$) as shown in Figures 3.9(c-d). Thus, the resulting ambiguous range R_u is the same, as given by equation (3.26).
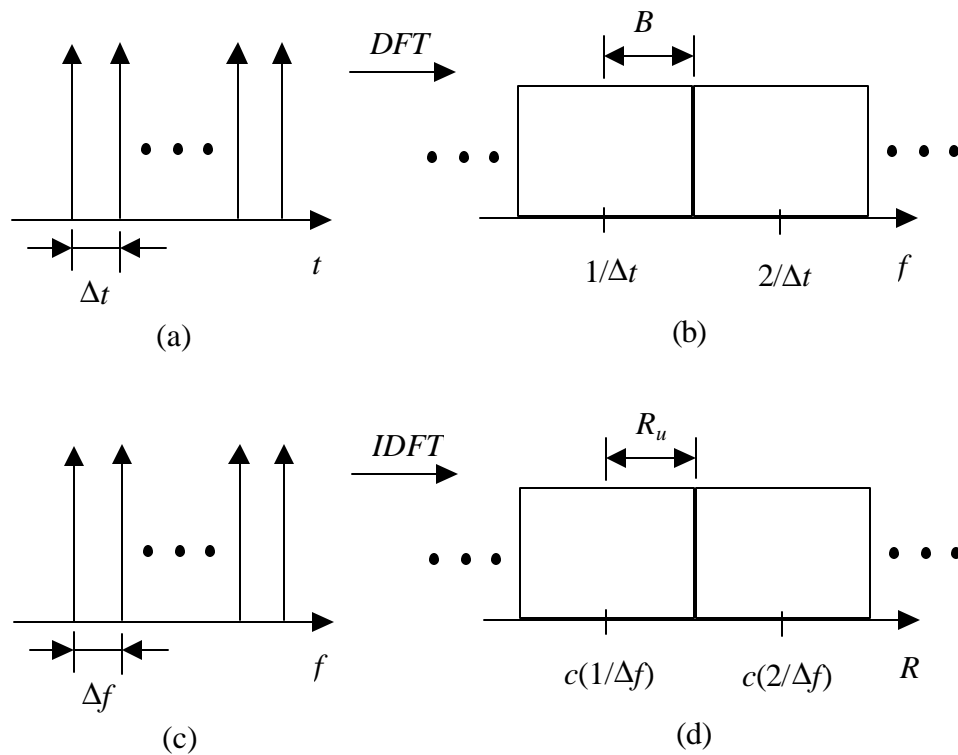
Figure 3.9 Nyquist sampling to avoid aliasing: (a) time domain samples; (b) frequency domain of (a) through the DFT; (c) SFCW signals in the frequency domain; (d) the range domain of (c) through the IDFT.

Figure 3.10 illustrates the ambiguous ranges vs. the frequency steps with various dielectric constants. According to the simulation results, the narrower the frequency step, the greater the ambiguous range, which inclines us to consider a frequency step of 10MHz, in spite of having an added disadvantage of requiring a large sweep time to cover the entire bandwidth. The rationale for this choice is further buttressed by the fact that the frequency synthesizer available in the testing lab doesn't allow for the generation of arbitrary frequency steps in the vicinity of 10 MHz.
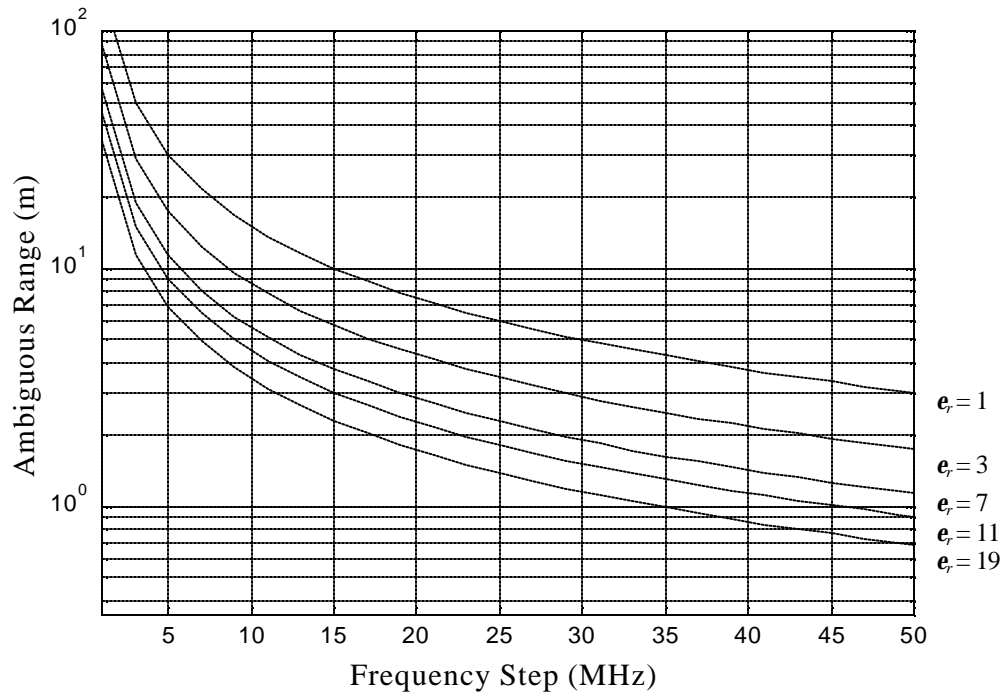
Figure 3.10 Ambiguous range vs. frequency step of the SFCW radar sensor for different dielectric constants.

For the microwave and millimeter-wave SFCW radar sensor, the frequency step of 10MHz was used. Though other frequency steps (1, 100 MHz) were realizable in the lab, they had significant limitations. The 1MHz frequency step was deemed too narrow to sweep the total operating bandwidth, while the 100MHz step was so wide that the ambiguous range was only 1.5m.

3.3.3 Pulse Repetition Interval

The SFCW radar sensor needs an entire train of stepped frequency signals for a process to find the range information of a given target. The SFCW radar sensor transmits a single frequency and receives the reflected signal frequency during a particular *PRI*. However, for coherent demodulation, the PRI should be at least larger than the two-way travel time to the target. Therefore, the *PRI* for a single stepped-frequency must be larger than the two-way travel time to the furthest target at *R*, which can be estimated as

$$PRI \geq \frac{2R}{c}$$
3.27

However, as the *PRI* should be considered up to the ambiguous range, it can be inferred from equations (3.26-27) that the *PRI* term related to the frequency step is given by [18]

$$PRI \geq \frac{1}{\Delta f}$$
3.28

From equation (3.28), the minimum required *PRI* should be greater than 0.1us if the frequency step is set to 10MHz. Thus, if a *PRI* of 50us is used with a frequency step of 10MHz, at a bandwidth of 5GHz, the sweep-time of the entire bandwidth would be 25ms.

However, the fastest *PRI* of the frequency synthesizer in the laboratory is 100ms. This *PRI* leads to a 50sec sweep-time for a frequency step of 10MHz, when a bandwidth of

5GHz is chosen. On account of this constraint, it was possible to conduct only stationary measurements.

3.3.4 Number of Frequency Steps

The SFCW radar sensor illuminates a target with a consecutive train of N frequencies, receives the train of N frequencies, and coherently processes them in a signal processing block in order to extract the synthetic pulse. Therefore, its process gain is said to be N if there is no integration loss. Generally, the effective integration number N_{eff} is given by [35]

$$N_{eff} = \frac{N}{L_i}$$

3.29

where N is the number of frequency steps and L_i is the integration loss.

Integration loss is caused by a window function, an imperfection in the coherent process, and so on. The hamming window yields an integration gain (= $1/L_i$) of 0.54 [35]. For subsurface SFCW radar sensors, a complete coherent process is achieved when the dispersion effect of the propagation media is compensated for by signal processing with known properties. Therefore, the radar equations (2.41) and (2.44) derived in Chapter II, need to be modified for the SFCW radar sensor, as given by

$$SF = \frac{64 p^2 \left(\frac{R}{\cos f_{i1}} + \sum_{l=1}^{n-1} \frac{x_l}{\cos f_{tll-1}} \right)^2 L}{G^2 I^2 N_{eff} (\Gamma_{nn-1})^2 \left[\prod_{m=1}^{n-1} (T_{mm-1})^4 \exp\left(-\frac{4 a_m d_m}{\cos f_{tmm-1}} \right) \right]}$$

3.30

and

$$SF = \frac{64\boldsymbol{p}^{3}\left(\dfrac{R}{\cos\boldsymbol{f}_{i1}} + \dfrac{x_{1\max}}{\cos\boldsymbol{f}_{t10}}\right)^{4} L}{G^{2}\boldsymbol{l}^{2}N_{\mathit{eff}}\boldsymbol{s}\left(\mathrm{T}_{10}\right)^{4}\exp\left(-\dfrac{4\boldsymbol{a}_{1}d_{1\max}}{\cos\boldsymbol{f}_{t10}}\right)} \qquad 3.31$$

Consequently, equations (3.30) and (3.31) can be used for detecting pavement layers and buried object under the ground, respectively.

3.4 The System Performance Factor and Penetration Depth

The system performance factor SF, as seen from equations (3.30) and (3.31), is one of the most important parameters in the radar equation for estimating the penetration depth of the subsurface radar sensor. In practical subsurface radar sensor systems, the system performance factor can be limited by the actual receiver dynamic range, as discussed below. Hence, it was necessary to incorporate a correction into the system performance factor

The maximum available dynamic range, denoted by DR_{ma}, of the receiver of a sensor is the ratio of the maximum available receiving power, denoted by P_{r_ma}, that the receiver can tolerate without suffering a distortion to the receiver's sensitivity, S_i, which satisfies a specified SNR at the output of the receiver. The upper limit of the maximum available compression free dynamic range is determined by the 1dB compression point P_{1dB} of the receiver amplifier in order to avoid its saturation, while the lower limit is determined by the receiver's sensitivity. For safety considerations in practical systems, the maximum available receiver power needs to be below the 1dB compression point of the receiver amplifier.

The maximum available receiving power of a sensor's receiver is occurred when the sensor system is directed on a metal plate during a calibration process. If the transmission loss L_t is considered to be the difference between the transmitted and the received power when their corresponding antennae are directed on the metal plate placed at the stand-off distance, R, as illustrated in Figure 3.11, it is found that the maximum available transmitting power P_{t_ma} can be estimated from the maximum available receiving power, as follows.

$$P_{t\_ma} = P_{r\_ma} + L_t \leq (P_{1dB} + L_t)(dB)$$

3.32

It should be noted that the above analysis is valid only if the maximum receiving power is less than the saturating power of the receiver.

The transmission loss L_t (= S_{21} in Figure 3.11) is caused by the spreading loss, the antenna's mismatch and efficiency, and others practical losses arising from connectors and cables. The transmission loss can be calculated using EM simulations, or measured using the Network Analyzer if antennae are available, as shown in Figure 3.11.

The instantaneous bandwidth of the SFCW radar sensor is equal to the inverse of the *PRI*, as the frequency band of a single frequency f during time τ is equal to $1/\tau$ around the center frequency f [38]. Thus, the instantaneous bandwidth of the input signal at the receiver is much less than the total bandwidth B, which results in a low sensitivity level at the receiver, as defined by equation (2.35).

A low noise amplifier (LNA) should be placed at the front-end, followed by a down-converter to reduce the total noise figure as given by [39]:
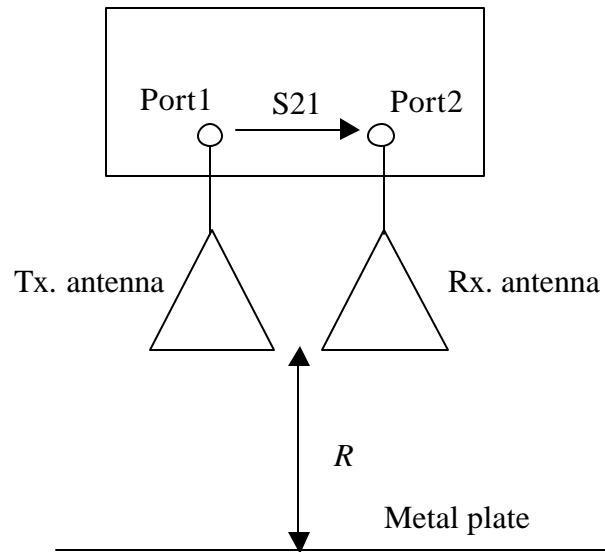
Figure 3.11 Measurement of the transmission loss L_t where R is the stand-off distance.

$$F = F_1 + \frac{F_2 - 1}{G_1} + ... + \frac{F_n - 1}{G_1 G_2 ... G_{n-1}}$$ 3.33

As a result, if the SNR_o is set, the sensitivity of the receiver is given by [39]

$$S_i = kTBF(SNR)_o$$ 3.34

where $kT = -174dBm$/Hz at $T = 290$ K.

Figure 3.12 illustrates the system performance factors and dynamic ranges of the sensor system. A procedure to calculate the actual system performance factor, which is modified from the system performance factor, is described as below.

The system performance factor can be found by using equations (2.41), (2.44) and (3.32):

$$SF = \left(P_{t\_ma} - S_i\right) = (P_{r\_ma} + L_t - S_i)(dB) \qquad 3.35$$
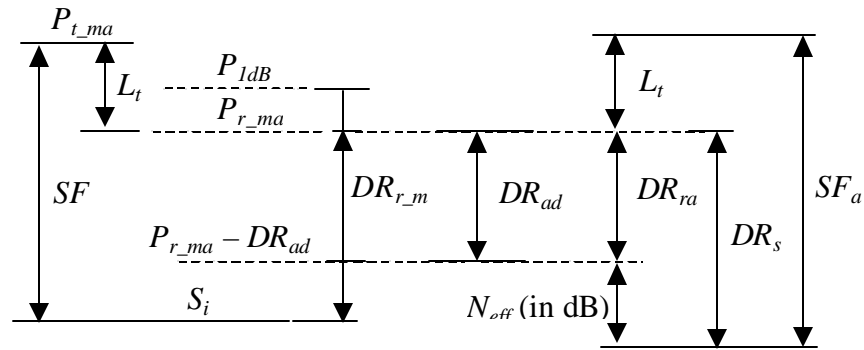
Figure 3.12 Graphical analysis of the system performance factors and the dynamic ranges when $DR_{ad} \leq DR_{r\_ma}$.

On the other hand, the receiver's maximum available dynamic range, denoted by DR_{r_ma}, can be defined as the difference between the maximum available receiving power and the receiver's sensitivity:

$$DR_{r\_ma} = \left(P_{r\_ma} - S_i\right)(dB) \qquad 3.36$$

This leads the system performance factor (in terms of the maximum available dynamic range) to be

$$SF = (DR_{r\_ma} + L_t)(dB) \qquad 3.37$$

The system performance factor represents the maximum performance of the system if the system satisfies the maximum available dynamic range. However, it is important to note that the system incorporates A/D converters for signal processing. Therefore, the A/D converter's dynamic range, denoted by DR_{ad}, should be considered in the system with its dynamic range given by [38]

$$DR_{ad} \approx 6.N\,(dB)$$

<div align="right">3.38</div>

where N is the number of bits of A/D converter.

Therefore, the receiver's available dynamic range, denoted by DR_{ra}, is limited by either the receiver's maximum available dynamic range or the A/D converter's dynamic range, whichever is narrower. However, a signal processing gain increases the receiver's dynamic range; therefore, the system dynamic range, denoted by DR_s, can be defined as

$$DR_s = \left\lfloor DR_{ra} + 10\log\left(N_{eff}\right)\right\rfloor(dB)$$

<div align="right">3.39</div>

As a result, the actual system performance factor, denoted by SF_a, is given by:

$$SF_a = \left(DR_s + L_t\right)(dB)$$

<div align="right">3.40</div>

Now, the penetration depth of the SFCW radar sensor system can be estimated using the radar equation incorporating the actual system performance factor obtained by equation (3.40).

3.4.1 Estimation of Penetration Depth of the Asphalt and Base Layers

The maximum penetration depths of the asphalt and base layers of the pavement, as shown in Figure 3.13, were simulated at 3GHz for the SFCW radar sensor. In addition, the effect of the incident angle was also simulated for the same sensor.

The parameters used for simulation are listed in Table 3.1 where the system loss L was set to 19dB, which includes the antenna efficiency (= 6dB per a resistive loaded antenna, i.e. 12dB for a pair of antennas), the antenna mismatch (= 1dB per antennas, i.e. 2 dB for a pair of antennas), and the other losses (= 5dB cables, connectors, etc.) [31]. The process gain was 24dB, while the hamming window function and 500 frequency steps were used on the signal processing without the integration loss. The A/D converters in the data acquisition (DAQ) board of LabView have a resolution of 12 bits per sample, which leads to a dynamic range of 72dB. The measured transmission loss was 25dB after incorporating the antennas (which will be discussed later in Chapter IV). Therefore, the actual system performance factor was estimated to be 121dB by using equation (3.39).

Figure 3.14 illustrates the maximum penetration depth (or maximum detectable thickness) of asphalt layers vs. the actual system performance factor with different attenuation constants. The results show that the attenuation constant and the actual system performance factor significantly affect the penetration depth. According to the simulation results, this sensor system based on the actual system performance factor of 121dB, can detect the thickness of the asphalt layer in the range of 2.3-9.5m, depending upon the attenuation constants.

The simulation results shown in Figure 3.15 represent the maximum penetration depth (or maximum detectable thickness) of an asphalt layer vs. the actual system performance factor with an incident angle of 20 degrees, where the attenuation constant of the asphalt layer was fixed at 0.3 (Np/m). The results show that the incident angle of 20 degrees does not significantly affect the maximum detectable range.

Figure 3.16 shows the simulation results for the maximum penetration depth (or maximum detectable thickness) of the base layer vs. the actual system performance factor with different attenuation constants, where the thickness of the asphalt layer was fixed to 3 inches.
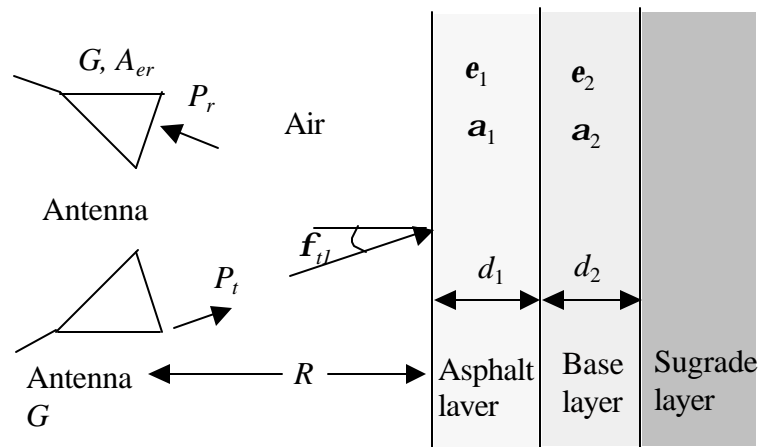
Figure 3.13 Pavement layers used for estimating penetration depths in the simulation.

In addition, this sensor system can detect the thickness of the base layer in the range of 0.2-0.4m, depending upon the attenuation constants, when the thickness of the asphalt layer is fixed to 3 inches.

Table 3.1 Parameters used in the simulation for estimating the penetration depth of the pavement.

Electrical properties of pavement layers at 3GHz		
Asphalt layer	$e\dot{c}_{r1}$	5-7
	$e^2{}_{r1}$	0.03-0.05
	a	0.05-0.5(Np/m)
Base layer	$e\dot{c}_{r1}$	8-12
	$e^2{}_{r1}$	0.3-0.8
	a	3-9(Np/m)
Subgrade layer	$e\dot{c}_{r3}$	20
Radar sensor parameters		
Antenna gain	G	10dB
Wave length at 3GHz	l	0.1m
System loss	L	19dB
Process gain	G_p	24dB
Incident angle	f_{t1}	20 degrees
Stand off distance	R	0.2m
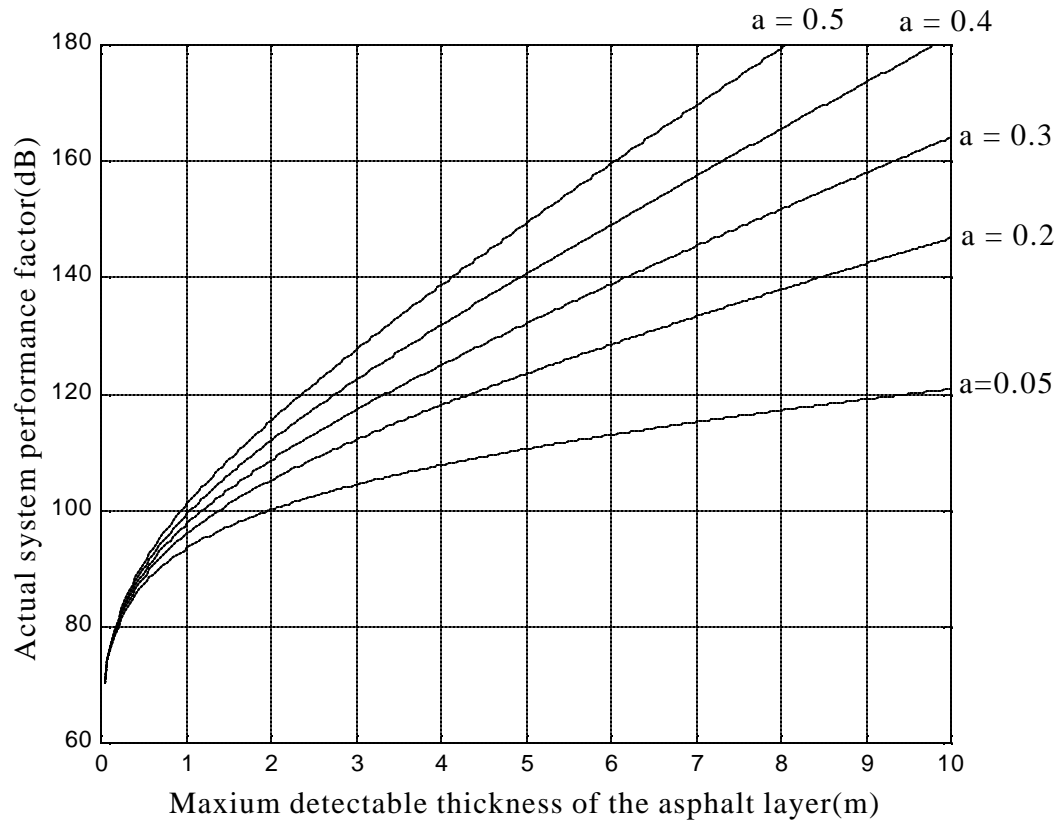
Figure 3.14 Maximum penetration depth (or maximum detectable thickness) of the asphalt

layer vs. the actual system performance factor with different attenuation constants where ″a″

denotes the attenuation constant (Np/m).
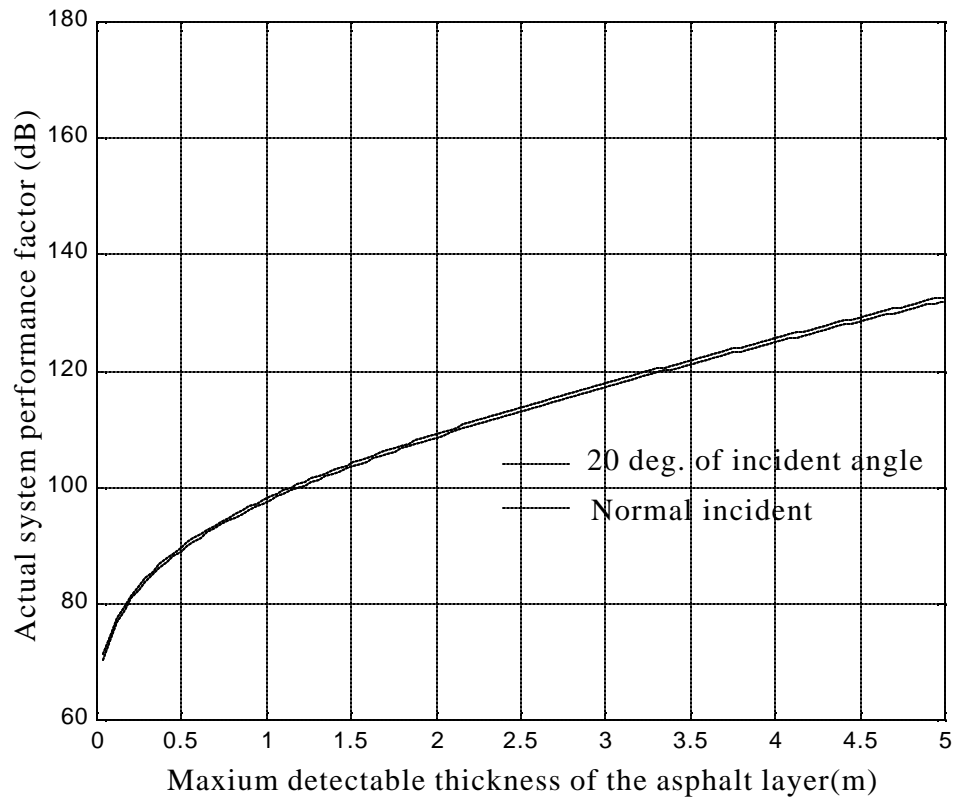
Figure 3.15 Maximum penetration depth (or maximum detectable thickness) of the asphalt layer vs. the actual system performance factor with different incident angles where the attenuation constant of the asphalt layer is 0.3 (Np/m).
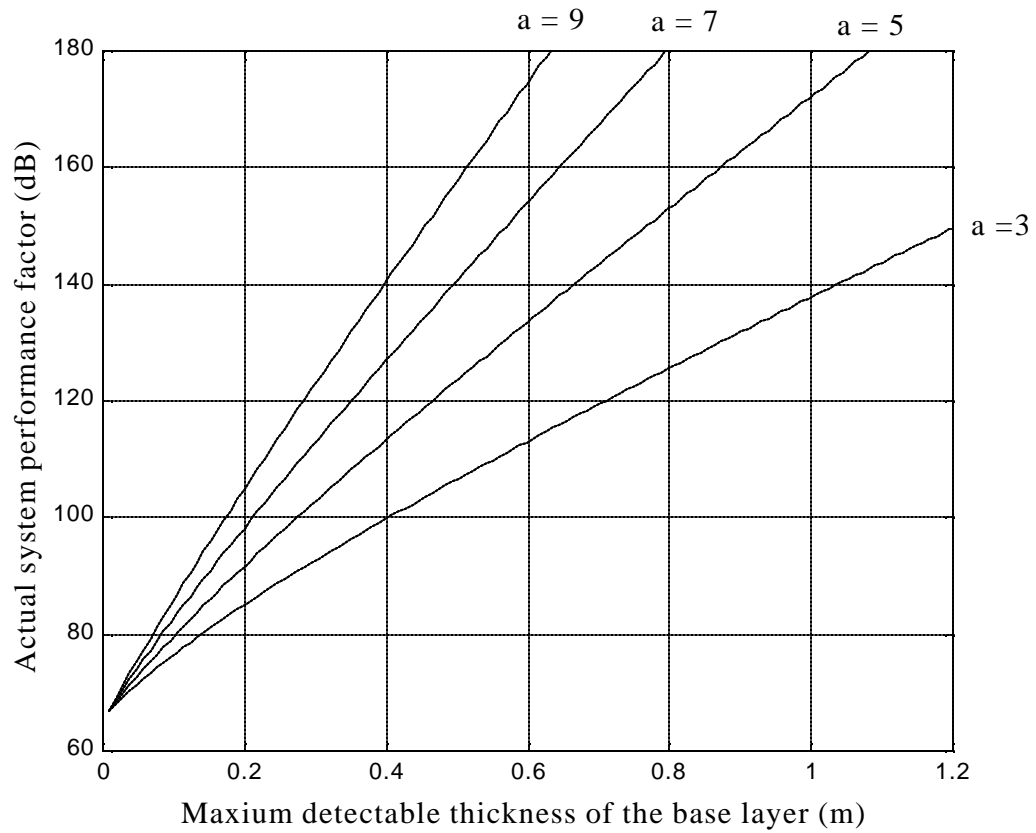
Figure 3.16 Maximum penetration depth (or maximum detectable thickness) of the base layer vs. the actual system performance factor with different attenuation constants where "a" denotes the attenuation constant (Np/m) and the thickness of the asphalt layer is 3 inches.

3.4.2 Estimation of Penetration Depth for Buried Mines

The maximum penetration depth of a buried metal target under sand, as shown in Figure 3.17, was simulated for the millimeter-wave SFCW radar sensor where the attenuation constants of the dry sand used were in the range of 3-70 (Np/m). As the accurate values of the attenuation constants of the dry sand at the Ka-band were not available, it was necessary to estimate the attenuation constants of the dry sand from those values at 1GHz (0.1-2.3) and 100 MHz (0.01-0.23), as mentioned in [31]. The parameters used for the simulation are listed in Table 3.2, where the system loss was set to 17dB, which includes the antenna efficiency at 4dB and the antenna mismatch at 2dB [31], and connectors, cables, adapter, and circulator losses at 9dB. The process gain was 23dB, while the hamming window function and 400 frequency steps were applied to the signal processing without the integration loss. The measured transmission loss was 13dB when a waveguide horn antenna was used. Therefore, the actual system performance factor was estimated to be 108dB where the A/D converter's dynamic range was 72dB.

Figure 3.18 shows the maximum detectable depth vs. the actual system performance factor to detect a spherical object (radius = 0.025m) buried under the sand with different attenuation constants. The results show that the millimeter-wave SFCW radar sensor system can detect the buried spherical target in the range of 0.05-0.5m, depending upon the attenuation constants of the sand used.
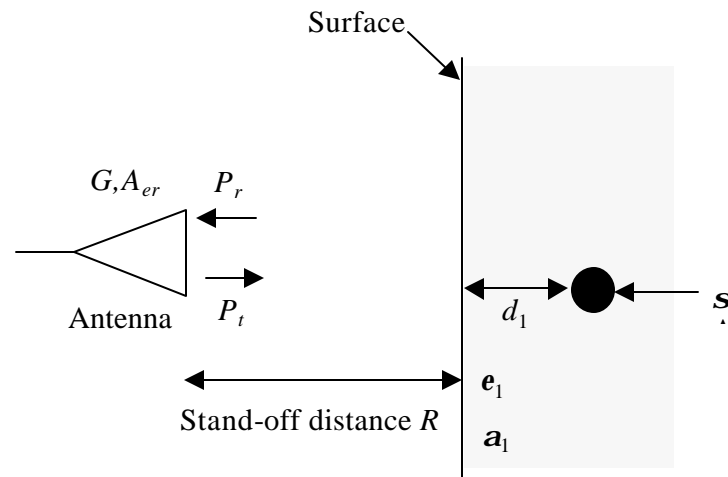
Figure 3.17 Buried target used for estimating the penetration depth in the simulation.

Table 3.2 Parameters used for estimating the detection of a buried object with the millimeter-wave SFCW radar sensor.

Electrical properties of the material used at 30GHz		
Dry sand	$e\text{¢}_{r1}$	3-6
	a	3-70
RCS of the target	s	0.0019m^2
Radar sensor parameters		
Antenna gain	G	24dB
Wave length	l	0.01m
System loss	L	17dB
Process gain	G_p	23dB
Stand off distance	R	0.1m
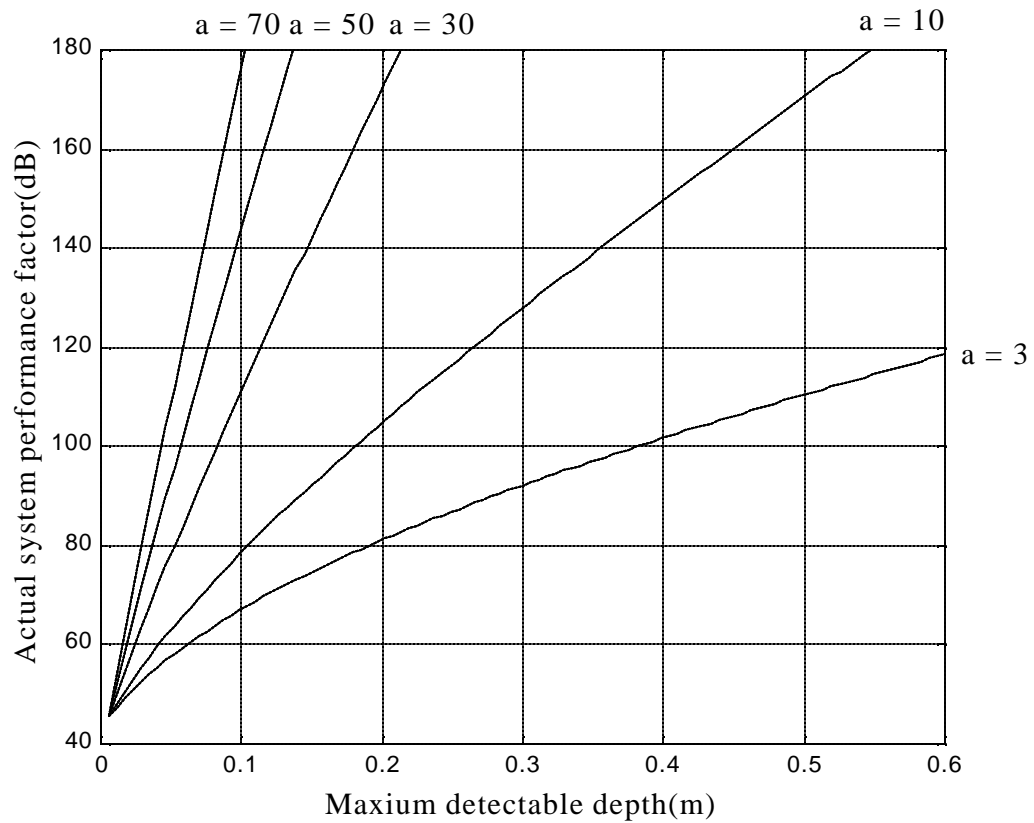
Figure 3.18 Maximum detectable depth vs. the actual system performance factor with different attenuation constants used to detect a spherical object (radius = 0.025m) buried under the ground (e_{r1} = 3) where "a" denotes the attenuation constant (Np/m) of the ground material.

CHAPTER IV

DEVELOPMENT OF SFCW RADAR SENSORS

4.1 Introduction

A stepped-frequency radar sensor system can be said to comprise of transceiver, antenna and signal processing parts. The transceiver architecture can be either a homodyne or super-heterodyne scheme. The super-heterodyne scheme is more complex, but enables easier correction of the I/Q errors, unlike the homodyne scheme; hence, it was chosen as the transceiver architecture of the stepped-frequency radar sensor systems. Therefore, two stepped-frequency radar sensor systems employing this coherent super-heterodyne architecture were developed. The first one, which essentially is a millimeter-wave stepped-frequency radar sensor, is used for surface and subsurface sensing, that specifically finds its applications in surface profiling, monitoring liquid level, and detecting and localizing mines. The other one, known as the microwave stepped-frequency radar sensor is used for investigating thickness of the asphalt or base layers. A receiver and transmitter based on these requirements, as discussed in the previous chapter, were designed accordingly. The transceiver of the millimeter-wave stepped-frequency radar sensor was integrated with MICs and MMICs on an FR-4 and alumina substrate, while that of the microwave stepped-frequency radar sensor was integrated with MICs on FR-4 substrates. This enabled the realization of low cost, light weight and small size transceivers.

Microstrip quasi-horn antennae that are suitable for integration with the transceivers were developed for both of the sensor systems. These types of antennae provide high gains comparable to waveguide horn antennae, however their E-plane radiation angles are slightly deviant from the boresight, due to the ground plane. Therefore, for the microwave stepped-frequency radar sensor system employing two antennae, an optimal alignment was determined with the aid of the measurement results using the Network Analyzer.

Signal processing was developed using LabView. The signal processing includes data acquisition, synchronization, and regeneration, as well as a new simple compensation technique for common amplitude and phase errors. In addition, a simple Fast Fourier Transform (FFT) that converts the frequency domain data to synthetic pulses in the time domain was performed.

4.2 Transceiver

The transceiver architecture of a typical stepped-frequency radar sensor can either be a homodyne or super-heterodyne. Figure 4.1(a–b) shows a block diagram of a stepped-frequency radar system based on the homodyne and the super-heterodyne architectures, respectively. The super-heterodyne system down-converts the input signal twice to get a base-band signal centered at DC.
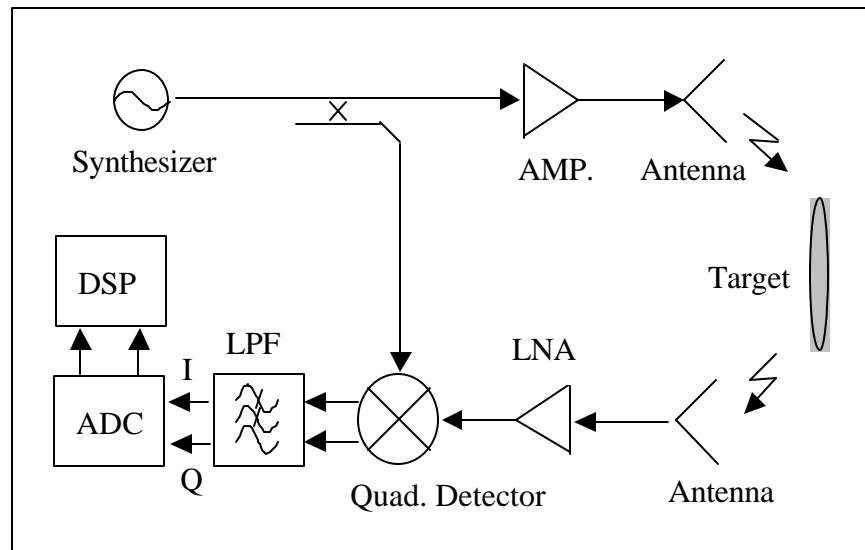
(a)
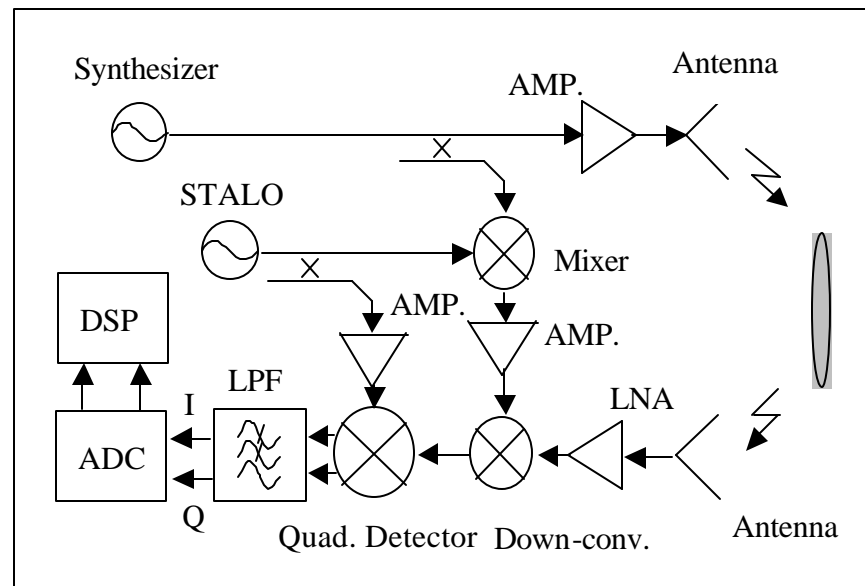
(b)

Figure 4.1 System block diagrams of a stepped-frequency radar sensor; (a) homodyne architecture (b) super-heterodyne architecture.

The inputs are first down-converted to an intermediate frequency (*IF*), which is the single center frequency of the down-converted band, then the *IF* is down converted into the base-band signal. For the super-heterodyne system, the quadrature detector is placed followed by the first down-converter. Alternately, the homodyne system, also called as a zero *IF* system, down-converts the input directly into the base-band in-phase (*I*) and quadrature (*Q*) components by using a quadrature detector. Thus, the homodyne system operating at a wide bandwidth requires a wideband quadrature detector, which leads to inconsistent *I/Q* imbalances over the band of interest as the responses of the 90 degree phase shifter are not constant in the wide-bandwidth. On the other hand, the heterodyne system can use a quadrature detector operating in a narrow band instead of a wide band. Therefore, *I/Q* imbalances are nearly constant as the responses of the 90 degree phase shifter are constant at the single *IF*. Consequently, despite the complexity, the super-heterodyne system is still very much preferred over the homodyne system.

4.2.1 Transceiver of the Millimeter-Wave SFCW Radar Sensor System

Figure 4.2 represents the system level block diagram of the newly developed millimeter-wave stepped-frequency radar sensor based on coherent super-heterodyne architecture.
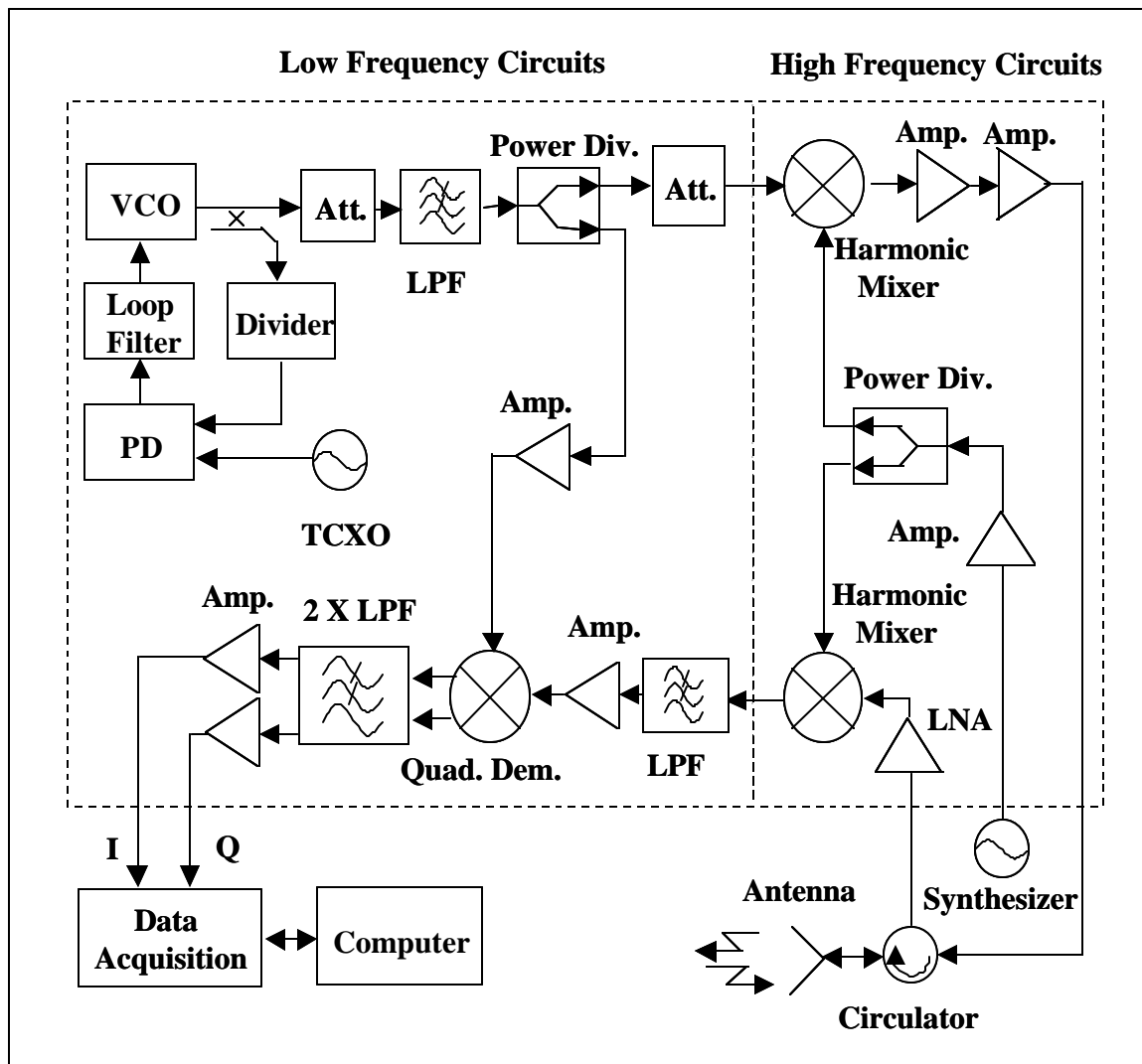
Figure 4.2 System level block diagram of the millimeter-wave stepped-frequency radar sensor.

A sensor employing a mono-static system, which transmits and receives signals through the same antenna, was configured with a transceiver, antenna and signal processing parts.

A sinusoidal signal of 1.72 GHz was generated by a phase-locked loop (PLL) oscillator consisting of a reference frequency of 6.71875 MHz, a 2^8- frequency divider and a 2-pole loop filter. The generated continuous wave is used as an intermediate frequency (IF) signal at the sub-harmonically pumped mixer in the transmitter path and as an LO signal at the quadrature demodulator in the receiver path. The sub-harmonically pumped mixer up-converts the IF signal, modulated with the incoming 14-17.99-GHz stepped frequencies that are increased by a frequency step of 10 MHz with an external synthesizer, to 29.72-37.7-GHz signals that are transmitted toward a target. The reflected signals from the target are down-converted to a single IF signal of 1.72 GHz by mixing with the 14-17.99-GHz stepped-frequencies by the sub-harmonically pumped mixer in the receiver path. The IF signal is then converted into base-band I and Q signals by the quadrature detector. These I and Q signals are digitized with ADCs in the DAQ board of LabView, and then processed to extract the target's information.

The transceiver has been completely realized using both discrete and integrated circuits - both MICs and MMICs. The circuits of the transceiver were clearly differentiated into high and low frequency circuits in order to reduce the cost of fabrication, as well as to facilitate their design as shown in Figure 4.1. The high frequency circuits were integrated on an alumina substrate that has a thickness of 10mil and a relative dielectric constant of 9.8

with a low loss. The high frequency circuits were composed of a Ku-band medium power amplifier (Agilent, HMMC-5618), Ka-band sub-harmonically pumped mixers (Hittite, HMC266), Ka-band low noise amplifiers (TRW ALH140C), transmission lines and a Ku-band power divider, and these were mounted and etched on an alumina substrate. The Ku-band medium power amplifier increases the external LO power generated from the synthesizer. The harmonic mixer up-converts the input at the IF port or down-converts the input at the RF port with the second harmonic of the frequency of the LO port. The LNAs amplify the transmitting and receiving signals and reduce the total noise figure of the receiver. These high frequency components were then bonded with 3-by-0.5mil gold ribbons by using a wedge-bonding machine (West bond, 7600C).

The low frequency circuits that operate below 1.72GHz were fabricated on an FR-4 PC board, that had a thickness of 31-mil and a relative dielectric constant of 4.3 with a loss of 0.15dB/in. at 1.72GHz. A PLL circuit, two attenuators, two low pass filters, a power divider, two amplifiers, a quadrature detector, and a two channel video amplifiers were mounted and etched on the FR-4 substrate. The PLL oscillator generates a stable single IF, and the attenuators adjust the LO and IF power below the specifications of the following circuits. LPFs reduce the high frequency harmonics included in the IF signal and the IF harmonics added in the base-band I/Q signals. The power divider splits the IF in two; one for the IF of the up-converter and the other for the LO of the qudrature detector. The LO amplifier increases the LO power to pump the quadrature detector; and the quadrature detector down-converts the single frequency input, which includes information on the targets,

into the base-band I/Q signals. The two channel video amplifier increases the power of the base-band I/Q signals to meet the input range of the A/D converter.

Table 4.1 represents the analysis of the receiver design. The transmission loss L_t (= 13dB) was measured with a waveguide horn antenna, as shown in Figure 3.11, to estimate the available transmitting and receiving power. The dominant parts were the LNA and down-converter, as the 1 dB compression points of the LNA and down-converter limit the maximum available receiving power. The maximum available receiving power must be set below -7dBm to avoid the down-converter and the LNA from saturating, thus, it was set to –8dBm with a 1 dB margin.

The total noise figure (F) of 5.7dB was estimated from equation (3.33), as the noise figure (F_1) of the LNA and that (F_2) of the down-converter are 4dB and 12dB, respectively. When the fastest PRI of 100ms, resulting in an instantaneous bandwidth of 10Hz, was used with the output SNR_o set to 14dB [35], the receiver sensitivity was calculated as –150.3dBm from equation (3.34).

Then, the input range of the A/D converter was determined according to the A/D converter specifications. The A/D converters in the DAQ board have 12bits of resolution per sample, which resulted in a dynamic range of 72dB, and the maximum input range was between $\pm$ 0.2V to $\pm$ 42V, which led to a sensitivity of 35uV at $\pm$ 0.2V of the maximum input. Thus, the maximum input was set to $\pm$ 2V, which led the input range of the ADC to be in the range of $\pm$ 2V (= 9dBm@1k) to $\pm$ 0.5mV (= -63dBm). The video amplifier was used for boosting the quadrature detector output to the ADC input range.

Table 4.1 Receiver design analysis where Pin_1dB is the input 1dB compression point, Pout is the output power, the maximum available receiving power P_{r_ma} is -8dBm, and 1dB for the insertion loss of FR-4 substrate was added.

	Gain(Vo/Vi)	Loss	Pin_1dB	Pout
LNA	11dB		4dBm	3dBm
Down-conv.		12dB	4dBm	-9dBm
LPF		0.5dB		-9.5dBm
Amplifier	13dB		1dBm	3.5dBm
I/Q mixer		8dB	4dBm	-4.5dBm
LPF(Ro=200)		6.2dB		-10.7dBm
Amp(Ro=1k)	27.7dB			10dBm
Substrate		1dB		9dBm
Total	51.7dB	27.7dB		
DR_{ra}		72dB	SF_a	108dB

From the maximum available receiving power of -8dBm, the maximum available transmitting power was set to be 5dBm from equation (3.32). The system performance factor *SF* was then calculated as 155.3dB (= 5dBm+150.3dBm) by using equation (3.35). Using the maximum available receiving power of –8dBm led the receiver's maximum available dynamic range to be 142.3dB (= -8dBm+150.3dBm) from equation (3.36). However, the ADC's dynamic range limits the receiver available dynamic range DR_{ra} to 72dB. Therefore, the actual system performance factor, denoted by SF_a, for the radar equation was calculated as 108dB (=95dB+13dB) from equation (3.40).

Similarly, Table 4.2 shows the analysis of the transmitter design. In order to reach the maximum available transmitting power level of 5dBm, a cascaded amplifier was used. Two attenuators were used to tune the power levels, one in between the PLL oscillator and the splitter output and the other in between the splitter output and the up-converter input.

Figure 4.3 shows a photograph of the integrated transceiver in the overall dimension of 4 x 6 inches, where the alumina and FR-4 substrates were mounted on an aluminum block, which supports two substrates on a strong ground plane and integrates them into one.

Table 4.2 Transmitter design analysis where 1dB for the insertion loss of FR-4 substrate was added.

	Gain	Loss	Pin_1dB	Pout
PLL osc.				5dBm
Attenuator		2dB		3dBm
LPF		0.5dB		2.5dBm
Splitter		3.5dB		1dBm
Attenuator		5dB		-4dBm
Up-converter		12dB	4dBm	-16dBm
Amplifier	11dB		4dBm	-5dBm
Amplifier	11dB		4dBm	6dBm
Substrate		1dB		7dBm
Total	22dB	24dB		
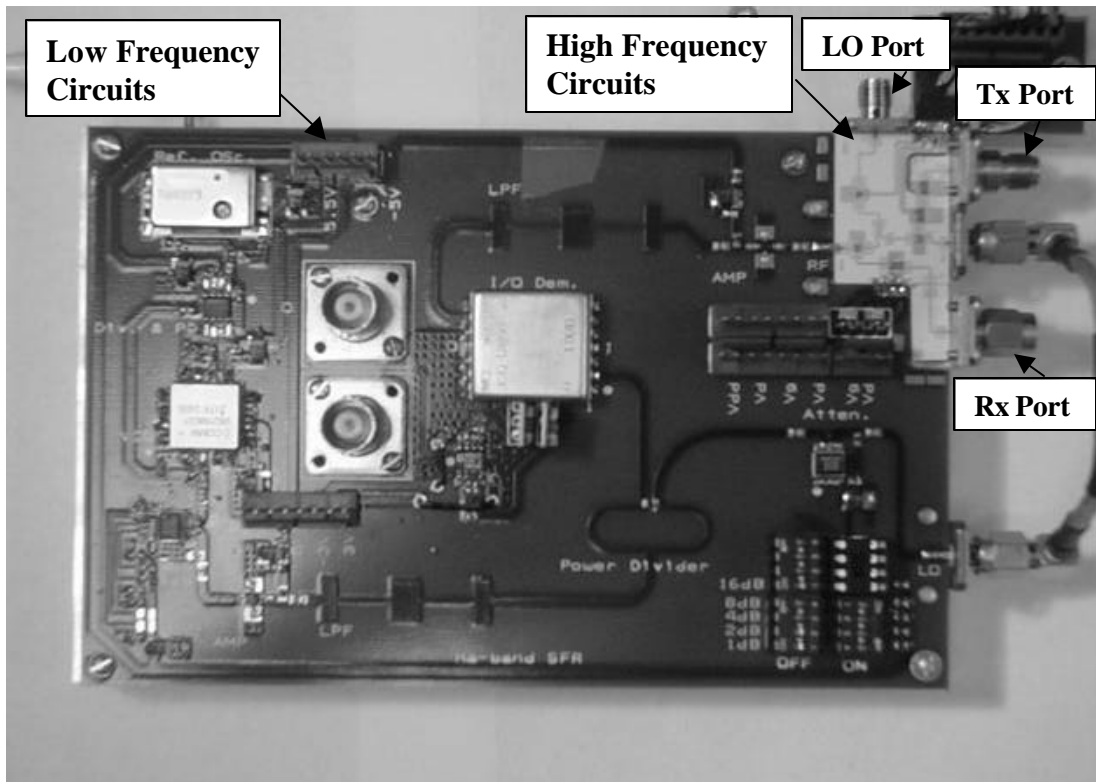
Figure 4.3 Photograph of millimeter-wave stepped-frequency radar transceiver.

4.2.2 Transceiver of the Microwave SFCW Radar Sensor System

　　　Figure 4.4 illustrates the system level block diagram of the newly developed 0.6-5.6-GHz microwave stepped-frequency radar sensor based on the coherent super-heterodyne architecture.
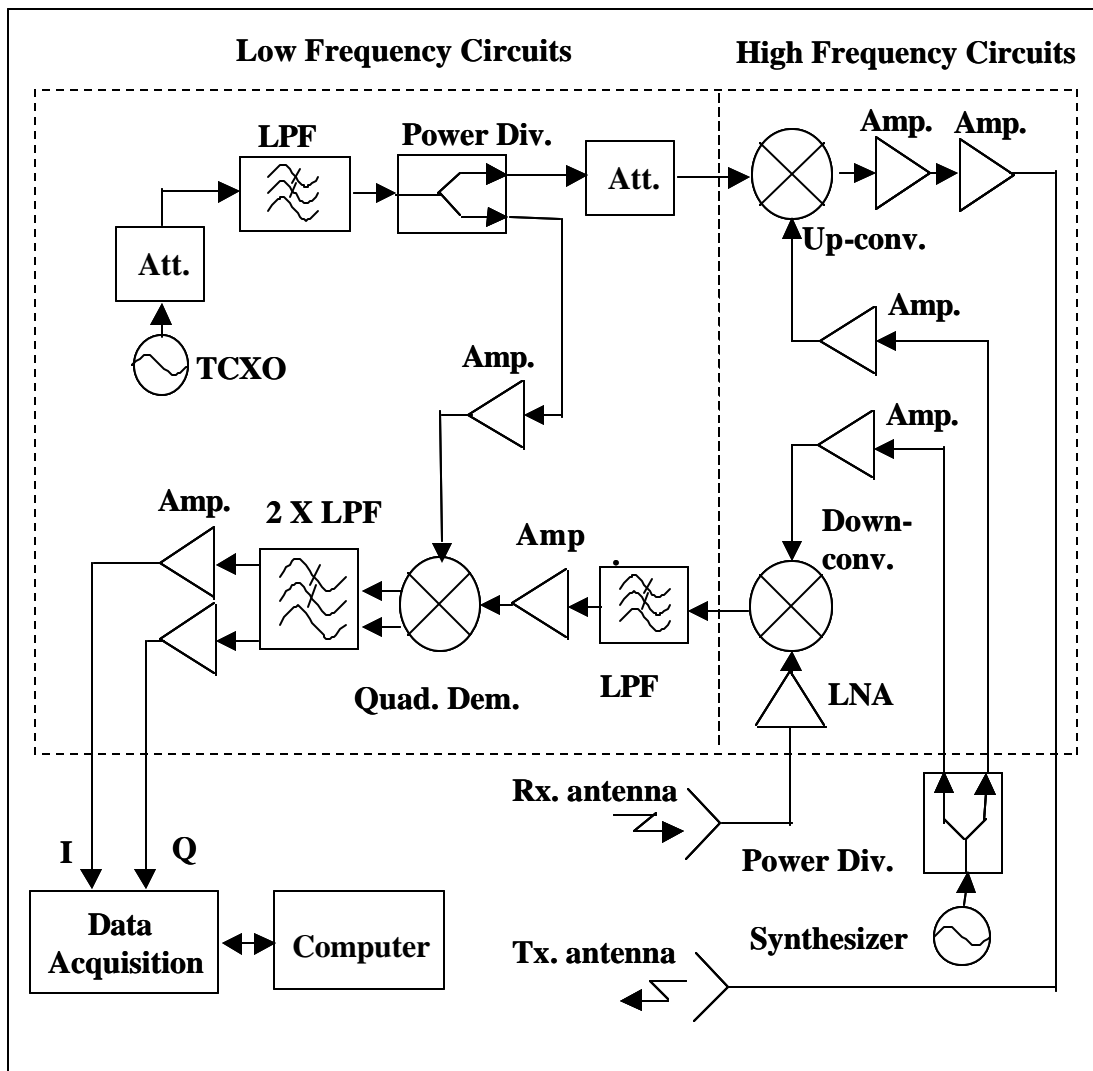
Figure 4.4 System level block diagram of the microwave stepped-frequency radar sensor.

The temperature compensated crystal oscillator (TCXO) in the transceiver generates a signal of 10 MHz, which is used as the LO signal for the quadrature detector and the IF signal for the up-converter. The up-converter converts the incoming 0.59-5.59-GHz LO signals from the synthesizer to 0.6-5.6-GHz signals that are meant to be transmitted toward the targets (through an UWB transmit antenna.) Alternately, the down-converter converts the returned signals from the targets (through the receiver antenna) to an IF signal of 10 MHz by mixing them with the coherent LO signals from the synthesizer. The IF signal is then converted into the base-band I/Q signal in the quadrature detector by mixing it with the coherent LO signal from the TCXO. The I/Q signals are finally digitized with ADCs and processed in digital signal processing blocks to extract the target information.

The transceiver, realized with integrated MICs, was separated into two parts for easy fabrication, evaluation, and trouble-shooting. One is for low-frequency circuits and the other is for high-frequency circuits. Both low and high-frequency circuits were fabricated on 31-mil FR-4 substrates. However, the loss of FR-4 (0.4dB/in. at 5GHz) is much higher than that of the common RT/Duroid substrates, which are widely used for microwave circuits, hence the substrate for the high frequency circuits was designed in a compact size of 2 x 4 inches.

The high-frequency circuits include an up-converter, a cascaded RF amplifier, two LO amplifiers, a low noise amplifier (LNA), and a down-converter. The up-converter modulates the IF signals into the RF signals with the aid of external LO signals. The cascaded amplifier increases the power of the transmitting RF signals, and the two LO amplifiers boost

the external LO up to the required power level for pumping the up-converter and down-converter, respectively. The LNA reduces the total noise figure (F) of the transceiver and increases the power of the received RF signals. The down-converter demodulates the received RF signals into a single frequency called the IF signal.

The low-frequency circuits consist of a stable local oscillator (STALO), attenuators, low pass filters (LPFs), a power divider, an IF amplifier, an LO amplifier, an I/Q detector, and a two channel video amplifier. A temperature controlled crystal oscillator (TCXO) was used for STALO. The attenuators limit the power of LO and IF signals below the specifications of the following circuits. LPFs reduce the high frequency harmonics included in the IF signal and IF harmonics added in the base-band I/Q signals. The power divider splits the output of TCXO into two, one for the IF of the up-converter and the other for the LO of the qudrature detector. The LO amplifier increases the LO power to pump the quadrature detector. The quadrature detector down-converts the single frequency input, which includes information on targets, into the base-band I/Q signals. The two channel video amplifier increases the power of the base-band I/Q signals to meet the input range of the ADC.

Table 4.3 shows the analysis of the transmitter design. The transmission loss L_t (= 25dB) was first measured with the developed antennae to estimate the available transmitting and receiving power. The maximum available transmitting power was set to 11dBm to avoid the transmitter amplifier from saturating. Two attenuators were used for adjusting the power levels, one in between the STALO output and the splitter output and the other in between the splitter output and the up-converter input.

Table 4.3 Transmitter analysis where 1dB for the insertion loss of FR-4 substrate was

added.

	Gain	Loss	Pin_1dB	Pout
STALO				5dBm
Attenuator		3dB		2dBm
LPF		0.3dB		1.7dBm
Spliter		3.2dB		-1.5dBm
Attenuator		2.5dB		-4dBm
Up-converter		8dB	5dBm	-12dBm
1st Amplifier	12dB		3dBm	0dBm
2nd amplifier	12dB		3dBm	12dBm
Substrate		1dB		11dBm

Table 4.4 shows the analysis of the receiver design. From the maximum available transmitting power, the maximum available receiving power was estimated to -14dBm from equation (3.32). The input range of the ADC was set to $\pm$ 2V (= 9dBm@1k), which is the same that was used for the millimeter-wave SFCW radar sensor system, and the video amplifier was used for increasing the quadrature detector output level to the ADC input range.

A total noise figure (F) of 6dB was estimated from equation (3.33), as the noise figure (F_1) of the LNA and that (F_2) of the down-converter are 5.5dB and 8dB, respectively. When the other conditions were the same as those for the millimeter-wave SFCW radar sensor system, the receiver sensitivity S_i was estimated to -148dBm from equation (3.34).

From a maximum transmitting power of 11dBm, the system performance factor SF was calculated as $159dB$ (= 11dBm+148dBm) by using equation (3.35). The receiver's maximum available dynamic range was 134dB (= -14dBm+148dB) from equation (3.36). From the ADC's dynamic range of 72dB, the actual system performance factor for the radar equation was calculated to 121dB (=96dB+25dB) from equation (3.40).

Table 4.4 Receiver analysis where the maximum available receiving power is -8dBm and where 1dB for the insertion loss of FR-4 substrate was added.

	Gain(Vo/Vi)	Loss	Pin_1dB	Pout
LNA	12dB		3dBm	-2dBm
Down-conv.		8dB	5dBm	-10dBm
LPF		0.3dB		-10.3dBm
Amplifier	13dB			2.7dBm
I/Q mixer		6dB	4dBm	-3.3dBm
LPF(Ro=200)		6.2dB	-	-9.8dBm
Amp.(Ro=1k)	26.8.dB		-	10dBm
Substrate		1dB		9dBm
DR_{ra}	72dB		SF_a	121dB

Figure 4.5 shows a photograph of the integrated transmitter with an overall dimension of 4 x 7 inches where the FR-4 substrates for low and high frequency circuits were mounted on an aluminum block to support the substrates on the strong ground plane and integrate them into one huge block.
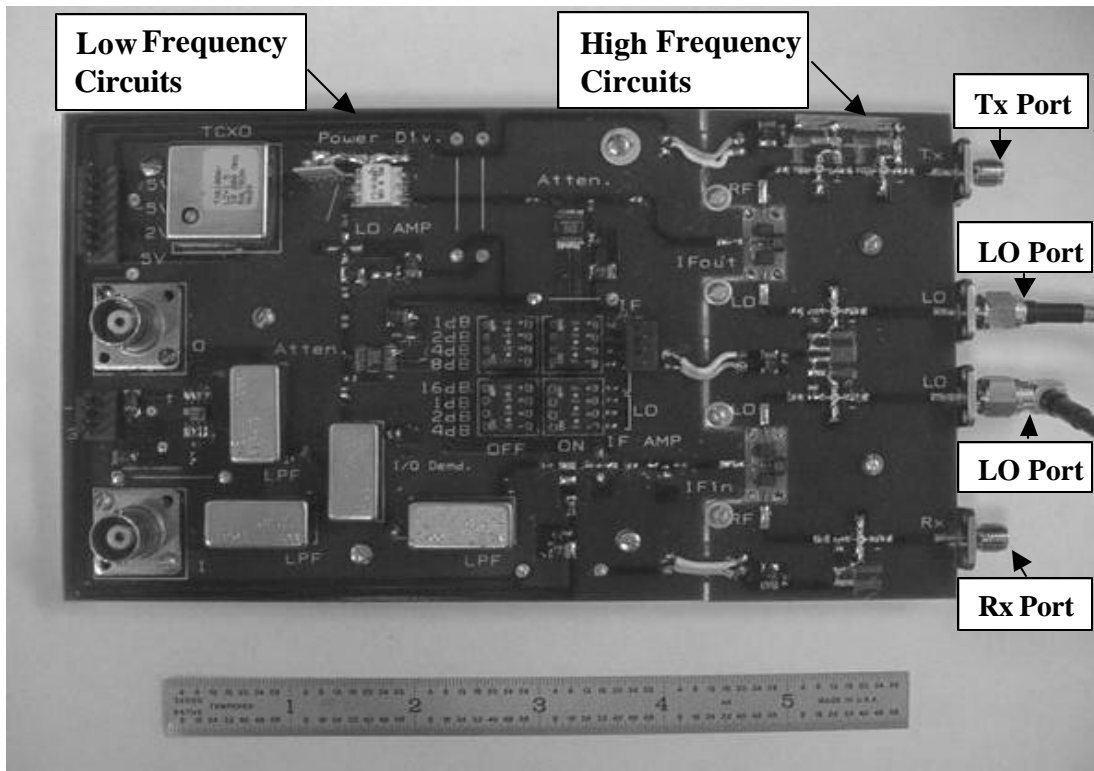
Figure 4.5 Photograph of the microwave stepped-frequency radar transceiver.

4.3 Antenna

The Antenna is a very crucial component of any surface and subsurface radar sensor system. The requirements of UWB radar sensor systems have fuelled intense research activity in the development of wideband antennas. Typical wideband radar sensors have employed transverse electromagnetic (TEM) horn antenna, as well as dipole, bow-tie, spiral, and log-periodic antennae [31]. The log-periodic antenna shows good polarization and suitable bandwidth characteristics; however, its physical size restricts its use drastically. The spiral antenna has a wide bandwidth, but it is also limited due to its dispersive characteristics. Alternately, TEM horn antennae are extremely attractive for UWB radar sensors owing to their inherent characteristics of wide bandwidth, high directivity, good phase linearity, and low distortion. Despite its excellent properties, the TEM horn antenna is also limited, due to its high cost and large size. Moreover, the waveguide horn antenna can operate only within the waveguide bandwidth, and is also expensive to manufacture. To assuage these limitations, various types of TEM horn antennae have been developed [40]-[42]. These antennae, however, prohibit a direct connection between the antenna and microwave integrated circuits. TEM horn antennae require a balun at their input, thereby limiting the operating bandwidth. The balun also makes it extremely difficult to integrate these antennas directly with the transceiver circuit. In addition, the leakage, caused by direct coupling between the transmitting and receiving antennas in the mono-static system that uses two antennas closely spaced, is inevitable.

Therefore, a cost-effective antenna that operates at UWB and is compatible with printed circuits is required for the integrated-circuit radar sensor systems. Recently, a new type of antenna that shows an extremely broad bandwidth of multiple decades, relatively high gain, and compatibility with microstrip circuits, was developed and demonstrated up to 18 GHz [43], [44]. Based on this concept, two new classes of UWB antennae were developed. One was developed for the microwave SFCW radar sensor system, and the other operating at the Ka-band was also presented for potential usage in the millimeter-wave SFCW radar sensor system. These antennae have similar performance compared to the waveguide horn antennae, but they can operate over wider bandwidths, do not need a transition to printed circuits, and are much easier to produce at a much lower cost.

4.3.1 Antenna for Microwave SFCW Radar Sensor System

The microstrip quasi-horn antenna for the microwave SFCW radar sensor was designed to present at least 10 dB of return loss over a wide band of 0.5-10 GHz. The length of the antenna, which is primarily restricted by the lowest operating frequency, was set to 16 inches. Its design was described in detail in [43]. Figure 4.6 shows a sketch of the fabricated antenna. The antenna used Styrofoam, which has the nearly same relative dielectric constant (i.e., $e_r = 1.03$) as the air, as a dielectric medium and a supporter for the antenna's top conductor. Reflections from the open end and the edges were significantly reduced by appending a resistive pad to the open end and absorbers to the edges as illustrated in Figure 4.6.
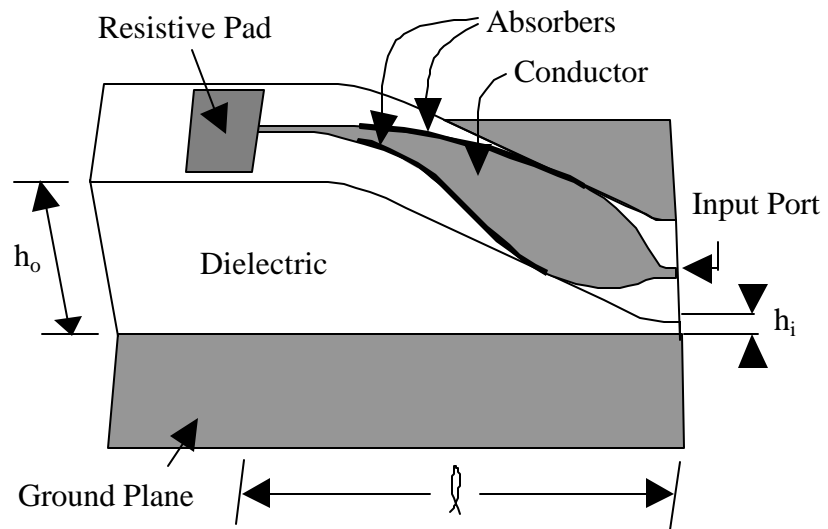
Figure 4.6 Sketch of the UWB antenna.

The resistive pad, which is made of a metal film with a thickness and resistivity of 0.025 inches and 250 ohms/square respectively, was tuned empirically to an optimal size of 2x3 inches. Electromagnetic simulations were performed using Ansoft's HFSS to theoretically verify the far field radiation patterns. Figure 4.7 shows the measured return loss in both the time and frequency domains. The return loss at the low frequency end, as seen in the frequency-domain plot, is improved significantly due to the incorporation of the resistive pad and absorbers. The measured return loss is better than 12dB at 0.6-10-GHz as shown in Figure 4.7 A better illustration of the impact of these accessories is shown in the time domain plots. An additional narrow peak, indicating deterioration of the input reflection loss, is observed at around 3.5 ns when the resistive pad and absorbers were not incorporated.

The simulation results of the radiation patterns in the E-plane show that the gain and the 3dB beam width are within 6-17dBi and 25-45degrees at 0.6, 3, and 5GHz, respectively, as shown in Figure 4.8(a-c).
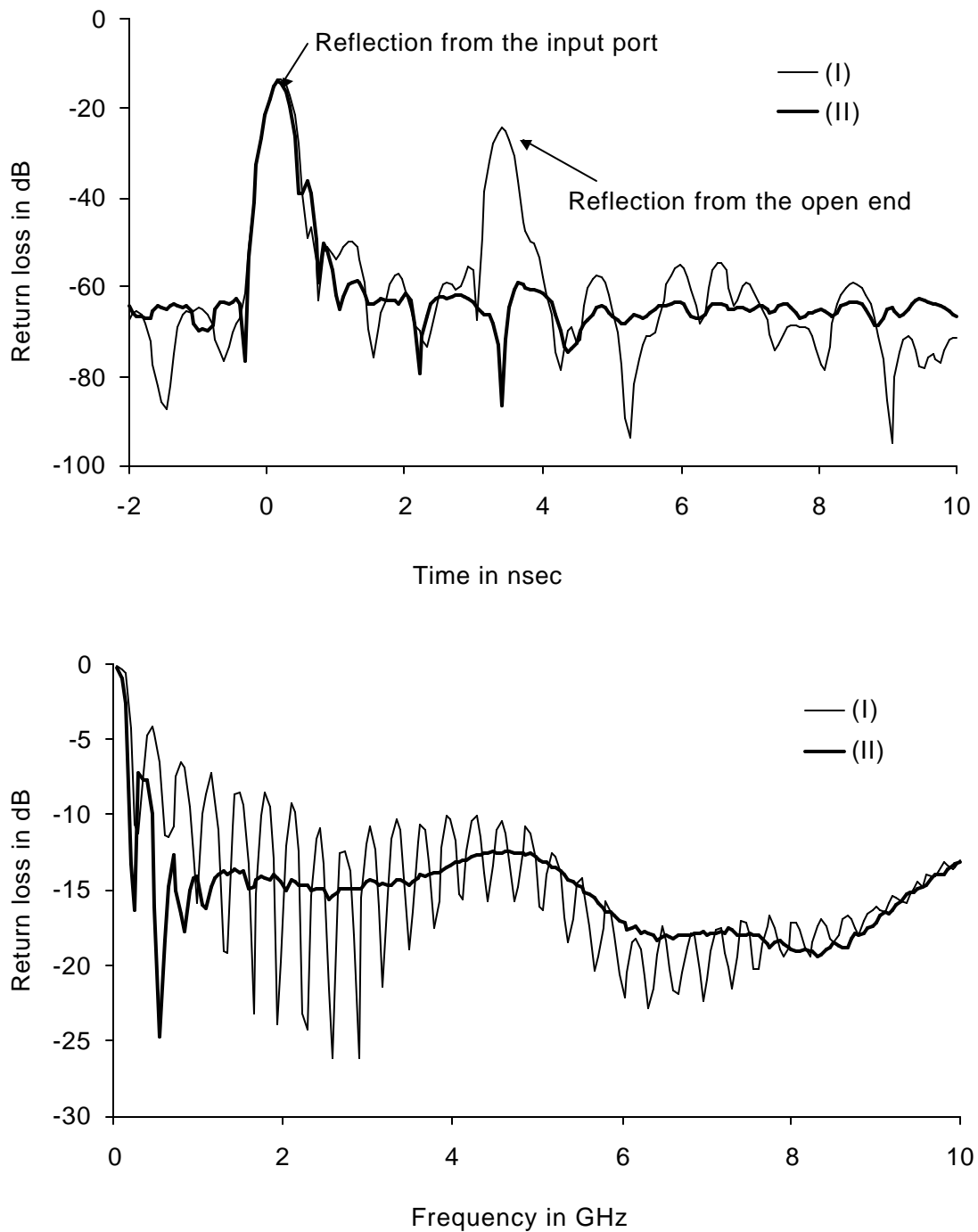
Figure 4.7 Antenna's return loss; (a) in the time domain (b) in the frequency domain, where (I) indicates the antenna alone and (II) represents the antenna with a resistive pad and absorbers.
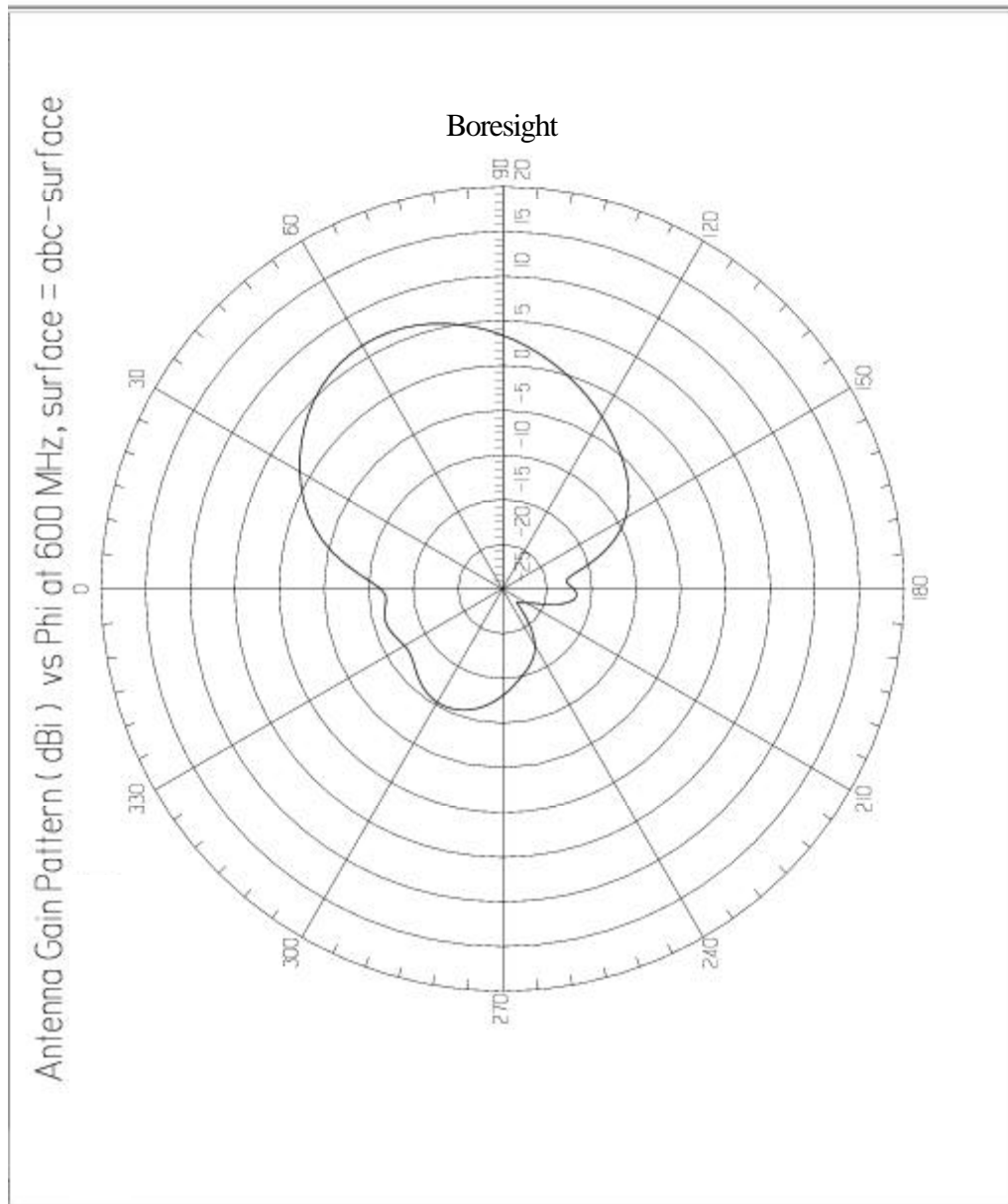
Figure 4.8 (a) Calculated radiation pattern of E-plane at 0.6GHz.
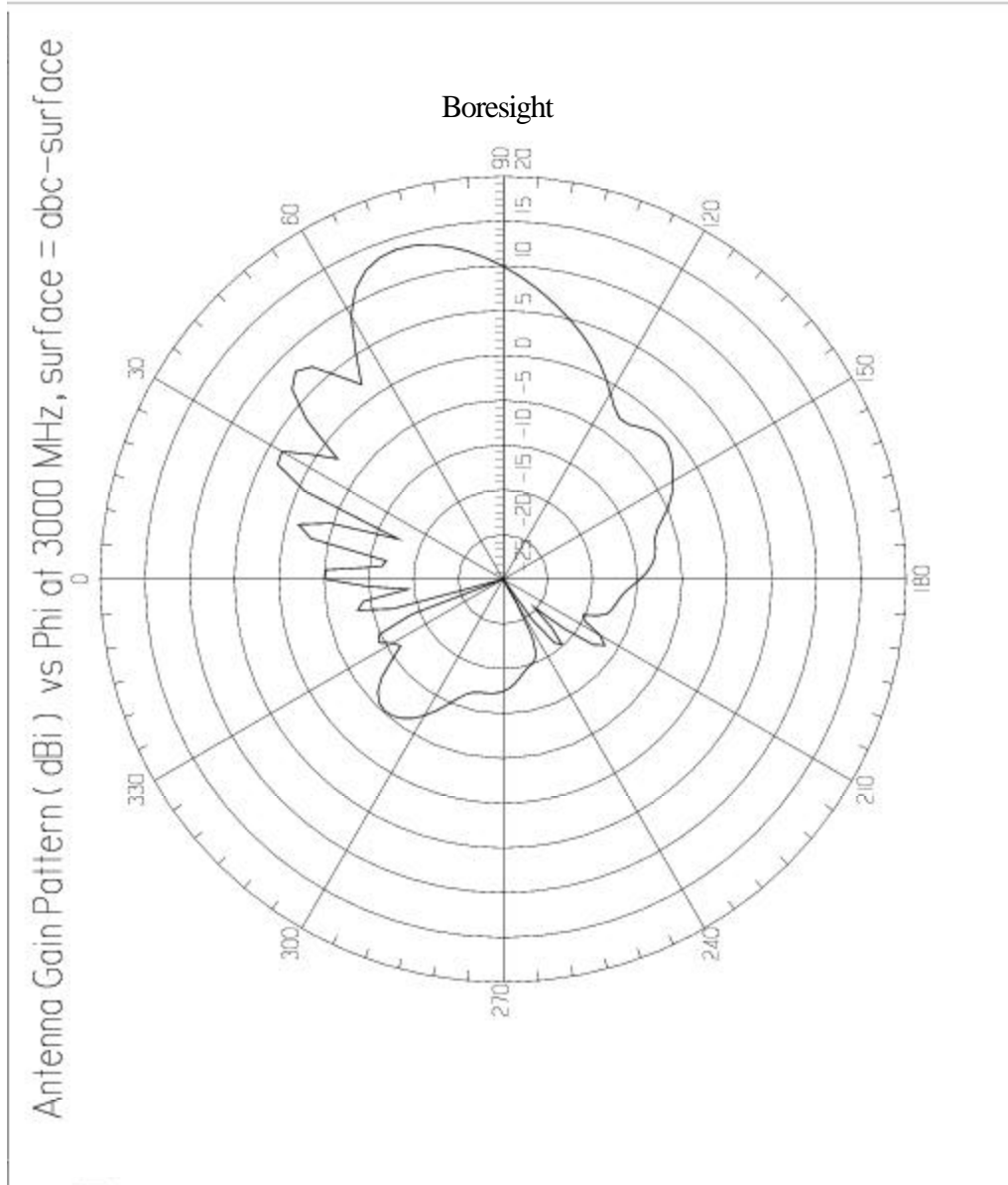
Figure 4.8 (b) Calculated radiation pattern of E-plane at 3GHz.
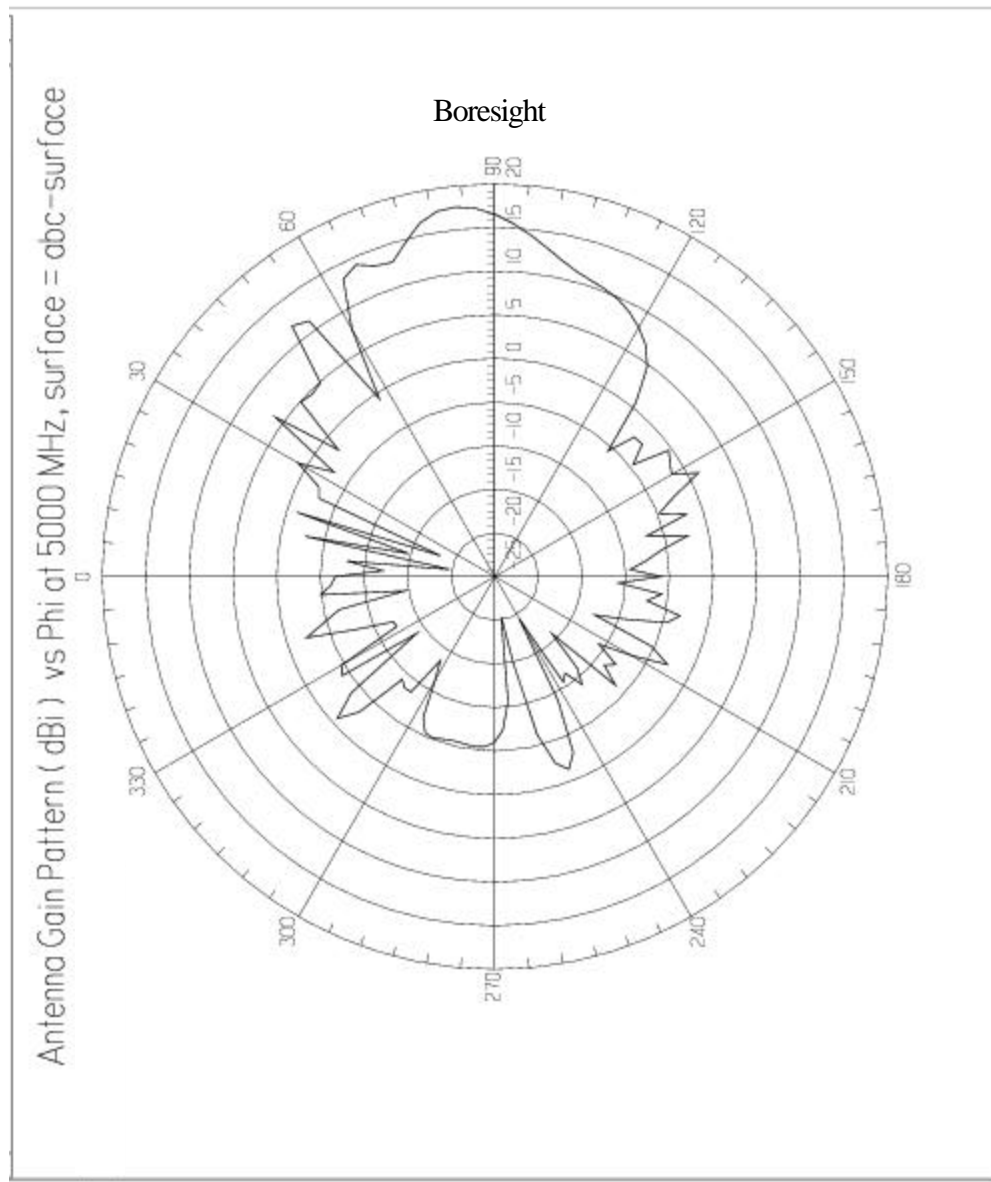
Figure 4.8 (c) Calculated radiation pattern of E-plane at 5GHz.

The simulated results show that E-planes are tilted about 8-28 degrees off the boresight axis due to the ground-plane effect. Therefore, the transmitting and receiving antennae should be carefully aligned to achieve maximum possible gains. To optimize an alignment of two antennas, the measurement was performed on a metal plate using the Network Analyzer. Figure 4.9 shows the configuration of the aligned antennas. A set of initial values for the angle, stand-off distance, and gap were obtained from EM simulations, and then they were tuned. Figure 4.10 shows the measured insertion loss of the two developed antennas where the optimum alignment is 65 degrees of the angle, 20cm of distance, and 7cm of gap.
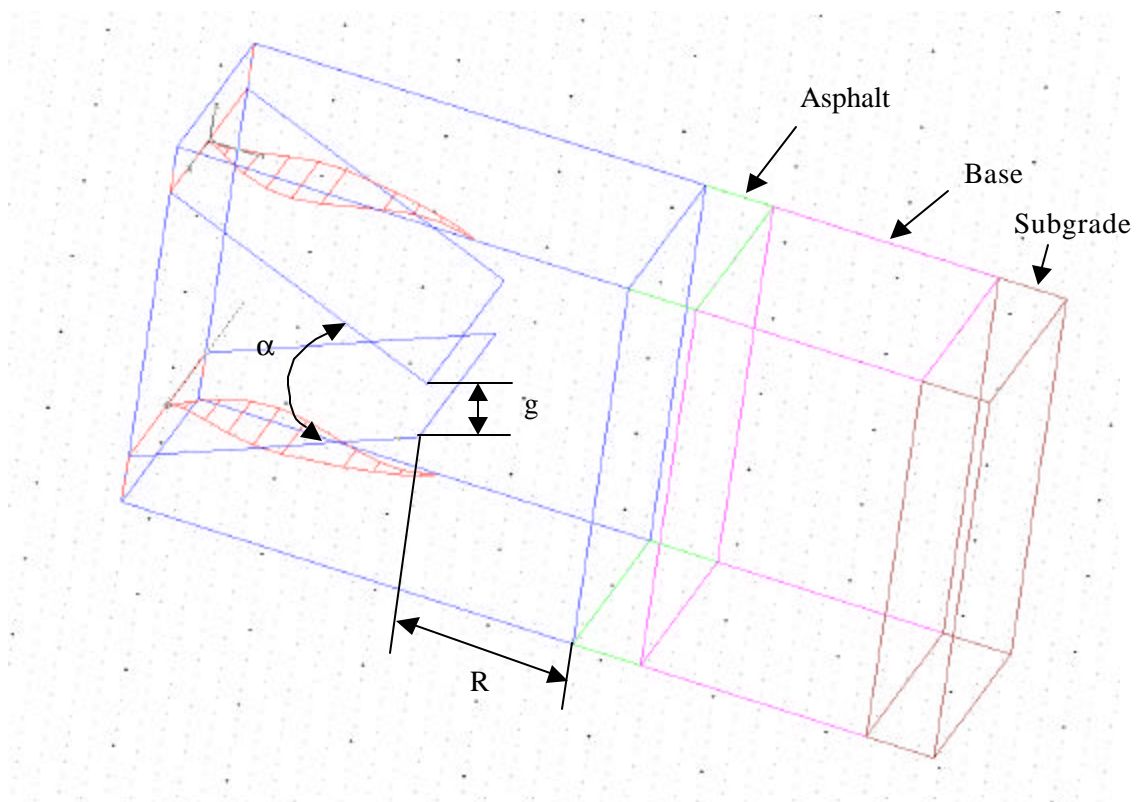
Figure 4.9 Configuration of the aligned antennas.
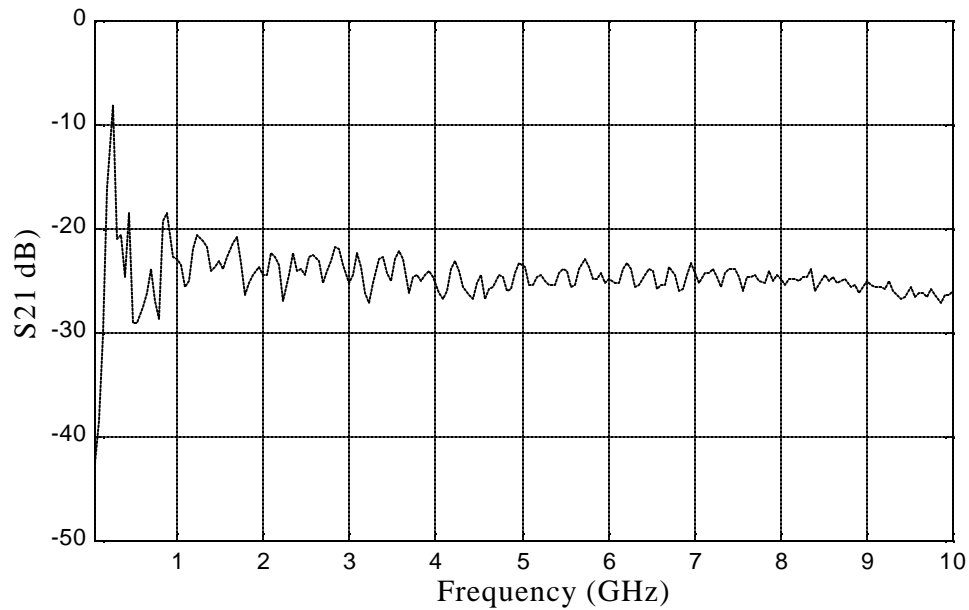
Figure 4.10 Measured S21 of the two aligned antennas.

4.3.2 Antenna Operating at Ka‑Band

Figure 4.11 shows the photograph of the fabricated Ka‑band microstrip quasi‑horn antenna. As can be seen from Figure 4.11, the antenna was directly connected to the OS‑50 connector without a balun, which results in simpler‑structure physically and higher‑performance electrically. To improve both the impedance transformation and the antenna radiation characteristic, especially at lower frequency, the antenna was shaped by a combination of the exponential and cosine‑squared functions to determine the height between the top conductor and the ground plane. This combination was selected by comparing the results of the simulations. The exponential function was used to determine the height up to one‑half wavelength of the lowest frequency (26.5GHz) and the cosine‑squared function was

used for the height from one-half wavelength to the open end. The impedance change from

the input port to the open end followed an exponential taper.
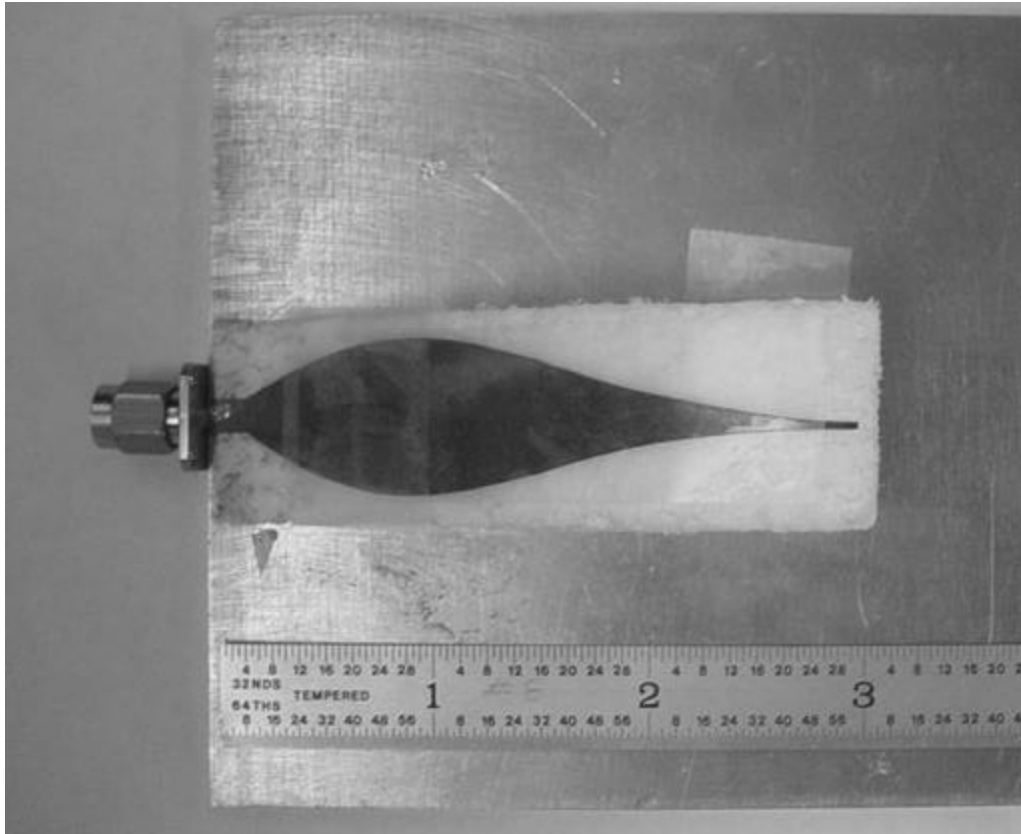
Figure 4.11 Photograph of the Ka-band microstrip quasi-horn antenna.

Figure 4.12 shows the measured return loss of the designed microstrip quasi-horn antenna, which is better than 14 dB from 20 to 40 GHz. Figures 4.13 (a-b) show the calculated and measured H-plane radiation patterns at 26.5 and 35GHz, respectively, where the patterns are measured and calculated within –90º to +90º from the boresight. The calculated and measured gains are within 16-18 and 14.5-15 dBi, respectively. Both the computed and measured half-power beamwidths are less than 20 degrees. The calculated and measured E-plane radiation patterns at 26.5 and 35GHz, respectively, are displayed in Figures 4.14 (a-b) while the corresponding gains are within 16-18.5 and 14.5 -15.5 dBi, and their beamwidths are about 22 and 15 degrees, respectively. All the calculations were carried out using Ansoft HFSS. The measured H-plane radiation patterns reasonably agreed with the calculated results, despite some physical dimension errors. However, the measured E-plane radiation patterns show lower gain due to a finite ground plane. It was impossible to achieve the same dimensions and shapes as those used in the simulations because the top conductor and foam were cut and integrated manually. It is important to note that both the measured and simulated radiation patterns of the E-plane are tilted about 10 degrees off the boresight axis, due to the ground-plane effect.
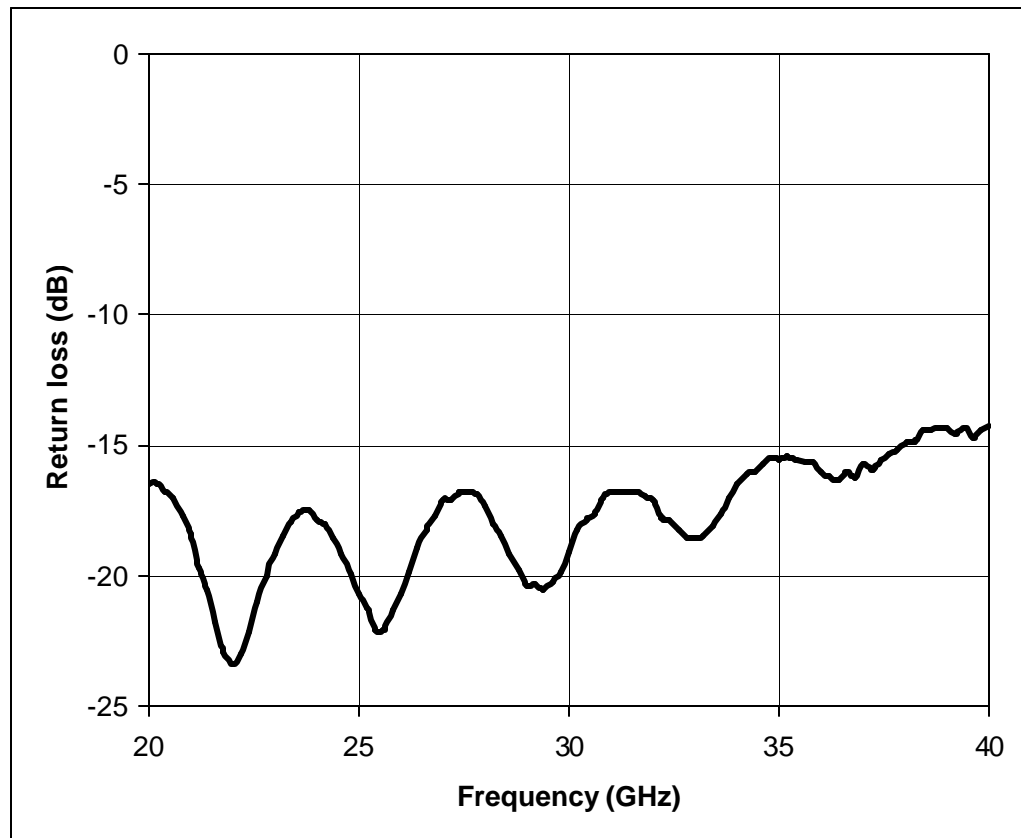
Figure 4.12 The measured return loss of the microstrip quasi-horn antenna.
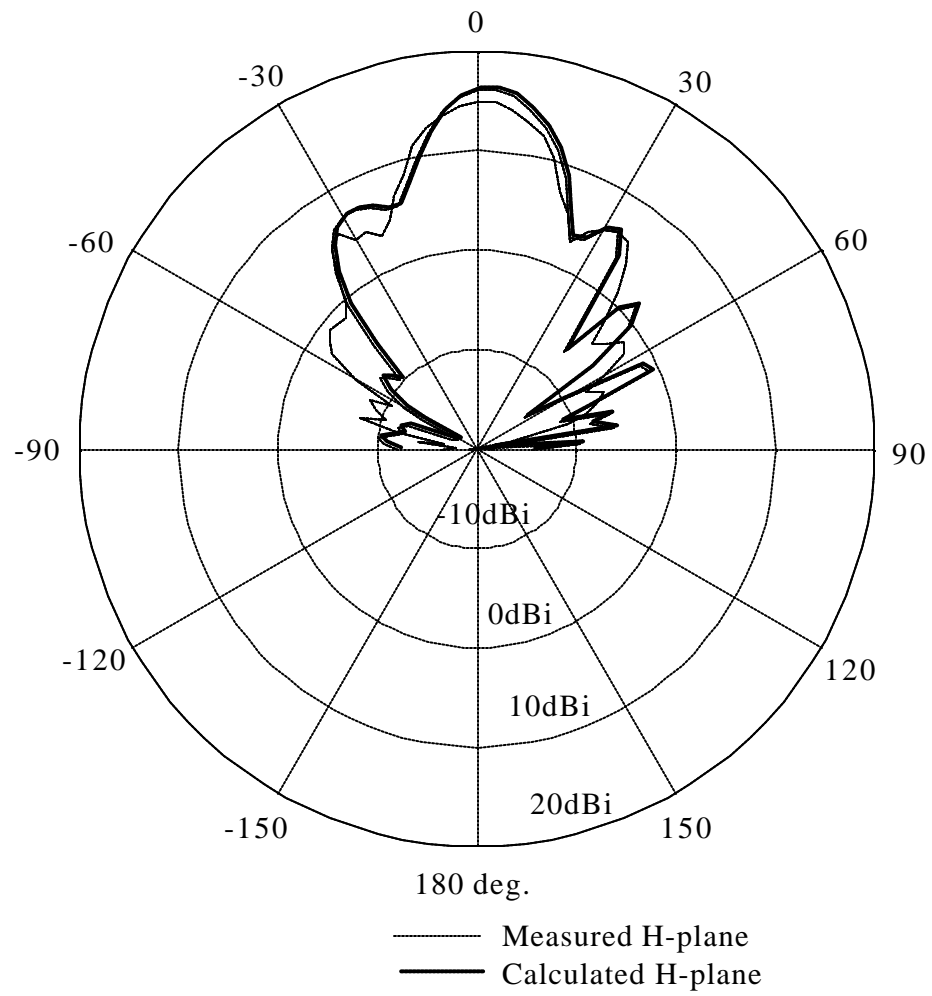
Figure 4.13 (a) Radiation patterns of the measured and calculated H-planes at 26.5GHz.
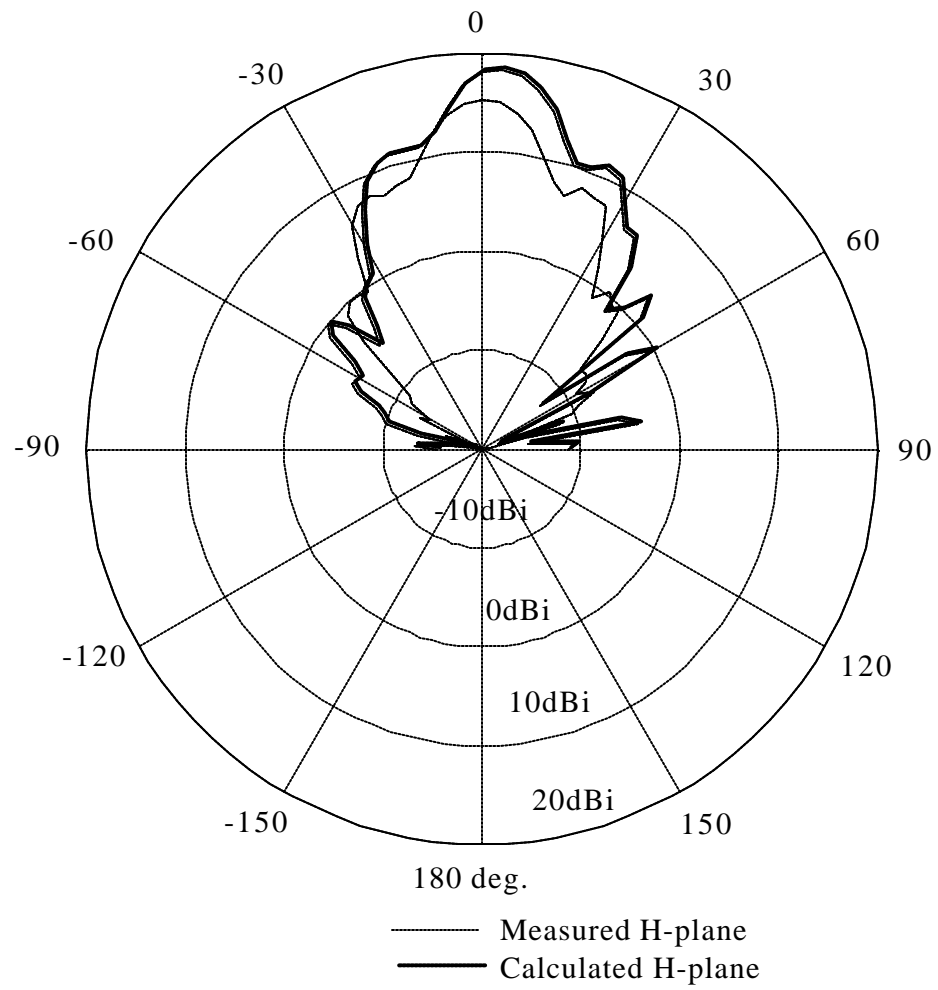
Figure 4.13 (b) Radiation patterns of the measured and calculated H-planes at 35GHz.
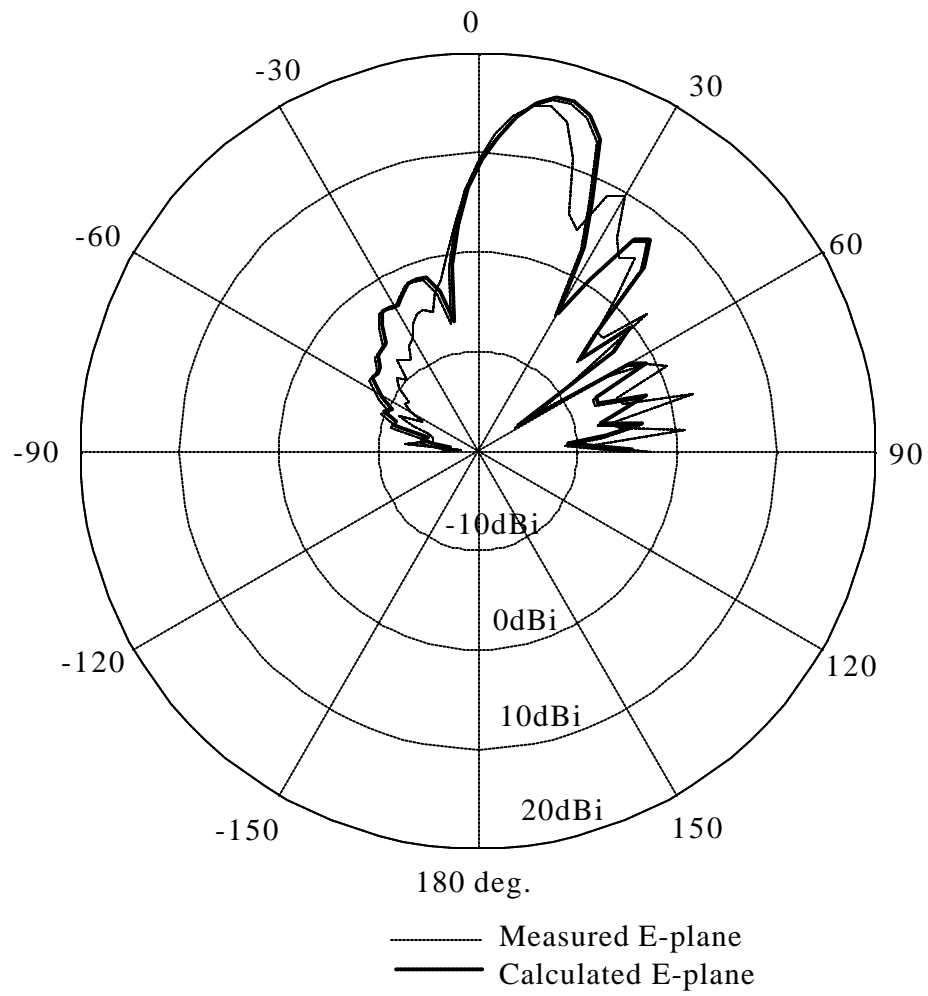
Figure 4.14 (a) Radiation patterns of the measured and calculated E-planes at 26.5GHz.
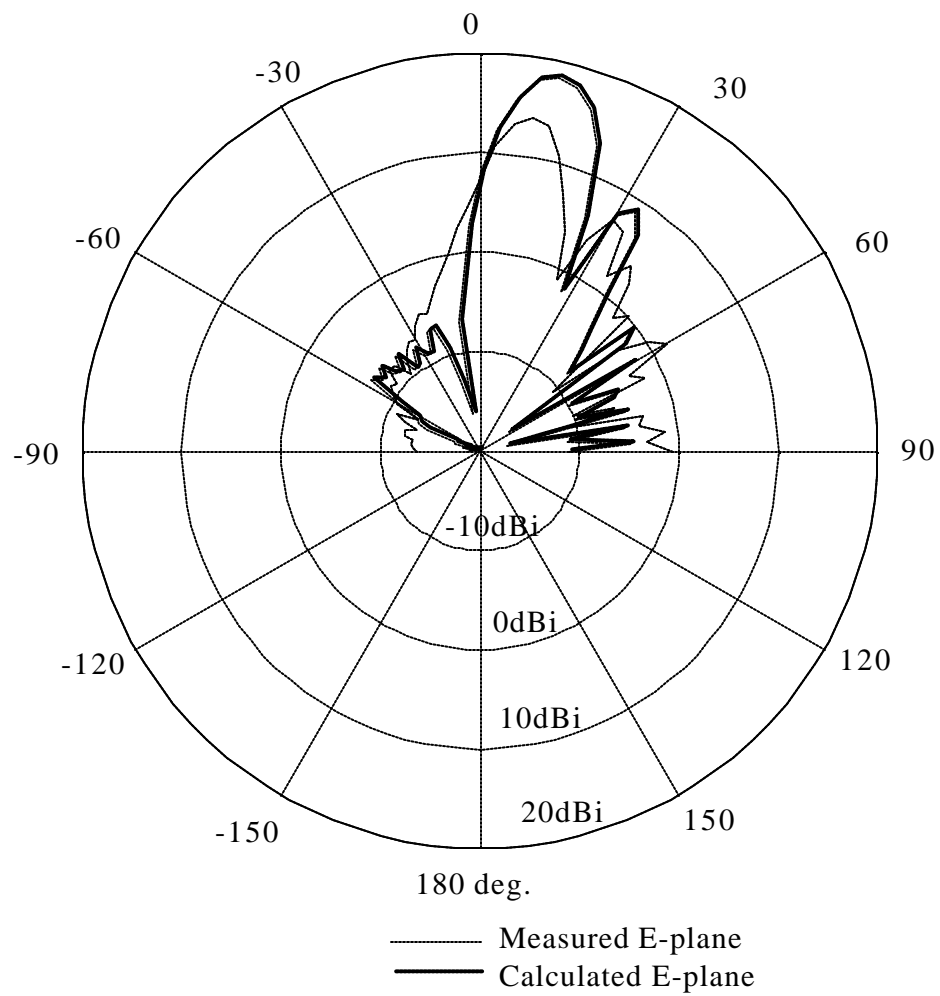
Figure 4.14 (b) Radiation patterns of the measured and calculated E-planes at 35GHz.

4.4 Signal Processing

The base-band analog I/Q signals are digitized into digital I/Q signals at ADCs in the DAQ board of the Labview. These digitized I/Q signals need signal processing to be transformed into synthetic pulses in time domain. Therefore, signal processing including I/Q error compensation and IDFT was developed using LabView.

The returned stepped-frequency from a target must be synchronized during data acquisition. Namely, a start point of data acquisition should coincide with the desired first step frequency. To synchronize the first step frequency to the starting point of acquisition, a trigger input was used, and Labview was programmed to utilize the trigger input for synchronizing data acquisition.

The I/Q data collected through data acquisition is processed to compensate for the I/Q errors, where the I/Q errors for compensation were focused on some common amplitude and phase errors because the differential amplitude and phase errors, can be easily compensated in the super-heterodyne scheme [45]. These compensated I/Q signals were then formed into complex vectors (i.e., $I_i + jQ_i$, $i = 0,1\ldots$N-1), and $(M - N)$ zeros were added on the complex vectors before being composed into an array.

Finally, the array was applied by a hamming window to reduce side lobes, and then transformed to a synthetic pulse in the time domain.

4.4.1 Acquisition and Restoration of Complex Vectors

The digitized I and Q samples from ADCs needed to be synchronized, restored, filtered and averaged to obtain a representative data point. Figures 4.15(a-b) represent the train of the frequency steps of the transmitted and returned signals, respectively. The settling time, z, of a synthesizer, and the delayed time, t, of the received signals should be considered, since non-coherent demodulation occurs during the time $z + t$. The samples are useless during the time $z + t$, and it is thus necessary to restore the samples with effective samples only.
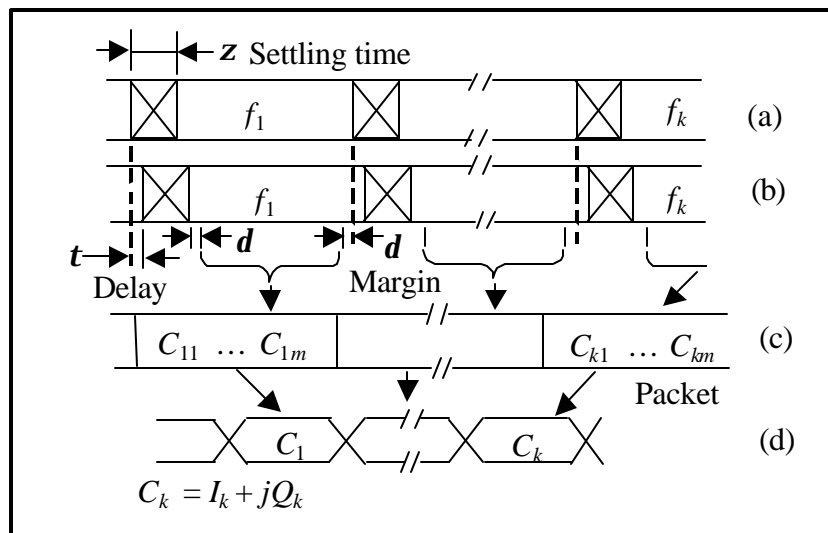
Figure 4.15   Procedure for generating representative complex vectors: (a) transmitted signals, (b) received signals, (c) restored effective complex vectors, (d) representative complex vectors after averaging.

The effective samples shown in Figure 4.15(c) are reconstructed such that there are adequate safety margins (*d*) to ensure that each packet has valid samples. The samples in each packet, C_{k1}, C_{k2}, ..., C_{kn} (k=0, 1, 2, ..., N-1) where C_{kn} denotes the mth complex vector corresponding to the kth frequency, are filtered and averaged to generate a new complex vector, C_k, as shown in Figure 4.15(d). Averaging the samples reduces the errors caused by short time jitters of the TCXO and synthesizer.

4.4.2 Compensation for the I/Q Errors

A practical (non-ideal) system produces common and differential amplitude and phase errors in the I and Q channels. The common errors are errors caused by the common circuits in the signal-propagation path to both the I and Q channels, which consist of the antennae, amplifiers, mixers, transmission lines, filters, etc. The differential errors are caused by a mismatch between the I and Q channels. These errors are generated in the quadrature detector, due to the difference between the two mixers and the phase imbalance of the 90-degree coupler contained in the quadrature detector. For a super-heterodyne scheme, the differential amplitude and phase errors in the I and Q channels are constant over the band of interest, as discussed earlier.

In the absence of errors in the I/Q channels, the phase j_i of the base-band I and Q signals, expressed in terms of the target range d and frequency step f_i, given by

$$j_i(d, w_i) = -\frac{2dw_i}{n} = -w_i t, \quad i = 0, 1, ..., N-1 \qquad 4.1$$

where $\mathbf{n}$ is the speed of the electromagnetic wave in the medium, $\mathbf{w}_i$ is the angular frequency step, and N is the number of the frequency steps. The time delay $\mathbf{t}$ is equal to a two-way travel time of $2d/\mathbf{n}$. The complex vectors corresponding to a fixed target are expressed in terms of the angular frequency $\mathbf{w}_i$ as

$$
\begin{aligned}
I_i(\mathbf{w}_i) + jQ_i(\mathbf{w}_i) &= A_i \cos\!\big[\mathbf{j}_i(\mathbf{w}_i)\big] + jA_i \sin\!\big[\mathbf{j}_i(\mathbf{w}_i)\big] \\
&= A_i \exp(-j\mathbf{w}_i \mathbf{t}), \quad i = 0,1,2...,N-1
\end{aligned}
\tag{4.2}
$$

where A_i is the amplitude.

If the common and differential errors are included, the complex vectors become, (assuming $A_i = 1$ for simplicity without loss of generality):

$$
\begin{aligned}
I_i(\mathbf{w}_i) + jQ_i(\mathbf{w}_i) &= (1 + \frac{cg_i}{2})\cos\!\big[\mathbf{t}\mathbf{w}_i + cp_i\big] \\
&- j(1 + dg_i + \frac{cg_i}{2})\sin\!\big[\mathbf{t}\mathbf{w}_i + dp_i + cp_i\big]
\end{aligned}
\tag{4.3}
$$

where $i=0,1,2,\ldots,N\text{-}1$, cg_i and cp_i are the common amplitude and phase errors, and dg_i and dp_i are the differential amplitude and phase errors, respectively.

The differential amplitude and phase errors generate a Hermitian image of the response in the resultant synthetic range profile, resulting in a reduction of the sensor's unambiguous range by one-half [45]. In a super-heterodyne system, these errors are constant in the operating frequency range, as a single constant intermediate frequency is used for the quadrature detector. Consequently, measurement and compensation of these errors is simple. The differential amplitude and phase errors in the I and Q channels at an intermediate frequency can be measured by using the methods presented in [18], [45]. By

following these techniques, the differential amplitude and phase errors were measured as 1 dB and 3 degrees, respectively, for the microwave stepped-frequency radar sensor and 3.5 dB and 7 degrees, respectively, for the millimeter-wave stepped-frequency radar sensor.

The common phase error consists of a linear phase error $a w_i$ and a non-linear phase error b_i as

$$cp_i = a w_i + b_i, \quad i = 0,1,...,N-1 \qquad 4.4$$

The common linear phase error results in a constant shift of the response in the synthetic range profile, due to the fact that a frequency-dependent linear phase is transformed into a constant time delay through the Inverse Fourier Transform [38]. Therefore, it is not necessary to correct the common linear phase error. However, the non-linear phase error causes shifting as well as an imbalance in the response of the synthetic range profile. The common amplitude error affects the shape of the synthetic range profile significantly, as they tend to defocus the response in the profile and increase the magnitudes of side lobes. Therefore, these common non-linear phase and amplitude errors need to be corrected. For their compensation, a new simple, yet effective and accurate, technique has been developed.

The complex vector given in equation (4.3) for a fixed angular frequency w_k is rewritten in terms of the range d as

$$
\begin{aligned}
I(d) + jQ(d) = (1 + \frac{cg_k}{2}) \cos\left[t(d)w_k + cp_k\right] \\
- j(1 + dg_k + \frac{cg_k}{2}) \sin\left[t(d)w_k + dp_k + cp_k\right]
\end{aligned}
\qquad 4.5
$$

from which, it is seen that these complex vectors will rotate circularly if the I/Q channels are completely balanced when *d* is increased or decreased at a constant rate.   In   the process of correction, the complex vector, *I(d)+jQ(d)*, is measured when a metal plate is moved along a track at a fixed frequency. Initially, the complex vector rotates elliptically, either clockwise or counter-clockwise, with respect to the direction of the metal plate, as the I and Q components, are not orthogonal due to the differential phase errors. After these differential errors are corrected, equation (4.5) can be rewritten as

$$
\begin{aligned}
I(d) + jQ(d) &= (1+\frac{cg_k}{2})\cos\left[\boldsymbol{t}(d)\boldsymbol{w}_k + cp_k\right] \\
&\quad - j(1+\frac{cg_k}{2})\sin\left[\boldsymbol{t}(d)\boldsymbol{w}_k + cp_k\right]
\end{aligned}
$$

4.6

from which, it is seen that the I and Q components become orthogonal in phase and balanced in amplitude, hence the complex vector *I(d)+jQ(d)* starts rotating circularly during the movement of the metal plate at a fixed frequency. The magnitude of the rotating vector is then measured and stored. This procedure is repeated at each frequency step across the operating frequency range. These measured magnitudes are used as reference data to compensate for common amplitude errors.

After compensating for the common amplitude errors, the normalized complex

vectors $I+jQ$ can be expressed, using equation (4.6), which can be written as

$$I(d) + jQ(d) = \cos\left[\boldsymbol{t}(d)\boldsymbol{w}_k + cp_k\right] - j\sin\left[\boldsymbol{t}(d)\boldsymbol{w}_k + cp_k\right]\qquad 4.7$$

From equation (4.7), the phase of the complex vector $I+jQ$ is obtained as $\boldsymbol{t}\boldsymbol{w}_k + \boldsymbol{a}\boldsymbol{w}_k + \boldsymbol{b}_k$

with the aid of equations (4.4-5). As mentioned earlier, the non-linear phase error $\boldsymbol{b}_k$ needs

to be corrected. Figure 4.16 depicts the calculated phases, $\boldsymbol{t}\boldsymbol{w}_k + \boldsymbol{a}\boldsymbol{w}_k + \boldsymbol{b}_k$, over a

frequency range. Cumulating the phase difference between two consecutive frequency steps,

$\boldsymbol{DF}_{(k-1,k)} = \boldsymbol{t}\boldsymbol{w}_k + \boldsymbol{a}\boldsymbol{w}_k + \boldsymbol{b}_k - \boldsymbol{t}\boldsymbol{w}_{k-1} - \boldsymbol{a}\boldsymbol{w}_{k-1} - \boldsymbol{b}_{k-1}$, unwraps the calculated phases and

makes it easy to draw the trace of the calculated phases as shown in Figures 4.16 (a-b).

Figure 4.16 (c) shows that the rotation of the vector $I+jQ$ is not constant, due to the non-

linear phase error $\boldsymbol{b}_k$.
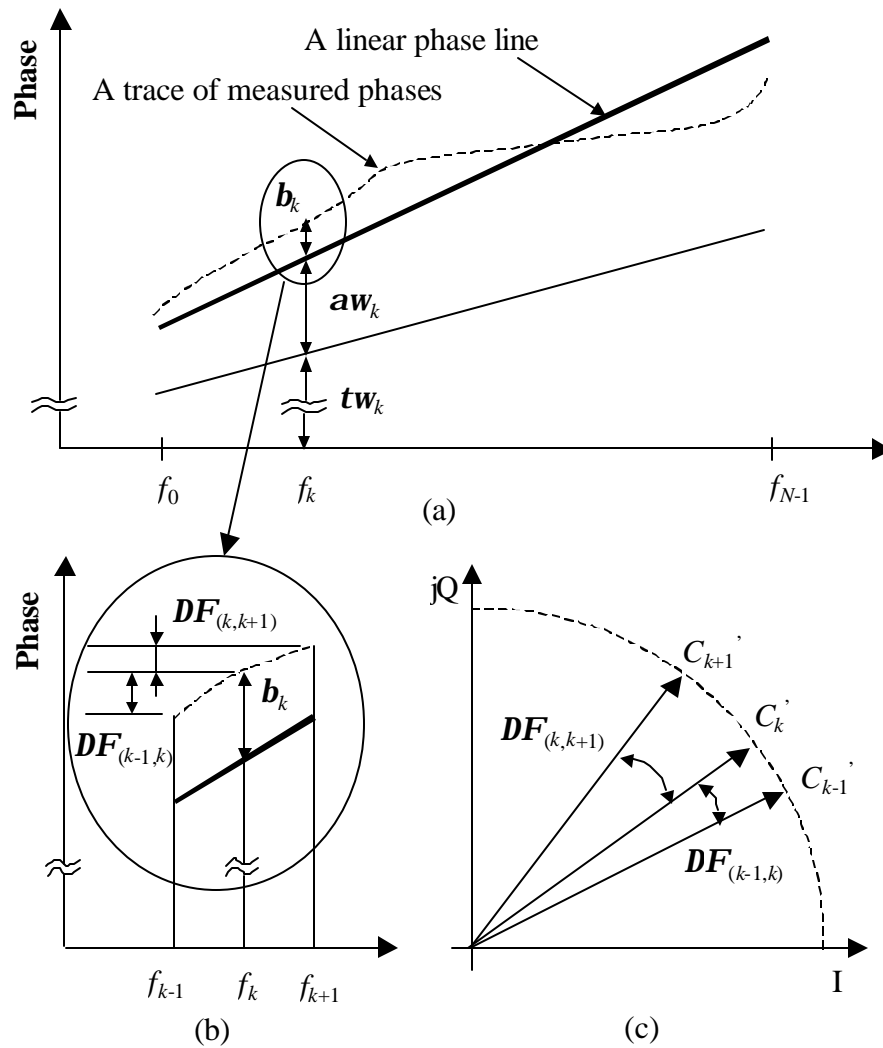
Figure 4.16 Phase of the complex vector $I+jQ$ versus frequency: (a) linear transformation of the trace of calculated phases to a linear phase line, $(a+t)w_k$; (b) a magnified drawing of (a) showing the trace of calculated phases obtained by cumulating the phase differences $DF_{(0,1)},\ldots, DF_{(k-1,k)},\ldots, DF_{(N-2,N-1)}$; (c) non-linearity of the calculated phases in polar form, where C_k' is the kth complex vector after compensating for the common amplitude deviation.
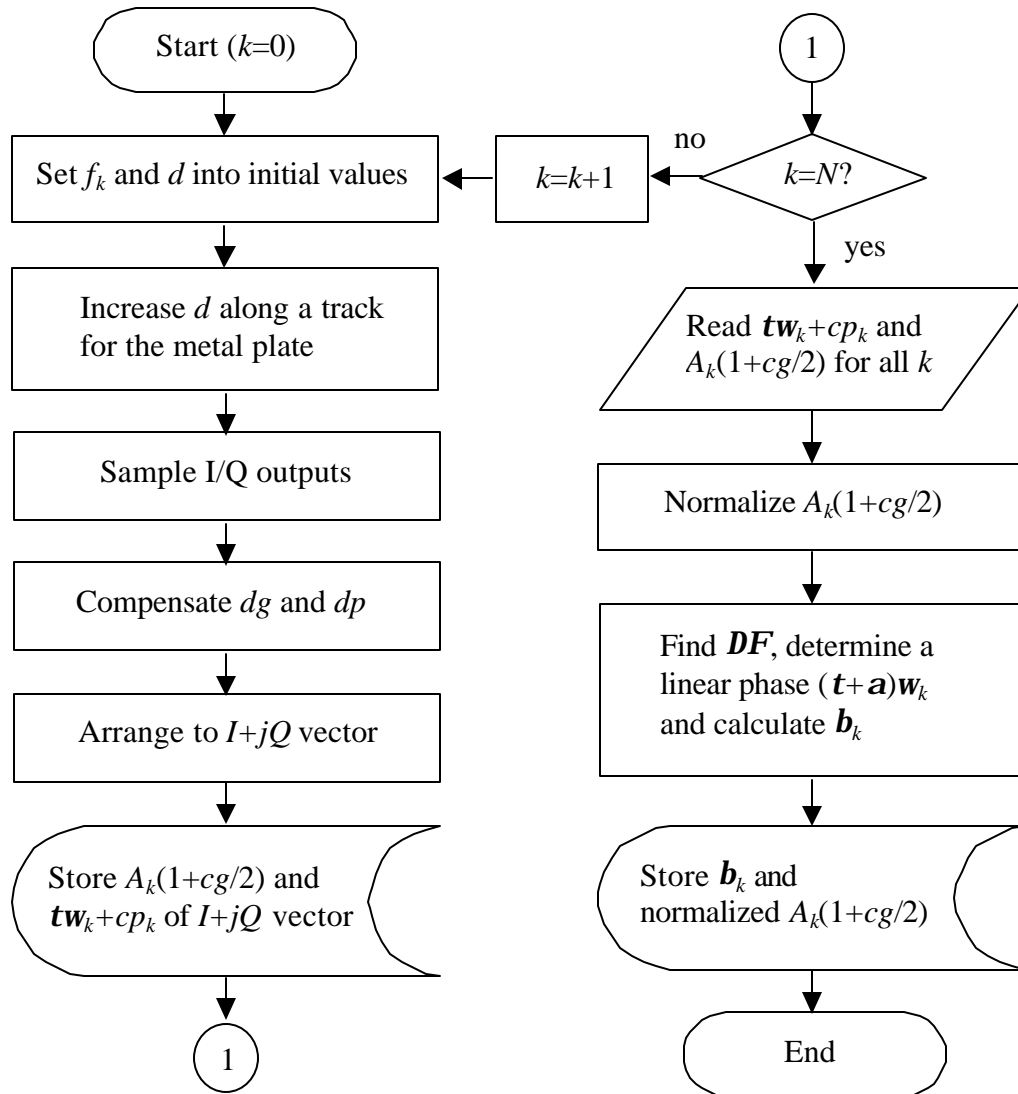
Figure 4.17 Flow chart for calculating the common errors.

After drawing an appropriate linear phase line as shown in Figure 4.16 (a), the non-linear phase error $\boldsymbol{b}_k$ is then determined by subtracting the linear phase line from the trace of the calculated phases. Consequently, the complex vector is obtained, after correcting the non-linear phase error, as

$$I(d) + jQ(d) = \cos\left[\boldsymbol{t}(d)\boldsymbol{w}_k + \boldsymbol{a}\boldsymbol{w}_k\right] - j\sin\left[\boldsymbol{t}(d)\boldsymbol{w}_k + \boldsymbol{a}\boldsymbol{w}_k\right]$$
$$= \exp\left\{-\left[\boldsymbol{t}(d) - \boldsymbol{a}\right]\boldsymbol{w}_k\right\}$$

4.8

The non-linear phase error $\boldsymbol{b}_k$ at all the frequency steps for the metal plate is stored in memory and used as reference data for compensating for the non-linear phase error of an actual target. The flow chart in Figure 4.17 shows the procedure for extracting the common amplitude and non-linear phase errors. Figure 4.18 shows the common amplitude deviations and non-linear phase errors of the measured vectors for the metal plate, used for correction in the frequency band of interest.
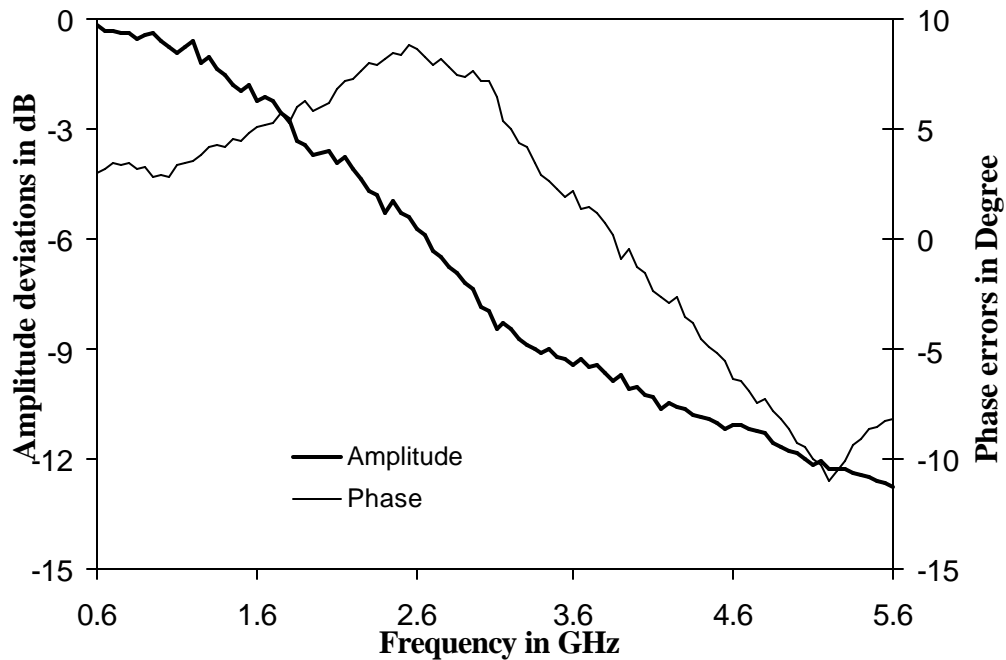
Figure 4.18 Amplitude deviations and non-linear phase errors of the complex vectors due to the imperfection of the system.

In order to compensate for the measured complex vectors of targets for the common amplitude and non-linear phase errors, the reference data, extracted from a metal plate, as described earlier, are applied to these vectors. The stored reference data for the common amplitude errors are normalized, inversed, and multiplied to the target's measured complex vectors. The stored reference data for the common non-linear phase errors are subtracted from the extracted phases of the target's measured complex vectors.

(a)   (b)
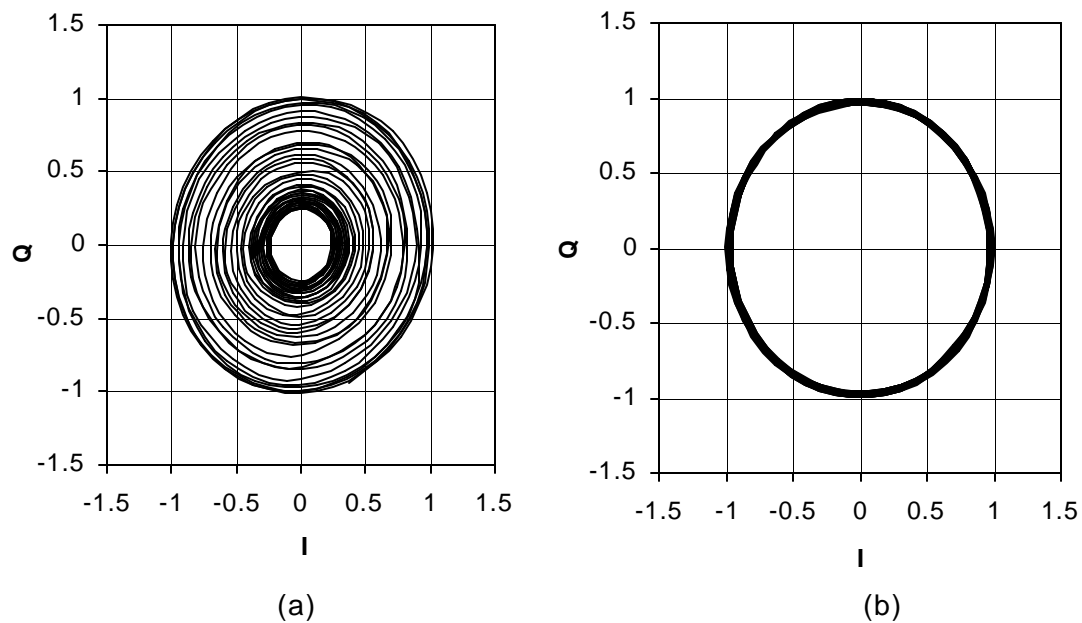
Figure 4.19   Normalized I/Q (a) before and (b) after compensating for the   amplitude deviations and non-linear phase errors.

Figures 4.19 (a-b) show the normalized I/Q outputs of the quadrature detector before and after compensating for the common amplitude and non-linear phase errors. The simulation results for a (fixed) point target are shown in Figure 4.20, which shows that the developed compensation method for the common errors not only reduces, but also balances the side-lobes of the synthetic range profile. Reduction of the side-lobes reduces the possibility of masking the responses from adjacent targets, and hence facilitating their detection. Balancing the side-lobes increases the possibility of accuracy in identifying the target. Upon compensating for the errors in the I and Q channels, the digital I and Q components are combined into a complex vector for each frequency step. An array V consisting of N complex vectors corresponding to N frequency steps is then formed as $C_{N-1} = I_{N-1} + jQ_{N-1}$. Adding ($M$-$N$) zeros to the complex vector array V generates a new array V_M of M elements. This zero padding is needed to improve the range accuracy, as discussed earlier, and the speed of the Inverse Discrete Fourier Transform (IDFT) by using Fast Fourier Transform (FFT). Finally, FFT is applied on the array V_M to get the synthetic pulse.
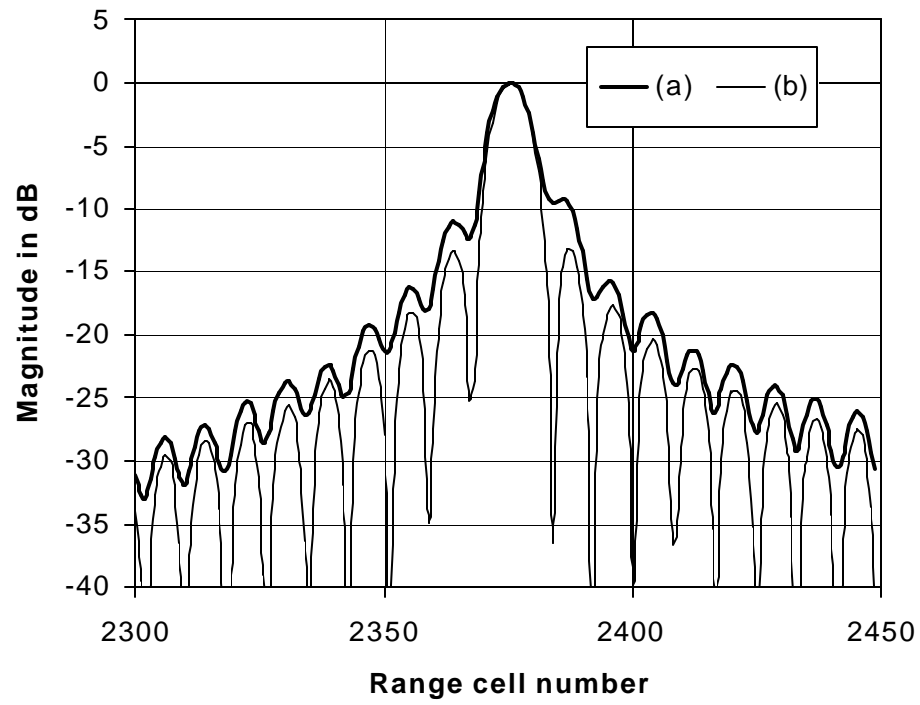
Figure 4.20   Synthetic range profile obtained from a target, whose main peak indicates the

target location: (a) before and (b) after compensating for amplitude deviations and non-linear

phase errors.

CHAPTER V

SYSTEM CHARACTERIZATION AND TESTS

This chapter discusses some of the important results achieved during experimentation with the two sensors that were developed. It also gives an insightful overview of the measurement procedure involved that helps to accurately evaluate the performance of the sensors. After validating their performance with the afore mentioned test procedures, a set of measurements were performed on various samples as well as on the actual road with these sensors. The final section describes some of the important results that were achieved with the aid of these sensors.

5.1 Electrical Characterizations of the Systems

Figure 5.1 depicts the total system built for the microwave SFCW radar sensor that consists of a transceiver, two antennae and a signal processing block. This configuration is very similar to the millimeter-wave SFCW radar sensor system that uses one single antenna for both transmission and reception. These two systems were tested for their electrical performances as described below.
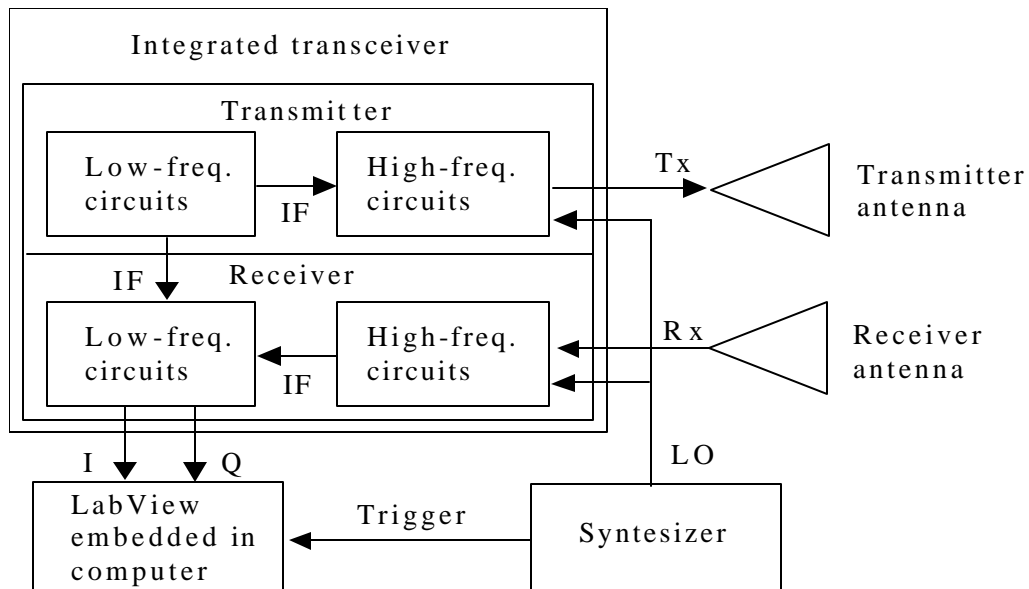
Figure 5.1 Configuration of the microwave SFCW radar sensor system.

5.1.1 Microwave SFCW Radar Sensor System

The transmission gain, denoted by G_T, of the high frequency circuits' block of the transmitter was measured in between the IF input and TX output ports over the entire operating frequency. Figure 5.2 shows that the measured transmission gains were deviated 0.4-4.7dB from the designed transmission gain of 16dB at 3GHz, as shown in the Table 4.3 in Chapter IV. The deviation was caused by losses of the FR-4 substrate and the up-converter, which in turn depend on the frequency of operation, as well as losses of the bias circuits of the cascaded amplifier.
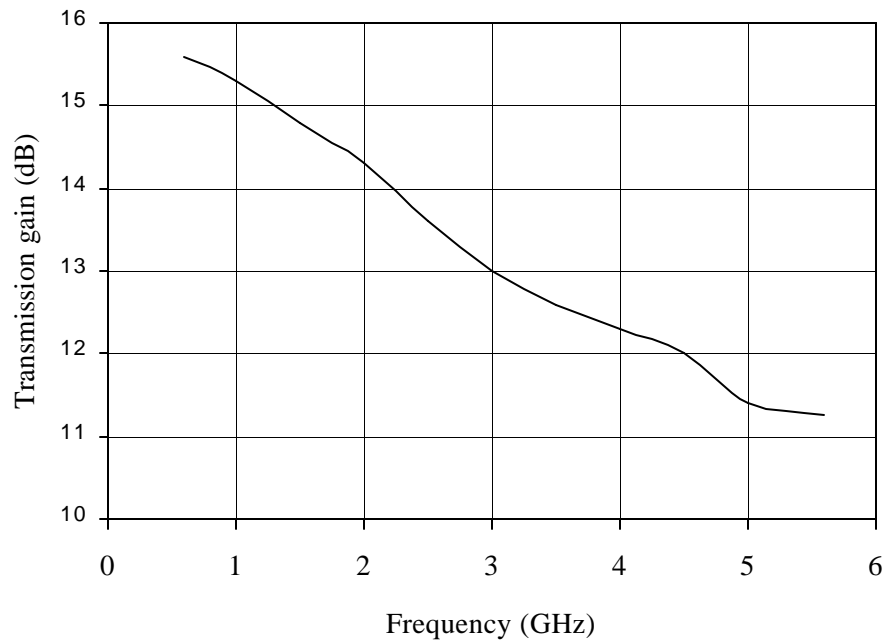
Figure 5.2 The measured transmission gain of the high frequency circuits' block of the transmitter.

Then, the output power at each component of the low frequency circuits of the transmitter was measured after adjusting the oscillator power with two attenuators to the desired specifications, viz. -1dBm at the splitter output that is fed to the LO amplifier, and –4dBm at the IF output. Table 5.1 represents the measured output power at each component of the transmitter. The measured transmitter output was in the range of 7.5-11.5dBm

Table 5.1 Measured output power of the transmitter.

	Gain	Loss	Pout	G_T
STALO			4dBm	
Attenuator		1dB	3dBm	-1dB
LPF		0.5dB	2.5dBm	-0.5dB
Splitter		3.2dB	-1dBm	-3.5dB
Attenuator		3dB	-4dBm	-1dB
Up-converter		N/A	N/A	
Amplifier	N/A		N/A	11.4-15.5dB
Amplifier	N/A		7.4-11.5dBm	
Total	N/A	N/A	-	5.4-9.5dB

Similarly, the transmission gain of the high frequency circuit block of the receiver was measured in between the Rx input and IF output ports over the entire operating frequency, where the Rx input was connected to the Tx output through a 25dB attenuator that takes into account the 25dB transmission loss L_t, as mentioned in Chapter IV. Figure 5.3 shows that the measured transmission gains were deviated 0.4-2.5dB from the designed transmission gain of 4dB, as shown in the Table 4.4 in Chapter IV. These errors are caused by similar reasons as in the case of the transmitter.
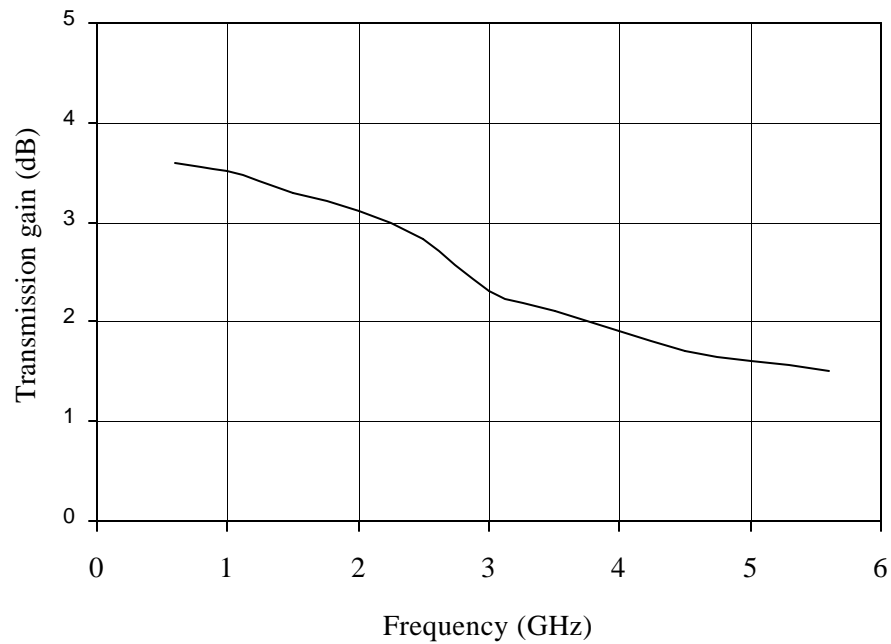
Figure 5.3 The measured transmission gain of the high frequency circuit's block of the receiver.

Figure 5.4 shows the linearity of the high frequency circuit block of the receiver. The measured input 1dB compression point of the high frequency circuit block was -4dBm at 3GHz. Then, with the aid of a video amplifier that increases the maximum output power (= -7.4dBm) of the quadrature detector, the ADC's maximum input range constraint of (= 9dBm) was satisfied. Table 5.2 represents the measured receiver's electrical characteristics.
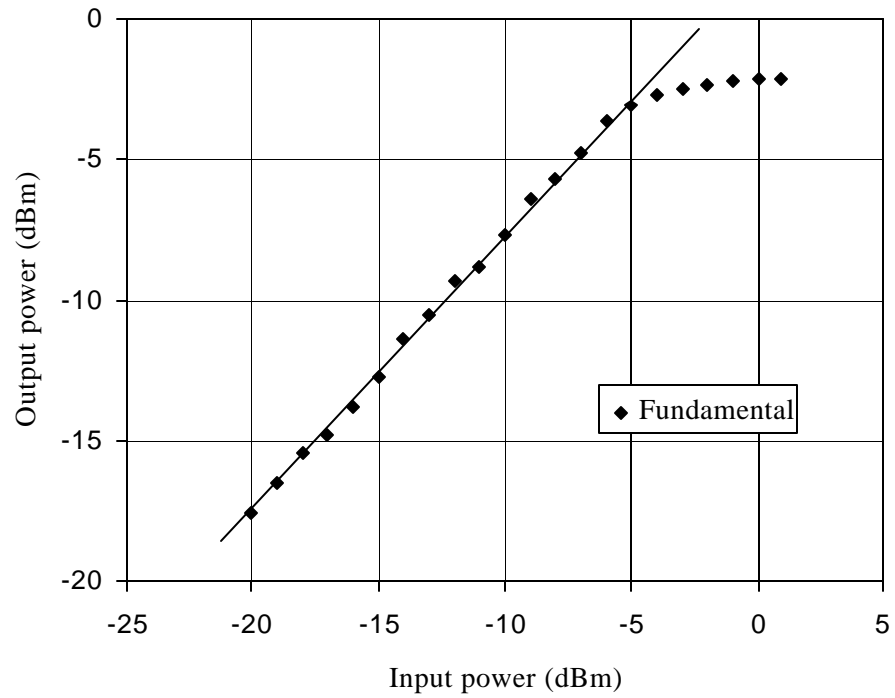
Figure 5.4 Linearity of the high frequency circuit's block of the receiver at 3GHz.

Table 5.2 Measured output power at each component of the receiver where the input power

was in the range of –17.6 to –13.5dBm.

	Gain(Vo/Vi)	Loss	Pout	G_T
LNA	N/A	N/A	N/A	1.5-3.6dB
Down-conv.		N/A	-16.1 to –9.9dBm	
LPF		0.5dB	-16.6 to –10.4dBm	-0.5dB
Amplifier	13dB		-4.6 to 1.6dBm	12dB
I/Q mixer		8.5dB	-13.6 to-7.4dBm	-9dB
LPF(Ro=200)		0.2dB	-19.8to-13.6dBm	-6.2dB
Amp.(Ro=1k)	29.6dB		2.8-9dBm	22.6dB
Total	N/A	N/A	-	20.4-22.5dB

The system dynamic range was measured at 3GHz as shown in Figure 5.5, where an

external attenuator was used to decrease the receiver's input power level. The base-band

I/Q signals were then sampled and transformed to a synthetic pulse. The attenuation level

was increased from 25dB upwards, which accounts for the transmission loss, until the

synthetic pulse was below 10dB SNR, which occurred at a level of 105dB. Therefore, the

actual system performance factor and the system's dynamic range were found to be 105dB

and 80dB, respectively. The measured system dynamic range was slightly lower than the

expected system dynamic range of 86dB. The difference was mainly caused by the total gain

deviation of 5dB at 3GHz. Table 5.3 shows other electrical characteristics and control parameters of the microwave SFCW radar sensor system.
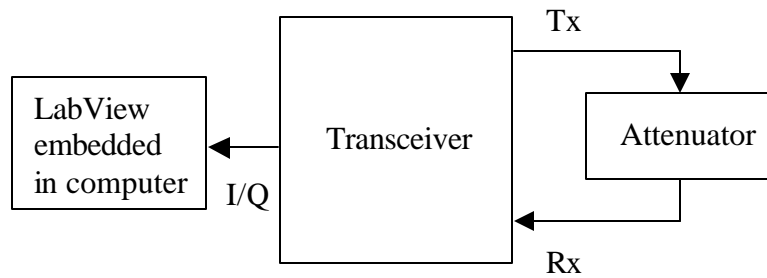
Figure 5.5 Set-up for measuring the system dynamic range of the system.

Table 5.3 Other measured electrical characteristics and the control parameters of the system.

Electrical characteristics		Control parameters	
DR_s	80dB	Freq. step Δf	10MHz
SF_a (at 3GHz)	105dB	Number of freq. steps	500
DC Power consumption	2.9W	PRI	100ms
P_{1dB}	-4dBm	ADC sampling freq.	1KHz

5.1.2 Millimeter-Wave SFCW Radar Sensor System

The transmission gain G_T of the high frequency circuit block of the transmitter was measured in between the IF input and TX output ports within 27-36GHz. Figure 5.6 shows that the measured transmission gains were deviated 4.2-5.7dB from the designed transmission gain of 10dB at 32GHz as shown in Table 4.2 in Chapter IV. The deviation was mainly caused by losses of bonding wires, connectors, and components.

Figure 5.6 The measured transmission gain of the high frequency circuit's block of the transmitter.

Then, the output power level for each component of the low frequency circuit portion of the transmitter was measured after two attenuators adjusted the measured PLL oscillator

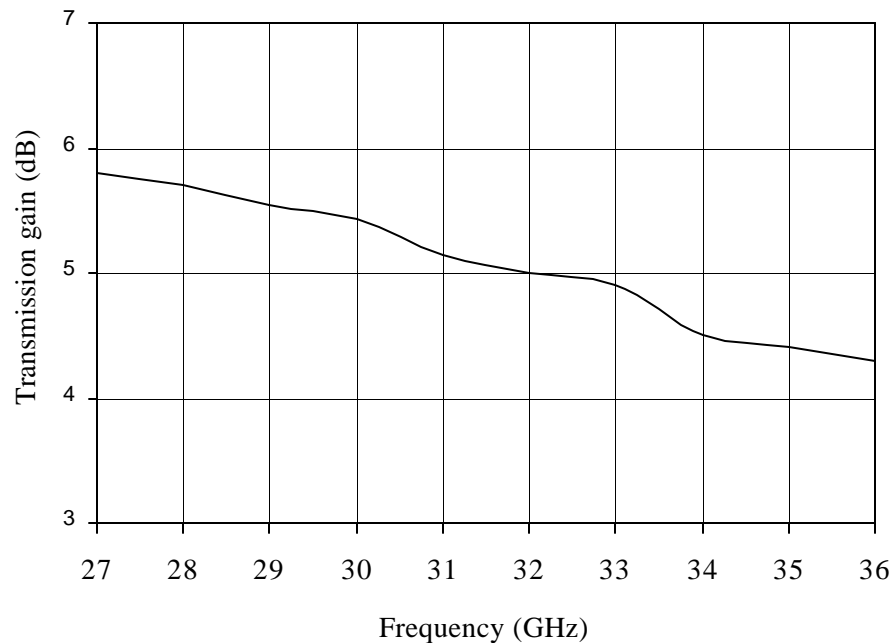power of 5.5dBm to the desired specifications; viz. 0dBm at the splitter output that is fed to the LO amplifier, and –0.5dBm at the IF output. Table 5.4 shows the measured output power at each component of the transmitter where the measured transmitter output was in the range of 3.8-5.3dBm.

Table 5.4 Measured output power at each component of the transmitter.

	Gain	Loss	Pout	G_T
PLL osc.			4.5dBm	
Attenuator		0 dB	4dBm	-0.5dB
LPF		0.5dB	3.5dBm	-0.5dB
Spliter		3.5dB	0dBm	-3.5dB
Attenuator		0dB	-0.5dBm	-1.5dB
Up-converter		N/A	N/A	
Amplifier	N/A		N/A	4.3-5.8dB
Amplifier	N/A		3.8-5.3dBm	
Total	N/A	N/A	-	-1.7 to -0.2dB

Similarly, the transmission gain of the high frequency circuit block of the receiver was measured in between the Rx input and IF output ports within 27-36GHz. Figure 5.7 shows that the measured transmission gains were deviated 2.8-3.8dB from the designed

transmission gain of -1dB at 32GHz, as shown in the Table 4.1 in Chapter IV. These errors were caused by similar reasons as those of the transmitter.
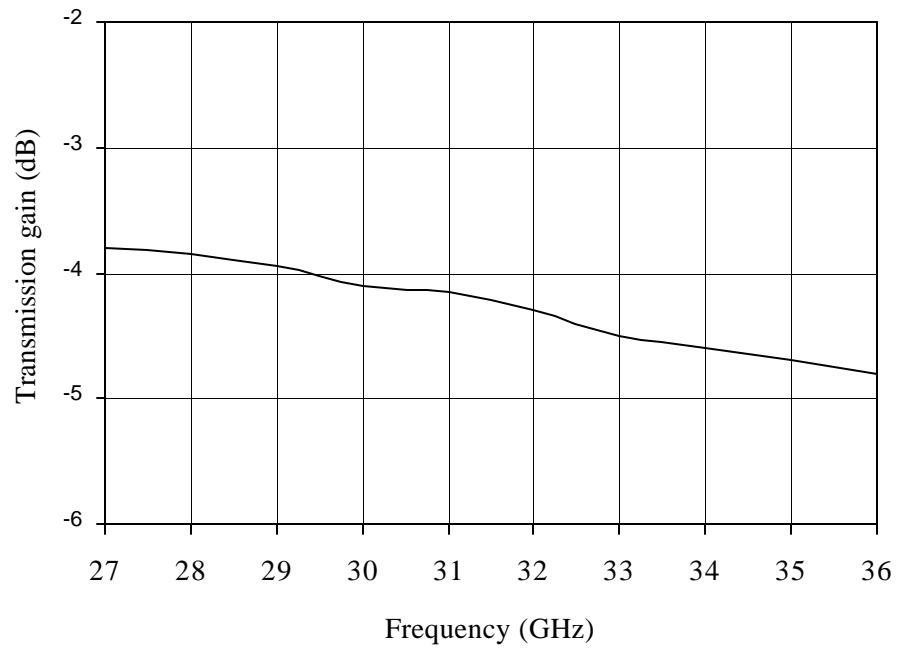
Figure 5.7 The measured transmission gain of the high frequency circuit's block of the receiver.

Figure 5.8 shows the linearity of the high frequency circuit block of the receiver. The measured input 1dB compression point of the high frequency circuit block was -6dBm at 32GHz.
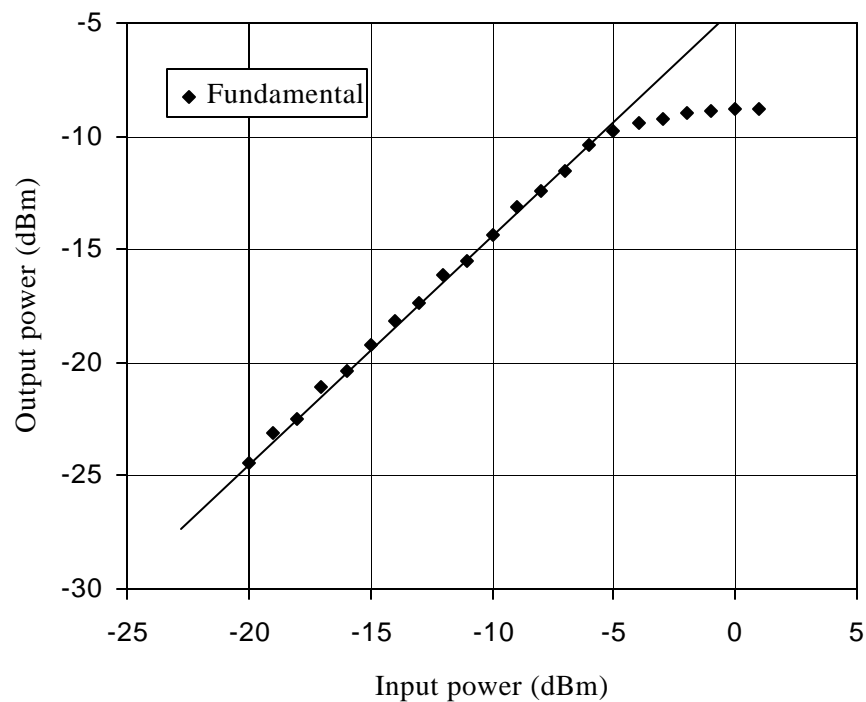

Figure 5.8 Linearity of the high frequency circuit's block of the receiver at 32GHz.

The video amplifier increased the maximum output power (= -10dBm) of the quadrature detector to meet the ADC's maximum input range (= 9dBm). Table 5.5 represents the measured receiver electrical characteristics.

Table 5.5 Measured output power of the receiver where the input power was in the range of –9.2 to –7.7dBm.

	Gain(Vo/Vi)	Loss	Pout	G_T
LNA	N/a	N/A	N/A	-4.8 to -3.8dB
Down-conv.		N/A	-14 to –11.5dBm	
LPF		0.5dB	-14.5 to -12dBm	-0.5dB
Amplifier	12dB		-3.5 to -1dBm	11dB
I/Q mixer		8.5dB	-12.5 to –10dBm	-9dB
LPF(Ro=200)		0.2dB	-18.7 to –16.2dBm	-6.2dB
Amp.(Ro=1k)	32.2dB		6.5 to 9dBm	25.2dB
Total	N/A	N/A	-	15.7to 16.7dB

The system dynamic range was not measured, as the wide range of external attenuator was not available in the laboratory. However, it was assumed to be 76dB from the measured dynamic range value of the microwave SFCW radar sensor system, as the process gain is 1dB lower than the microwave SFCW radar sensor system and gain deviation is 3dB worse than the corresponding values of the microwave SFCW radar sensor system. From the above assumed value of the system dynamic range, the actual system

performance factor was calculated as 89dB (= 76dB+13dB). Table 5.6 shows other electrical characteristic and control parameters.

Table 5.6 Other measured electrical characteristics and the control parameters of the system.

Electrical characteristics		Control parameters	
DR_s	76dB	Freq. step Δf	10MHz
SF_a (at 32GHz)	89dB	Number of freq. steps	400
DC Power consumption	2.6W	PRI	100ms
P_{1dB}	-6dBm	ADC sampling freq.	1KHz

5.2 Tests with the Millimeter-Wave SFCW Radar Sensor System

The assumptions implicit in course of measurements are as follows. Firstly, the targets or objects were homogeneous materials with relatively low loss. Secondly, the incident waves were TEM plane waves. Thirdly, the double reflected waves in a layer were ignored. Lastly, the loss of dry sand at Ka-band was simply estimated from those values at 0.1 and 1 GHz presented in [31]. These assumptions may cause significant discrepancy between the actual penetration depth and the estimated one; however, the main purpose of the test was to verify its feasibility as a subsurface radar sensor and hence further investigation in this direction was not pursued.

5.2.1 Measurement of the Surface Profiling

This measurement involves profiling the surface of a sample where the surface abruptly changes in height. A plastic sample (20 in. × 6 in.) was used for measuring the surface profile. The sensor's antenna was pointed directly onto the surface of the sample without contact while the sample was moving in the x direction as in Figure 5.9. The measured data was collected every 0.2 inches along the direction of movement. Figure 5.10 shows the reconstructed profile, obtained from the measurements, of the sample along with the actual profile. The reconstructed profile agrees well with the actual profile of the sample with less than ± 0.04-inch error in height except near the edges, at which the actual surface profile abruptly changes.

In order to find the lateral resolution, we estimated a minimum cross-range that can be detectable with this sensor from the reconstructed profile. The minimum cross-range is given by subtracting B from A, as shown in Figure 5.10, as the distance of B-A is constant at a particular height, which means that the sensor can reconstruct the bottom surface when B is greater than 0. The estimated minimum detectable cross-range, R_{c_min}, of 1 inches also agrees well with the lateral resolution of 0.92 inches, obtained theoretically for the range R of 3.5 inches with the aid of equation (3.22) in Chapter III. Consequently, the reconstructed profile was quite comparable to the actual profile (Figure 5.10). The measurement results showed that the sensor has a lateral resolution of 1 inches and a good accuracy with less than ± 0.04-inch error, except near the edges, at which a sudden change of the height occurs.
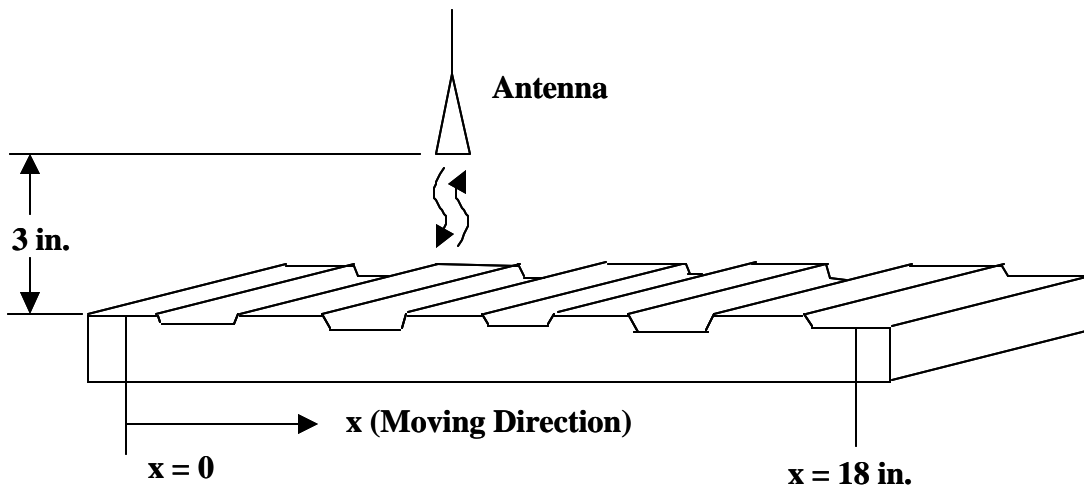
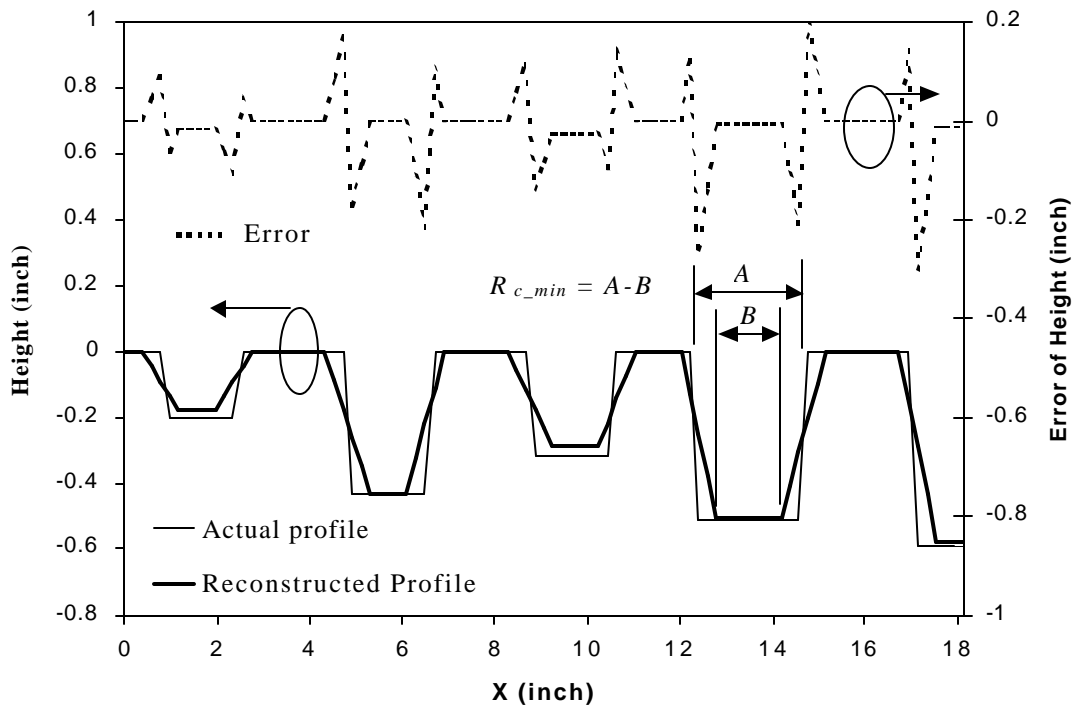Figure 5.9 The set up for measuring of the surface profile.

Figure 5.10 Reconstructed and actual profiles of the surface of the sample in Figure 5.9,

where the height is set to 0 at the top surface at $x = 0$.

5.2.2 Measurement of Liquid Level

This procedure monitors the continuously varying liquid level in a tank. As shown in Figure 5.11, liquid level in a tank was measured with the SFCW sensor. The level of liquid was decreased from a reference level, an initially set value of 0, to 3 inches below the reference and the resulting changes were measured. The measured results were very close to the actual liquid level in the tank with less than ±0.04-inch error as shown in Figure 5.12 (where the negative sign (-) means below the reference level).

According to the above two measurements, the sensor achieved a good range accuracy with less than ± 0.04-inch error, which agrees very well with the theoretical error of ± 0.036 inches, obtained from equation (3.16) in Chapter III, where the frequency step and the number of steps were 20MHz and 4096 points, respectively. Also, a lateral resolution of 1-inch was obtained, which agrees quite well with the theoretical lateral resolution of 0.72-0.92 inches. In addition, the sensor can promise very accurate measurement of vertical displacement of the liquid level with less than a ± 0.04-inch error.
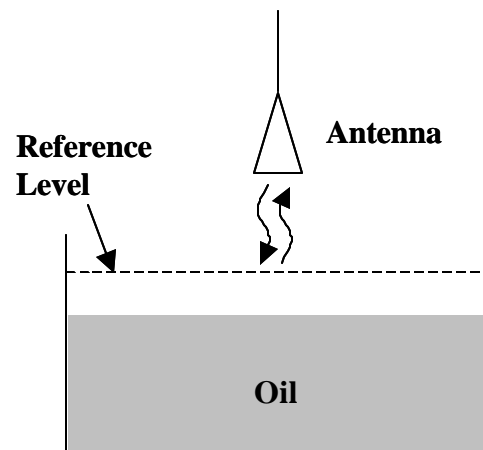
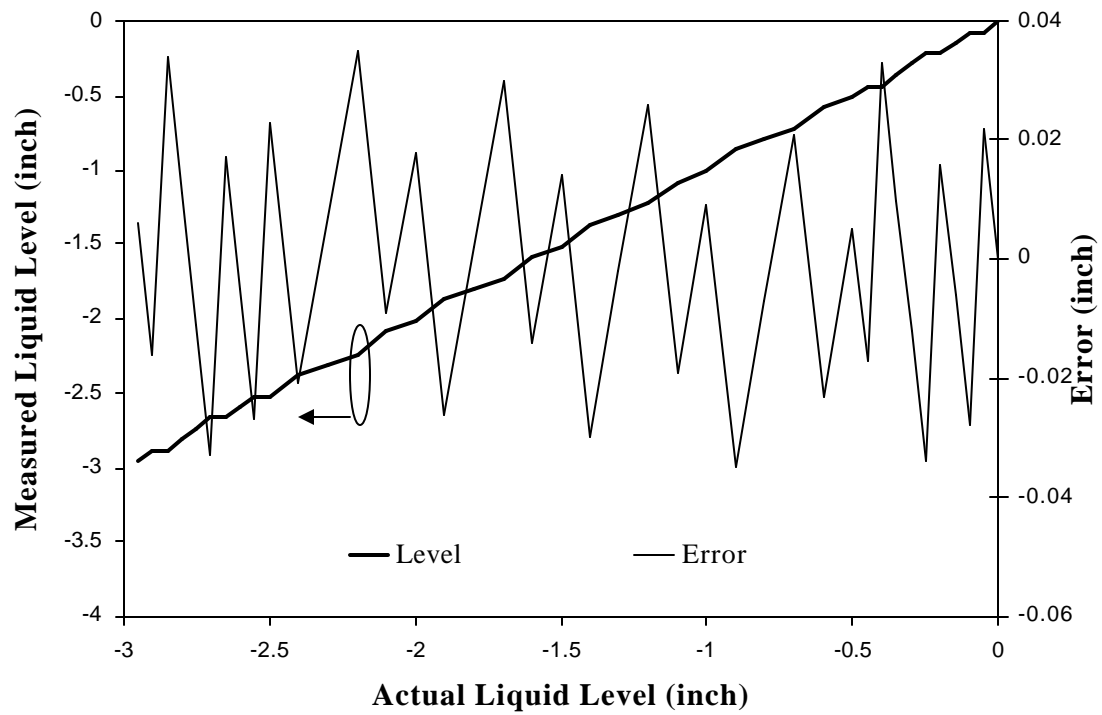Figure 5.11 The set up for monitoring the liquid level in a tank.

Figure 5.12 Measured and actual liquid level in the tank in Figure 5.11.

5.2.3 Measurement of Buried Mines

To demonstrate possible usage in applications for mine detection, three different Anti-personnel (AP) metal mines were used as shown in Figure 5.13. The purpose of the measurement was to localize and detect AP mines buried under a sandy surface.

The first named AP1 is spherical in shape, 2.5 inches in diameter, buried at 2 inches depth (d1) and displaced 7 inches horizontally (h1) from the edge of the container, another named AP2 is cylindrical in shape, 5 inches in diameter and 2.5 inches high, buried at 6 inches of depth (d2) and displaced 15 inches horizontally (h2), and a final one named AP3 is cylindrical in shape, 2.2 inches in diameter and 3.5 inches high, buried at 0.75 inches under the surface (d2) and 23 inches in horizontal displacement(h3).

A metal plate (0.04m^2) was first placed 10 inches under the surface of sand and measurements were performed to find its depth by using equation (3.15), which does not consider the effect of the propagation medium. The measured depth of the metal plate was 16.7 inches, which is longer than the actual depth as the dielectric medium was not considered. From the measured result of the metal plate, the calculated depth d in sand can be found using a proportional expression described as

$$d = \frac{10d_m}{16.7} \qquad\qquad 5.1$$

where d_m is the measured depth by using equation (3.15) and d is the calculated depth in sand.

The depths (d1, d2, and d3) and horizontal displacements (h1, h2, and h3) of the AP mines were measured with the antenna moving in the horizontal direction as shown in Figure 5.13. From equation (3.15), the measured depths of AP1, AP2, and AP3 mines were recorded as 3.39, 10.09 and 1.33 inches, respectively. Therefore, the calculated depths of AP1, AP2, and AP3 mines in sand were found at 2.05, 6.08 and 0.8 inches as shown in Figure 5.14, which shows synthetic pulses corresponding to each AP mine. The measured horizontal displacements of AP1, AP2, and AP3 mines were 7, 15.75, and 23.25 inches, respectively. Figure 5.15 shows the detected and localized mines. The results show that the measured horizontal displacements and depths of AP mines are fairly close to the corresponding actual horizontal displacements and depths with less than 0.75 and 0.08 inches of error.

Note that the AP3 mine buried at only 0.75 inches under the top surface was clearly detected and localized with the aid of the theoretical range resolution equation (eqn. 3.18) as 0.59 inches. As a result, the sensor has demonstrated its ability in detecting and locating AP mines of very small sizes with a competitively high resolution.
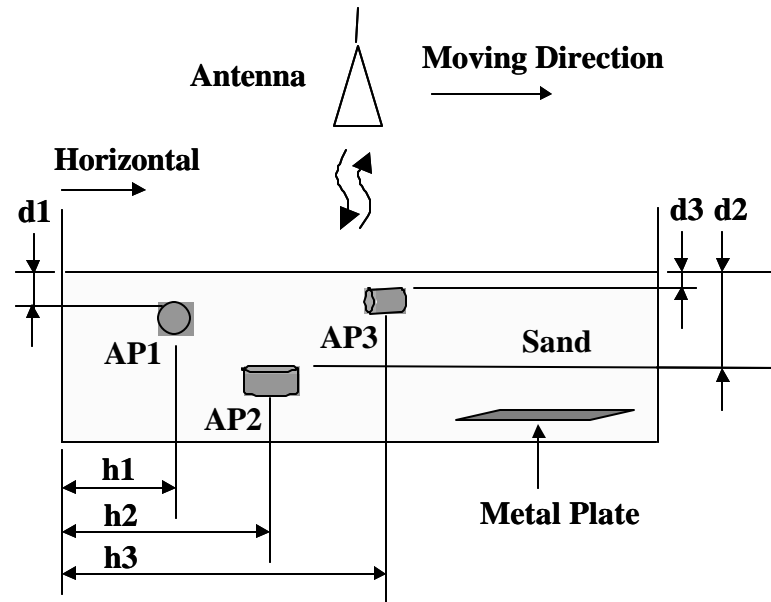
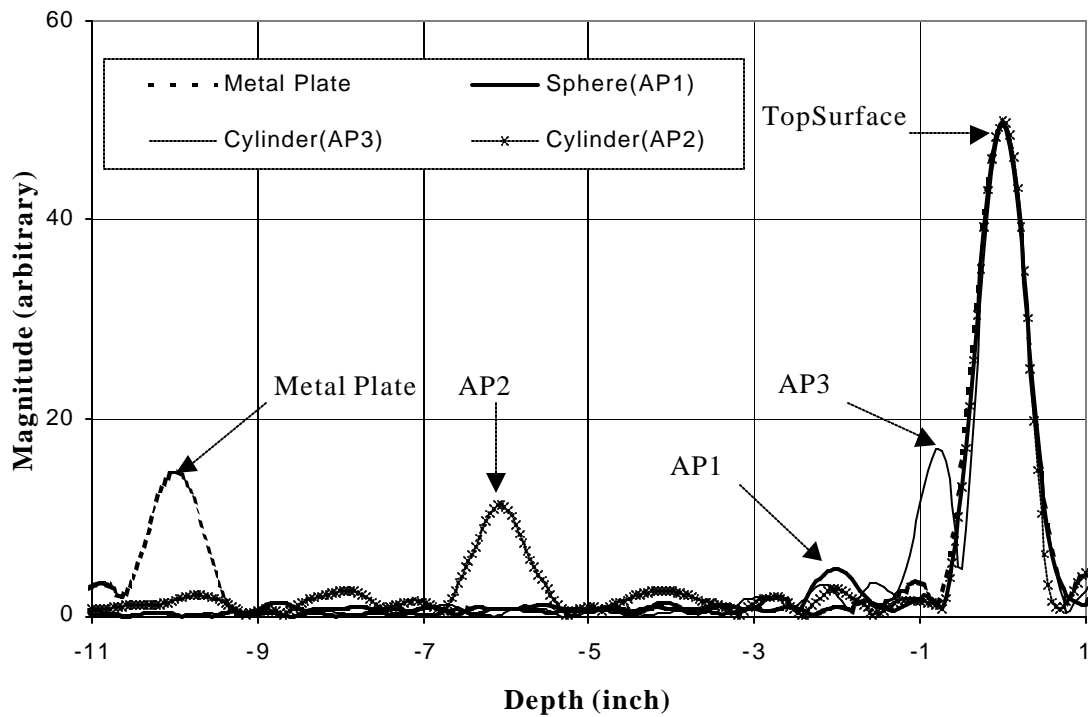Figure 5.13 The set up for detecting AP mines buried in sand.

Figure 5.14 Synthetic pulses extracted from measurements of AP mines in Figure 5.13.
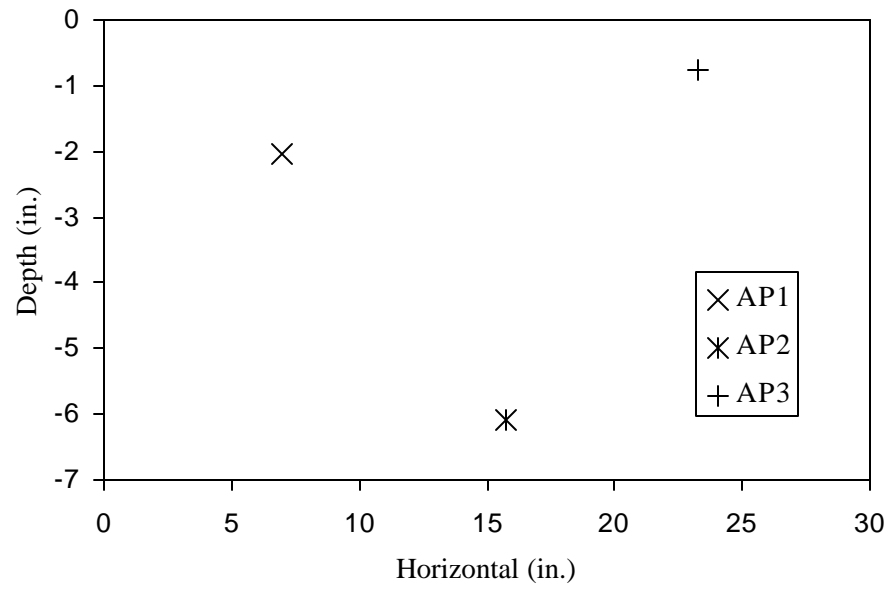
Figure 5.15 AP mines localized in depth and horizontal displacement.

5.3 Tests with the Microwave SFCW Radar Sensor System

Two measurements on the microwave SFCW radar sensor prototype were performed to verify its feasibility as a subsurface radar sensor; one is conducted on a sample pavement provided by TTI for laboratory experimentation and the other on an actual road, as well as at a test site in the Riverside Campus area of Texas A&M University.

The assumptions applied on all measurements are listed as follows: Firstly, it was assumed that the targets or objects were homogeneous materials with low loss. Secondly, the incident waves were assumed as plane waves. Thirdly, the multiple-reflected waves in a layer were ignored as mentioned in Chapter II. Lastly, the layers were taken to be smooth half-spaces. In fact, these assumptions are not correct for practical pavement materials. However, as will be seen later, accurate measured results have been achieved for a practical pavement sample.

5.3.1 Measurements on the Sample Pavement

A pavement sample was constructed with two layers in a wooden box of 36 in. x 36 in. The top layer is asphalt having a thickness of 2.6-2.7 inches while the bottom layer is base with a thickness of 4.1 inches and filled with limestone. The sensor's antennae were pointed obliquely onto the sample surface with a parallel polarization and 10 degrees of incident angle at 3GHz through the air at 0.2 m of stand-off distance.

As shown in Chapters II and III, 10 degrees of incident angle was not much and had little affect on the reflection and transmission coefficients, as well as the penetration depth,

therefore it was ignored. Figure 5.16 illustrates the signals reflected at the interfaces between the sample's layers.
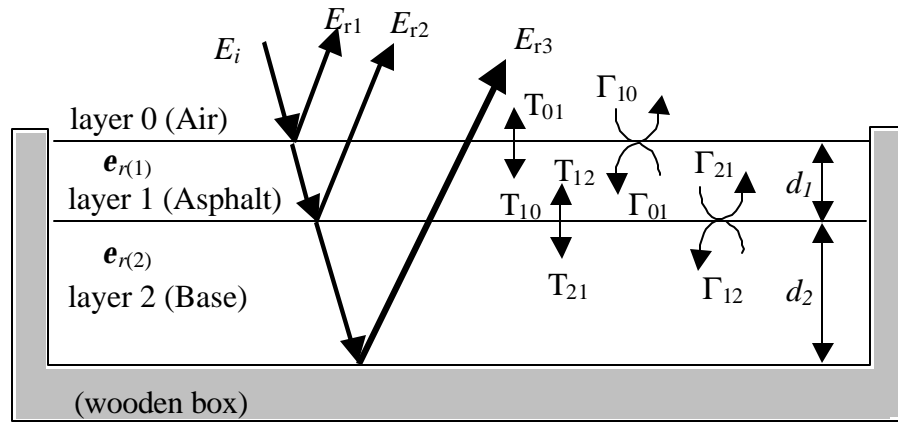
Figure 5.16 Sketch of the pavement sample in a wooden box together with the incident and reflected waves. E_i is the incident wave; E_{r1}, E_{r2} and E_{r3} are the reflected waves at the interfaces between layers 0 and 1, layers 1 and 2, and layer 2 and the wooden box, respectively, and d_1 and d_2 are the thickness of the layers 1 and 2, respectively.

With reference to Figure 5.16, the single reflected field at the 2nd interface in Chapter II, resulting in equation (2.24b), repeated here with a normally incident wave, is given as under:

$$E_{r2} = E_i T_{10} T_{01} \Gamma_{21} \exp\left(-a_1 d_1\right) \qquad 5.2$$

where E_i represents the incident wave.

Then, the relative dielectric constant $e_{r(i+1)}$ of layer $i+1$ ($i = 0, 1, 2$) can be derived from equation (2.20), when a plane wave is incident transversely from layer i to layer $i+1$:

$$e'_{r(i+1)} = e'_{r(i)} \left(\frac{1 - \Gamma_{i+1i}}{1 + \Gamma_{i+1i}} \right)^2$$

5.3

where $e'_{r(i)}$ is the real part of the relative dielectric permittivity of layer i and Γ_{i+1i} indicates the reflection coefficient of the wave incidents from layer i to layer $i+1$.

From equations (2.18) and (2.25) in Chapter II, the single reflected field from the nth interface is found as

$$|E_{rn}| = |E_i| |\Gamma_{nn-1}| \left(\prod_{m=1}^{n-1} T_{mm-1} T_{m-1m} \exp(-2a_m d_m) \right)$$

5.4

where a_m and d_m are the attenuation constant and thickness of the layer m.

With assuming $\Gamma_{10} = -1$, the reflected field E_m from the metal plate is equal to the incident field E_i when a metal plate is placed at the first interface, which results in

$$|E_m| = |E_i|$$

5.5

The reflection coefficient at the first and second interfaces are then obtained from equations (5.4) and (5.5) as

$$\Gamma_{10} = \frac{|E_{r1}|}{|E_m|}$$

5.6

and

$$\Gamma_{21} = \frac{|E_{r2}|}{|E_m|\mathrm{T}_{10}\,\mathrm{T}_{01}\,\exp(-2\boldsymbol{a}_1 d_1)}$$ 5.7

.

where E_{r2} represents the single reflected field at the 2nd interface.

Using equations (5.4) and (5.7), the relative dielectric constants of the asphalt and base layers can be calculated as

$$\boldsymbol{e}'_{r(1)} = \left(\frac{1-\Gamma_{10}}{1+\Gamma_{10}}\right)^2$$ 5.8a

and

$$\boldsymbol{e}'_{r(2)} = \boldsymbol{e}'_{r(1)}\left(\frac{1-\Gamma_{21}}{1+\Gamma_{21}}\right)^2$$ 5.8b

In addition, the thickness of layer i can be derived from equation (3.15) in Chapter III as

$$d_i = \frac{c\Delta n_{(i,i+1)}}{2M\Delta f\,\sqrt{\boldsymbol{e}'_{r(i)}}}$$ 5.9

where $\Delta n_{(i,i+1)}$ is the difference between the bin numbers of cells corresponding to layers i and $i+1$ as shown in Figure 5.17. It should be mentioned here that this procedure can also be applied to structures containing more than 3 layers.

Figure 5.17 represents the synthetic range profile of the pavement sample and a metal plate obtained from the measurement data. Table 5.7 shows the measured parameters of the pavement sample along with the actual values. The measured thickness of each layer agrees well with the actual values. Note that the theoretical relative dielectric constants of the sample's asphalt and base materials, in Table 2.1 in Chapter II, were not used here since 1)

the reported values vary over a wide range as in Table 2.1 which is provide by TTI and 2)

the reported asphalt and base materials are not the same as those in our pavement sample.
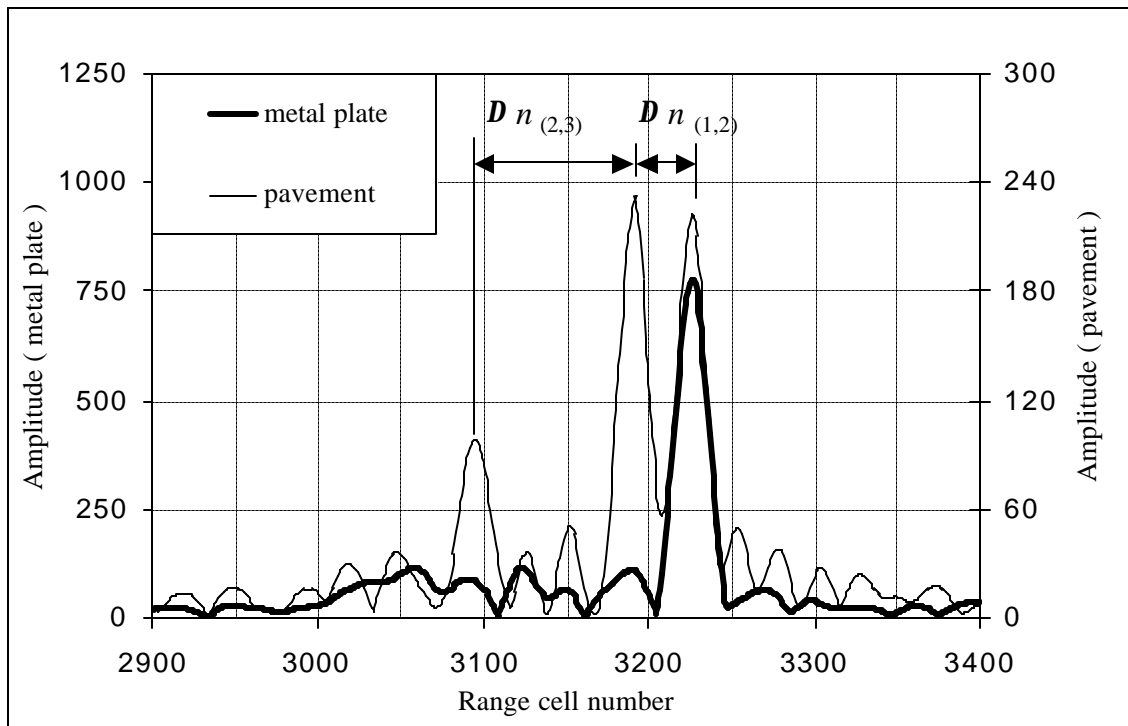

Figure 5.17 Synthetic range profiles obtained from a metal-plate target and the pavement
sample.

Table 5.7 Comparison between actual and measured data.

		Asphalt	Base
Relative dielectric constant	Experiment	3.24	12.5
Thickness (inches)	Actual	2.6-2.7	4.1
	Experiment	2.72	4.04

5.3.2 Measurements on the Test Site and Actual Road

The measurements were also conducted at two sites on the Riverside Campus of Texas A&M University. As discussed earlier, only stationary tests were performed due to the low *PRI* of the synthesizer.

The first measurement was conducted on the test site that was partitioned with several sections in which there are pavement layers with various thicknesses as shown in Table 5.8. However, the actual thickness and other properties should be different with those values in Table 5.8 as the test site was constructed 30 years ago. The second measurement on the road named as Rut Ride was performed where the thickness of the asphalt layer is fixed at 2 inches while the thickness of the base layer is varied continuously as shown in Figure 5.18. The measurement data was collected every 20 feet for a total length of 100 feet.

Figures 5.3.19-22 show the synthetic profiles of sections A-D. As shown in Figures 5.3.19-22, this sensor system detected up to the second interface between the asphalt and

base layers at the section A, B, and C and up to the third interface between the base and subgrade layers at the section D, where the thickness of the asphalt layer is only one inch. The measured thickness of the asphalt and base layers was found, as shown in Table 5.8, using equations (5.6-9).

Figure 5.23 (a-f) represents the synthetic profiles obtained at different positions of the road as shown in Figure 5.18. As expected from the previous measurement results, it only detected the second interface between the asphalt and base layers. The measured thickness of the asphalt layer, as shown in Table 5.9, showed less than 0.25 inches of error compared to the actual thickness of the asphalt layer.

From the measured results, it can be deduced that the transmitted power was rapidly decreased in the layers due to significant loss at high frequencies. However, it demonstrated that this sensor could clearly detect as least 5 inches of the thickness of the asphalt layer.

Table 5.8 Thickness and material of each section where x, y, and z are limestone, limestone + 2% lime, and limestone + 4% cement, respectively.

Section	Thickness (inches)/material				
	Asphalt		Base		Subgrade
	Actual	Measured	Actual	Measured	Actual
A	5	4.68	4/z	N/A	4/x
B	5	4.82	4/z	N/A	4/z
C	3	3.12	8/y	N/A	8/y
D	1	0.99	4/y	3.96	12/x

z = 0   z = 100

2 in.   Asphalt εr ≈ 6

6 in.   Base εr ≈ 13   14 in.
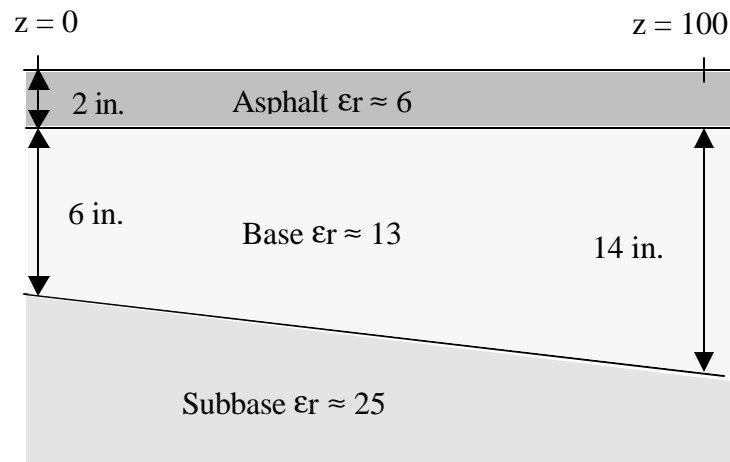
Subbase εr ≈ 25

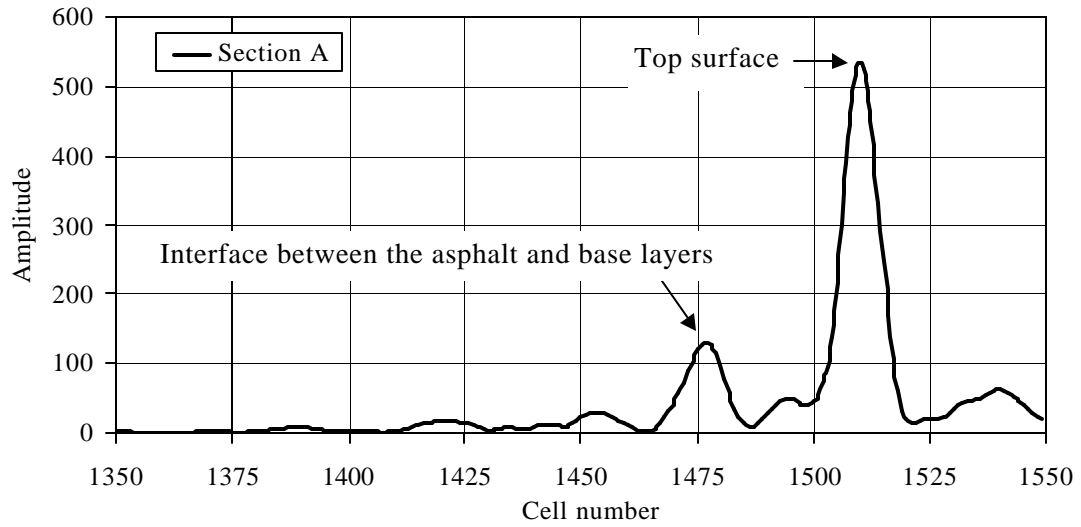Figure 5.18 Cross-section of the road.

Figure 5.19 Synthetic profile of section A.
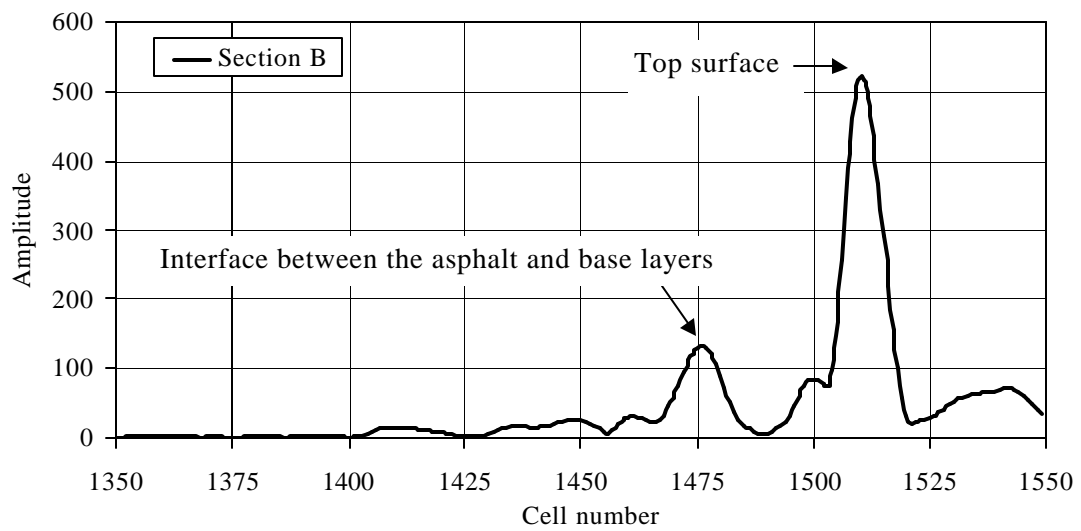
Figure 5.20 Synthetic profile of section B.
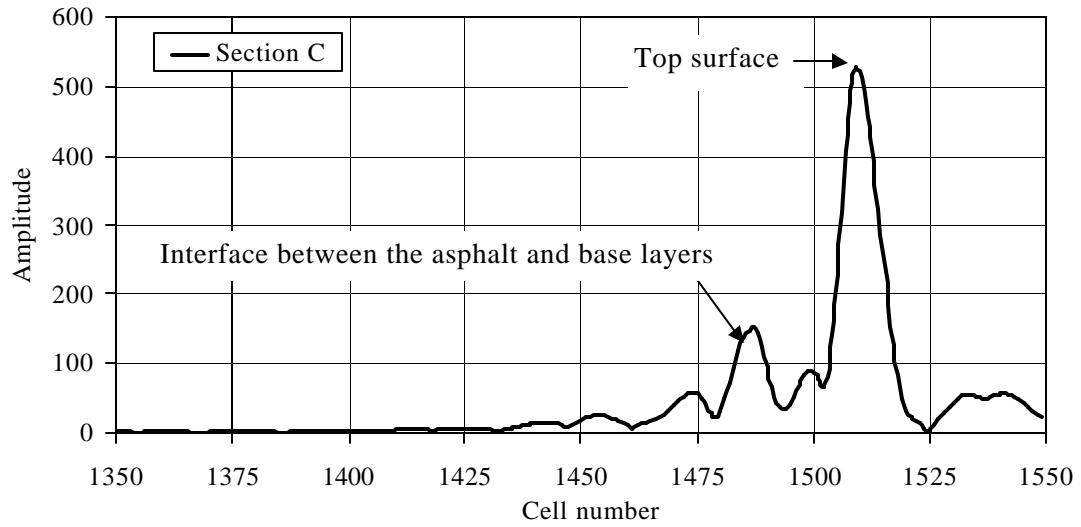
Figure 5.21 Synthetic profile of section C.

Figure 5.22 Synthetic profile of section D.

Table 5.9 Comparison between actual and measured data.

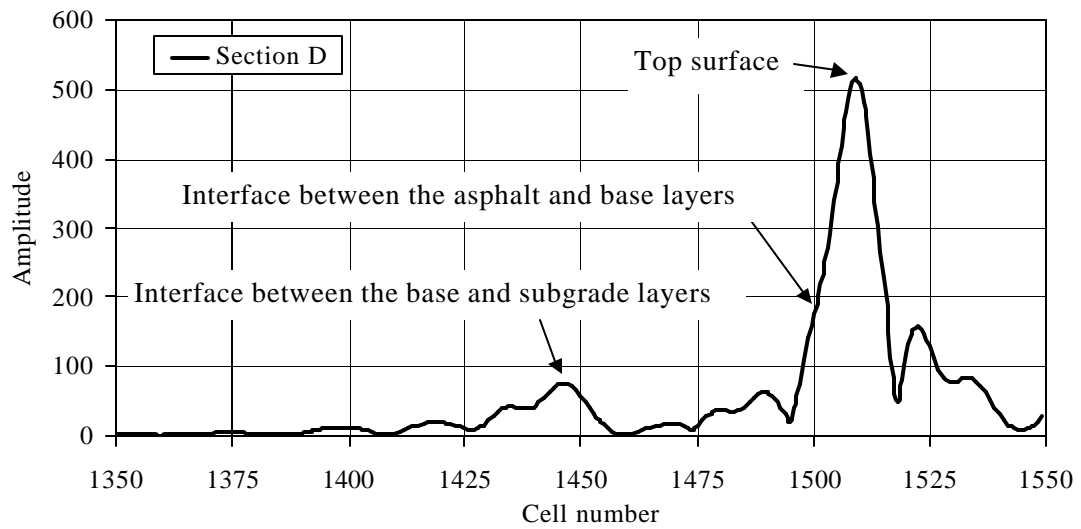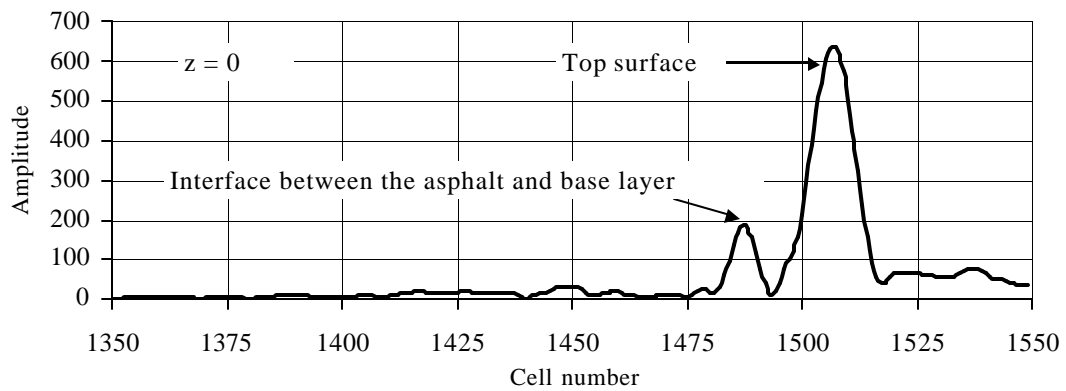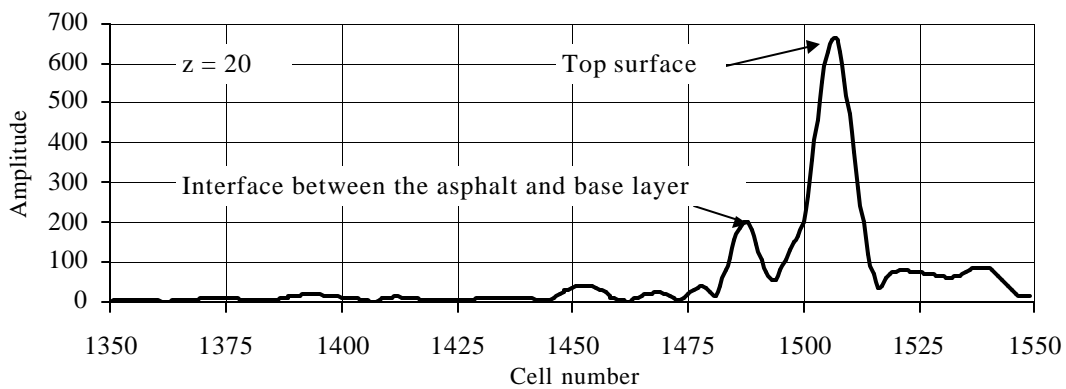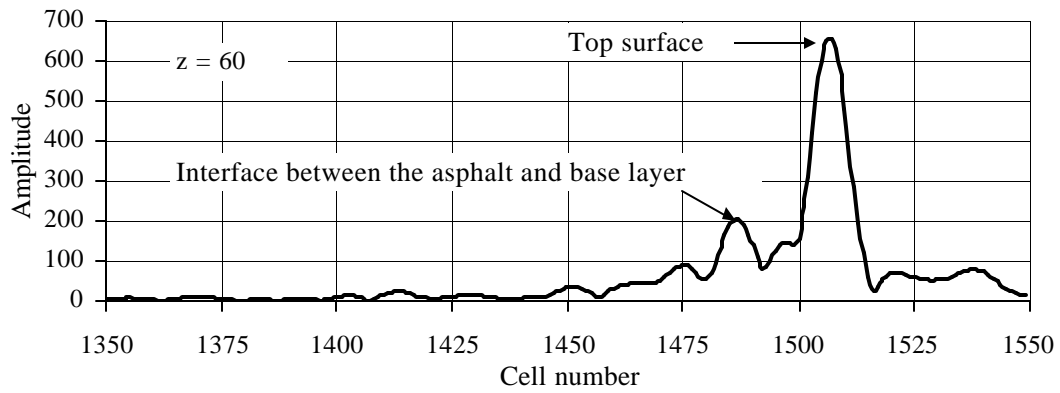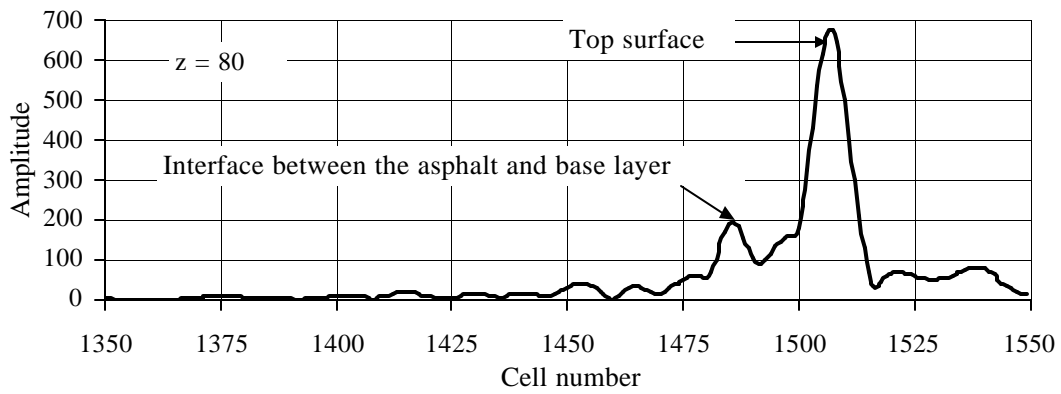| Position	z(feet)	0	20	40	60	80	100
Thickness	Actual	2	2	2	2	2	2
	Measured	2.13	2.13	2.13	2.25	2.25	2.25

(a)

(b)
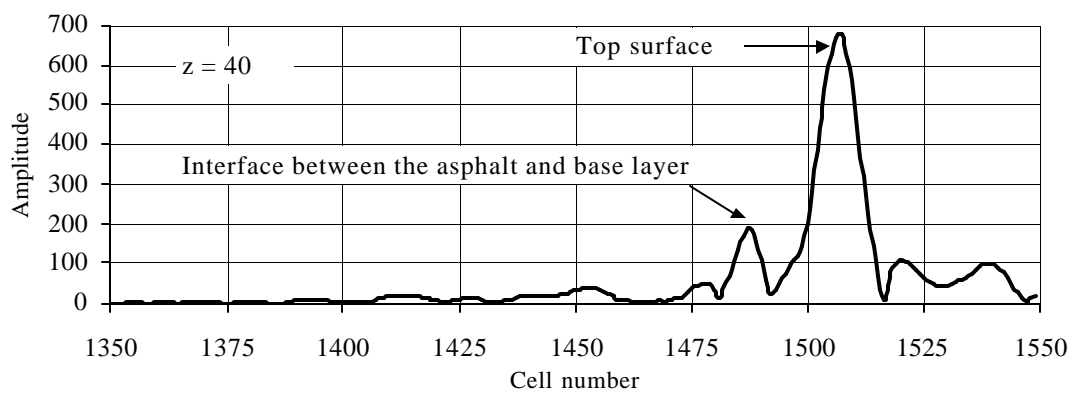
(c)

(d)

(e)
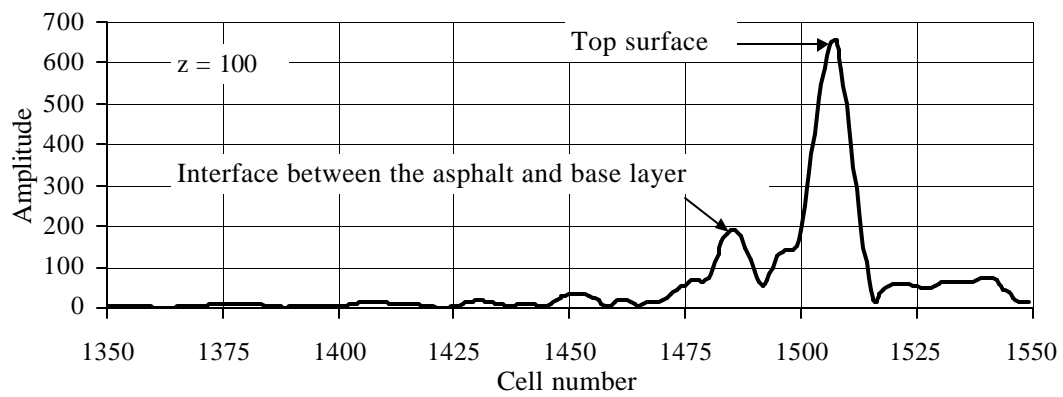
(f)

Figure 5.23 Synthetic profile of the road in Figure 5.18.

CHAPTER VI

CONCLUSIONS

Two new mircrowave and millimeter-wave integrated-circuit SFCW radar sensor systems, having high resolution and good accuracy, have been developed.

A set of modified radar equations that accurately characterize any subsurface radar sensor intended to investigate multi-layered structures, such as the pavements consisting of the asphalt, base, and several subgrade layers or to detect and localize buried object under the surface, were derived. These equations involved a larger than usual number of parameters that subsurface radar sensors require to estimate their penetration depth.

The system performance factor that was incorporated in the radar equation was renamed "actual system performance factor", to better characterize the SFCW radar sensor system. Along with this term, the radar equations enabled the estimation of the maximum penetration depth of the SFCW radar sensor for buried objects under ground and also for pavement layers. A term called "range accuracy" was coined in the course of the dissertation work and was used for accurately measuring the vertical range of a target, and also for estimating a varying liquid level.

The microwave SFCW radar sensor's transceiver, operating in the 0.6-5.6GHz range and based on a coherent super-heterodyne scheme, was realized using MICs on FR-4 substrates, which resulting in a low cost, light weight and small size implementation of the transceiver.

Also, a millimeter-wave SFCW radar sensor's transceiver, employing a coherent super-heterodyne architecture, was developed with both MICs and MMICs on FR-4 and alumia substrates with an 8GHz operational bandwidth.

A UWB microstrip quasi-horn antenna for the microwave SFCW radar sensor system, realized with low cost and light weight, was also developed and demonstrated its excellent properties with better than 10dB of return loss and 6-17dBi of directional gain in the desired UWB range of frequency. It was found that an extra resistive load and pieces of absorbers could improve the return loss caused at the open end of the antenna significantly.

A Ka-band microstrip quasi-horn antenna was also developed for potential usage in millimeter-wave SFCW radar sensor systems. It demonstrated excellent properties in the 20-40GHz with greater than 14 dB of the return loss and 14-17 dBi of directional gain.

An innovatively simple yet effective technique for compensating the common I/Q errors caused by the system itself was demonstrated and applied to the signal processing, and some other blocks for acquisition and storage of I/Q data.

The microwave SFCW radar sensor's transceiver was incorporated in a system along with UWB antennae and a signal processing block and tested meticulously to verify its electrical performance. The measured actual system performance factor was 105dB.

Tests of the millimeter-wave SFCW radar sensor's transceiver were also performed. It was incorporated with a waveguide horn antenna and the system was re-tested. Its actual system performance factor was found to be 89dB.

Measurements using these sensor systems were conducted on various samples as well as on actual roads. The microwave SFCW radar sensor system demonstrated its excellent performance with great measurement results on the sample pavement with less than ± 0.1 inches of error. It also showed that the thickness of the asphalt layer on the actual road could be accurately measured less than 025 inches of error.

The millimeter-wave SFCW radar sensor system also demonstrated its benefits as a surface and subsurface radar sensor. Its feasibility as a subsurface radar sensor was verified by testing it for detecting and localizing very small buried AP mines under sand with less than 0.75 inches of vertical resolution. As a surface radar sensor, it profiled the surface of a sample whose height rapidly changes along the horizontal direction, with 1 inches of lateral resolution and less than ± 0.04 inches of range accuracy. In addition, it accurately measured the displacement of liquid level with less than ± 0.04 inches of discrepancy.

6.1 Recommended Future Work

The following are some of the recommendations that could be suggested on the basis of the experiences gained during the course of this project:

1. Advanced image processing such as SAR technique is needed to increase its lateral resolution for better localizing buried objects or finer profiling a rough surface.

2. Compensation for dispersion of the propagation media by using signal processing is needed to enhance its synthetic pulse shape resulting in higher vertical resolution.

3. The transmitting power needs to be increased to penetrate much further in depth.

4. A fast frequency synthesizer needs to be incorporated with the sensor systems for measurements on a moving vehicle. For instance, the sweep time of the frequency synthesizer needs to be 25ms if the speed of the vehicle is 20 miles per hour.

REFERENCES

[1]   D. J. Daniels, D. J. Gunton and H. F. Scott, "Introduction to subsurface radar," *IEE Proc.* vol. 135, pp. 278-320, Aug. 1988.

[2]   S. L. Earp, E. S. Hughes, T. J. Elkins and R. Vikers, "Ultra-wideband ground-penetrating radar for the detection of buried metallic mines," *IEEE Aerospace and Electronic Systems Magazine*, vol. 11, pp. 30-39, Sep. 1996.

[3]   A. Langman and M. R. Inggs, "A 1-2GHz SFCW radar for landmine detection," *in Proc. of the 1998 South African Symposium.*, pp. 453-454, Sep. 1998.

[4]   C. J. Vaughan, "Ground-penetrating radar surveys used in archaeological investigations," *Geophysics*, vol. 51, no. 3, pp. 595-604, Mar. 1986.

[5]   J. Otto, "Radar applications in level measurement, distance measurement and nondestructive material testing," *in Proc. of the 27th European Microwave Conference and Exhibition*, vol. 2, pp 1113-1121, Sep. 1997.

[6]   T. Lasri, B. Dujardin and Y. Leroy, "Microwave sensor for moisture measurements in solid materials," *Microwaves, Antennas and Propagation*, vol. 138, pp. 481-483, Oct. 1991.

[7]   T. Scullion, S. Servos, J. E. Ragsdale and T. P. Saarentento, "Application of ground-coupled GPR to pavement evaluation," TTI Report #2947-S, Texas Transportation Institute, College Station, TX, 1997.

[8]   J. Lee, "Design of high-frequency pulse subsurface penetrating radar for pavement assessment," Ph.D. Dissertation, Texas A&M Univ., College Station, TX, 2000.

[9]   A. P. Annan and J. L. Davis, "Radar range analysis for geological materials," *Geological Survey of Canada*, no. 77-1B, pp. 117-124, 1977.

[10]   D. A. Ellerbruch and D.R. Belsher, "Electromagnetic technique of measuring coal layer thickness,"*IEEE Trans. on Geoscience Electronics*, vol.16, no. 2, pp. 126-133, Apr. 1978.

[11]   E. K. Miller, *Time-domain measurements in electromagnetics*, New York, NY, Van Nostrand Reinhold Company, 1986.

[12]   C. H. Lee, "Picosecond optics and microwave technology," *IEEE Trans. Microwave Theory Tech.*, vol. 38, pp. 569-607, May 1990.

[13]   L. L. Molina, A. Mar, F. J. Zutavern, G. M. Loubriel and M. W. O'Malley, "Sub-nanosecond avalanche transistor drivers for low impedance pulsed power applications," *in Pulsed Power Plasma Science-2001*, vol. 1, pp. 178-181, June 2001.

[14]   J. S. Lee and C. Nguyen, "Uniplanar picosecond pulse generator using step-recovery diode," *Electronics Letters*, vol. 37, pp. 504-506, Apr. 2001.

[15]   P. Dennis and S.E Gibbs, "Solid-state linear FM/CW radar systems-their promise and their problems," *in IEEE MTT-S International Microwave Symposium Digest*, vol. 74, no. 1, pp. 340-342, June 1974.

[16]   S. O. Piper, *Frequency-modulated continuous wave systems*, Norwood, MA, Artech House, 1993.

[17] A. E. Carr, L. G. Cuthbert and A. D. Oliver, "Digital signal processing for target detection in FMCW radar," *IEE Proc. Communications, Radar, and Signal Processing,* vol. 128, no. 5, pp. 331-336, Oct. 1981.

[18] D. R. Wehner, *High resolution radar*, Norwood, MA, Artech House, 1995.

[19] K. Iizuka and A. P. Freundorfer, "Detection of nonmetallic buried objects by a step frequency radar," *IEEE Proc.,* vol. 71, no. 2, pp. 276-279, Feb. 1983.

[20] D. A. Noon, "Stepped-frequency radar design and signal processing enhances ground penetrating radar performance," Ph.D. Thesis, University of Queensland, Queensland, Australia, 1996.

[21] L. A. Robinson, W. B. Weir and L. Young, "An RF time-domain reflectometer not in real time," *in GMTT International Microwave Symposium Digest*, vol. 72, no. 1, pp. 30-32, May 1972.

[22] R. C. Pippert, K. Soroushian and R. G. Plumb, "Development of a ground-penetrating radar to detect excess moisture in pavement subgrade," *in Proc. of the Second Government Workshop on GPR – Advanced Ground Penetrating Radar: Technologies and Applications,* pp. 283-297, Oct. 1993.

[23] A. Langman, P. D. Simon, M. Cherniakov and I. D. Langstaff, "Development of a low cost SFCW ground penetrating radar," *in IEEE Geoscience and Remote Sensing Symposium,* vol. 4, pp. 2020-2022, May 1996.

[24] G. F. Stickley, D. A. Noon, M. Cherniakov and I. D. Longstaff, "Preliminary field results of an ultra-wideband (10-620 MHz) stepped-frequency ground penetrating

radar," *in Proc. of the 1997 IEEE Int. Geoscience and Remote Sensing Symp.*, vol. 3, pp. 1282-1284, Aug. 1997.

[25]   D. Huston, J. O. Hu, K. Muser, W. Weedon and C. Adam, "GIMA ground penetrating radar system for monitoring concrete bridge decks," *Journal of Applied Geophysics,* vol. 43, pp. 139-146, May 2000.

[26]   F. T. Ulaby, R. Moore and A. Fung, *Microwave remote sensing*, vol. 3, Norwood, MA, Artech House, 1986.

[27]   R. E. Collin, *Foundations for microwave engineering*, 2nd Ed., New York, NY, McGraw-Hill, 1992.

[28]   D. M. Pozar, *Microwave engineering*, 2nd ed., New York, NY, John Wiley & Sons, 1998.

[29]   R. H. Church, W. E. Webb and J. B. Salsman, "Dielectric properties of low-loss materials," Report of Investigations 9194, US Bureau of Mines, Washington D.C., 1998.

[30]   J. L. Davis A. P. Annan, "Ground-penetrating radar for high-resolution mapping of soil and rock stratigraphy," *Goephysical Prospecting*, vol. 37, No. 5, pp. 531-551, Jul. 1989.

[31]   D. J. Daniels, *Surface-penetrating radar*, London, UK, The Institute of Electrical Engineers, 1996.

[32]   D. E. Kerr, *Propagation of short radio waves*, New York, NY, McGraw-Hill, 1964.

[33]   R. J. Yelf and G. Turner, "Applications of ground radar to coal mining," *in Proc. of the 3rd International Conference on GPR*, pp. 87-89, May 1990.

[34]   M. I. Skolnik, *Introduction to RADAR systems*, 3rd ed., New York, NY, McGraw-Hill, 2001.

[35]   B. Edde, *RADAR principles, technology, applications*, Englewood Cliffs, NJ, Prentice Hall, 1995.

[36]   C. A. Balanis, *Antenna theory analysis and design*, 2nd ed., New York, NY, John Wiley & Sons, 1997.

[37]   B. Razavi, *RF microelectronics*, Englewood Cliffs, NJ, Prentice Hall, 1998.

[38]   J. G. Proakis, and D. G. Manolakis, *Digital signal processing*, Englewood Cliffs, NJ, Prentice Hall, 1996

[39]   K. Chang, *Microwave solid-state circuits and applications*, New York, NY, John Wiley & Sons, 1994.

[40]   E. A. Theodorou, M. R. Gorman, P. R. Rigg and F. N. Kong, "Broadband pulse-optimized antenna, " *IEE Proc*., vol. 128, Pt. H, no. 3, pp. 124-130, June 1981.

[41]   S. Evans and F.N. Kong, "TEM horn antenna: Input reflection characteristics in transmission," *IEE Proc*., vol. 130, Pt. H, no. 6, pp. 403-409, Oct. 1983.

[42]   J. D. Cermignani, R. G. Madonna, P. J. Scheno and J. Anderson, "Measurement of the performance of a cavity backed exponentially flared TEM horn," *Proc. of SPIE, Ultrawideband Radar,* vol. 1631, pp. 146-154, Jan., 1992.

[43]   C. Nguyen, "A wideband antenna," Patent Pending, Technology Licencing Office, Texas A&M University, College Station, TX, 1999

[44]   C. Nguyen, J. Lee and J Park, "Novel ultra-wideband microstrip quasi-horn antenna," *Electronics Letters*, vol. 37, no. 12, pp. 731-732, June 2001.

[45]   F. E. Churchill, G.W. Ogar and B.J. Thompson, "The correction of I and Q errors in a coherent processor," *IEEE Trans. on Aerospace and Electronic Systems,* vol. 17, no. 1, pp. 131-137, Jan. 1981.

VITA

Joongsuk Park received his Bachelor Science degree in electrical engineering in 1988 from Yonsei University, Seoul, Korea. Upon graduating, he worked as a research and applications engineer at LG Electronics Inc., for 9 years. During that time, he developed subsystems and systems for analog and digital TVs.

He received his Ph.D. degree in electrical engineering at Texas A&M University in December 2003. He worked as a research assistant under the guidance of Dr. Cam Nguyen.

His research interests are in microwave and millimeter-wave integrated circuits and antennas, surface and subsurface radar sensors, nondestructive testing and evaluations, and ultra-wideband systems for communication and sensor applications.

His permanent address is 26-1207 Hanyang Apt., Apgujung-Dong, Kangnam-Ku, Seoul, 135-110, Korea.